The effect of exchange and magnetostatic interactions on grain boundaries

Louise Lillias Margaret Barron

Thesis submitted for the Degree of

Doctor of Philosophy

University of Edinburgh

2011

Dedication

This work is dedicated to my great-grandmother Lillias Steven Laird who graduated in science nearly 100 years ago and very kindly let me have her name.

Declaration

This thesis is entirely the work of myself, all the following work is my own unless otherwise referenced. None of this body of work has been submitted, either whole or in part, for any other degree award.

Louise Barron 16^{th} May 2011

Abstract

Magnetic minerals are abundant within our Earth's crust and can retain, through one of a number of processes, a remanent magnetisation induced by the Earth's magnetic field. Analyses of palaeomagnetic samples have been used for the past fifty years to improve our understanding of many of the Earth's major processes.

Recent studies utilising newly developed imaging techniques, namely holographic transmission electron microscopy, have for the first time allowed direct observations of the magnetic structure in palaeomagnetic samples on a nanoscale. It is commonly observed that igneous rocks contain closely packed magnetic lamellae with a non-magnetic matrix, a result of the chemical process of exsolution. However, the results of current micromagnetic models, generated to predict the magnetic structure within such samples, are not in agreement with these direct observations. The results do, however, show strong similarities to the direct observations. The discrepancies between the direct observations and micromagnetic models indicate a lack of understanding of the magnetic interactions within such samples. To examine this two distinct hypotheses have been tested.

Firstly, the geometry of the system has been altered to examine the effect of this on the magnetic structure of the grains. Secondly, a multiphase model has been produced. This multiphase model allows the simulation of more complicated systems that include more than one magnetic material in direct contact. This multiphase model has allowed us to examine the effect of varying the exchange in these multiphase structures and its effect on the modelled magnetic structure. Further, this multiphase model has allowed us to examine theoretical systems involving combinations of magnetic materials commonly found in palaeomagnetic samples.

Acknowledgements

This research would not have been possible without the continued support of many people.

In particular I thank my supervisor Prof Wyn Williams who has continued to give me all the support and patience necessary to complete this thesis. I have greatly benefitted also from discussions with Dr Adrian Muxworthy, Dr Richard Harrison, Dr Rafal Dunin-Borkowski, Nathan Church and Dr Takeshi Kasama. Similarly I thank Ruth Carley, Ciaran Beggan, Caroline Graham and Jennifer Rapp who have advised me on specific aspects of this research.

I have received a great deal of support from the GeoSciences IT staff, especially from Shane, Faye, Magnus and Justin. Thanks are due also to the administration staff who have helped me on many occasions.

I also wish to thank my parents, my sister Kate, and also Rhian whose proof reading has been invaluable.

This entire PhD experience would not have been nearly as enjoyable without the happy home life with my "Edinburgh family" of Caroline, Jenny and Matt. In a similar vein, this experience has been helped by the friendship and support of all the "attic dwellers" past and present.

Finally, I would like to thank my family who have only ever supported and encouraged me and continue to do so.

This project has only been made possible by NERC award NE/D0020366/1. All the 3D images have been produced using Tecplot 360 and all the geometry and mesh generation has been carried out using the CUBIT Sandia CAD package. Translation for the genesis file format has been done using netcdf. The thesis has been produced using LaTeX.

Abbreviations

1D	.....	One dimensional
2D	.....	Two dimensional
3D	.....	Three dimensional
TRM	.....	Thermal remanent magnetisation
NRM	.....	Natural remanent magnetisation
DRM	.....	Detrital remanent magnetisation
VRM	.....	Viscous remanent magnetisation
IRM	.....	Isothermal remanent magnetisation
SD	.....	Single domain
PSD	.....	pseudo-single domain
MD	.....	Multi-domain
CAD	.....	Computer aided design
LLG	.....	Landau Lifshitz Gilbert equation

Symbols

e	.....	electronic charge
I	.....	current
L	.....	Angular momentum
n	.....	Principal quantum number
A_{ex}	.....	Exchange constant
$K1$	.....	1^{st}order magnetocrystalline anisotropy constant
$K2$	.....	2^{nd} order magnetocrystalline anisotropy constant
Ms	.....	Magnetic saturation
T_C	.....	Curie temperature
T_v	.....	Verwey temperature
T_M	.....	Morin temperature
T_N	.....	Neél temperature
γ	.....	Gyromagnetic ratio
α	.....	Gilbert damping constant
M	.....	Magnetisation
E	.....	Energy
E_{K1}	.....	Anisotropy energy
E_{ext}	.....	External energy
$E_{A_{ex}}$	.....	Exchange energy
E_{demag}	.....	Demagnetisation energy
H	.....	Magnetic field
J	.....	Exchange integral
χ	.....	Magnetic susceptibility
Φ	.....	Magnetic potential

Physical Constants

e	electron charge	$1.60 \times 10^{-19} Coulombs$
m	electron mass	$9.11 \times 10^{-31} kg$
μ_B	Bohr Magneton	$9.274 \times 10^{-24} JT^{-1}$
μ_0	permeability of free space	$4\pi \times 10^{-7} Hm^{-1}$
$\hbar$	Plancks Constant	$1.05457148 \times 10^{-34} m^2 kg/s$

Contents

List of Figures

List of Tables

Chapter 1

Introduction

Palaeomagnetism has been at the forefront of many of the geological breakthroughs of the last 50 years, such as plate tectonics and polar drift, and as such palaeomagnetic samples create the basis for many geological studies. It is, therefore, vital that we have a firm understanding of the physics of such samples, particularly the physics of how such samples are created and the effect of the sampling procedures on the samples. Our understanding of magnetism within the field of physics and our understanding of our Earth's magnetic field, one of the first properties attributed to the Earth, developed independently until the 1960s when the work of Nagata combined the two.

To better our understanding of these magnetic systems used so commonly within palaeomagnetic studies we use computer simulations. These simulations are built using the mathematical theory available about magnetic structures on appropriate scales, the aim of these models being to try to simulate the magnetic structures directly observed within samples. The first such micromagnetic simulations were carried out in 1935 by Landau and Lifshitz [Landau and Lifshitz (1935)], but these first simulations considered only certain energy contributions affecting magnetic systems, namely the anisotropy information. Although these early models were by no means a full description of the magnetic systems they were, nonetheless, an important foundation for subsequent micromagnetic sim-

ulations. Micromagnetic models are more advanced using a fuller mathematical description of the physics of the systems. Similarly this field has benefited greatly from the advances in computing speed and efficiency over the last ten years allowing the simulations of larger and more complicated systems at greater resolutions.

A further important tool which has aided this field has been the development of more powerful imaging techniques which enable the comparison of computer simulations with direct observations on a nanoscale, providing the opportunity to test more fully the fidelity of the simulations. Observations at a nanoscale are of particular importance due to the significance of nanoscale single domain (SD) systems within palaeomagnetic samples.

This study is part of a larger collaboration involving Cambridge University and Danmarks Tekniske Universitet (The Technical University of Denmark, DTU). This project has included the experimental generation and the subsequent imaging of samples analogous to those observed in natural samples and used within palaeomagnetic studies. This specific body of work was undertaken to use these experimentally produced samples to produce micromagnetic models with the aim of examining the fidelity of the current micromagnetic model as applied to irregular and multiphase structures.

The catalyst for the micromagnetic modelling section of this study was a previously modelled irregular structure shown in Figure 1.1. This was the first time this micromagnetic model had been used to examine an irregular structure and a structure pertaining to a real sample. Importantly this sample, through off-axis electron holography, also had a known in-plane magnetic field that allowed a direct comparison of both the model and the directly observed magnetic structure of the sample.

The degree of similarity between model and direct observation is striking, however there are certain differences between the two. Of particular interest is the positioning of the vortex structures, the features indicated within Figure 1.1 within the sample. The structures are consistently located within the body of the lamellae in the direct observations and at the boundaries between the lamellae

in the models. This is an interesting result as magnetic theory would suggest that nucleation of a vortex is more inclined to start at an edge or a corner within a magnetic system. However, the micromagnetic model does not take into account that the magnetite regions are separated by another material. Ulvöspinel, although non-magnetic, still contains magnetic exchange carriers. The overall aim of this research was therefore to examine if increasing/changing the interaction between the individual lamellae would have an effect on the overall observed magnetic structure of a system.

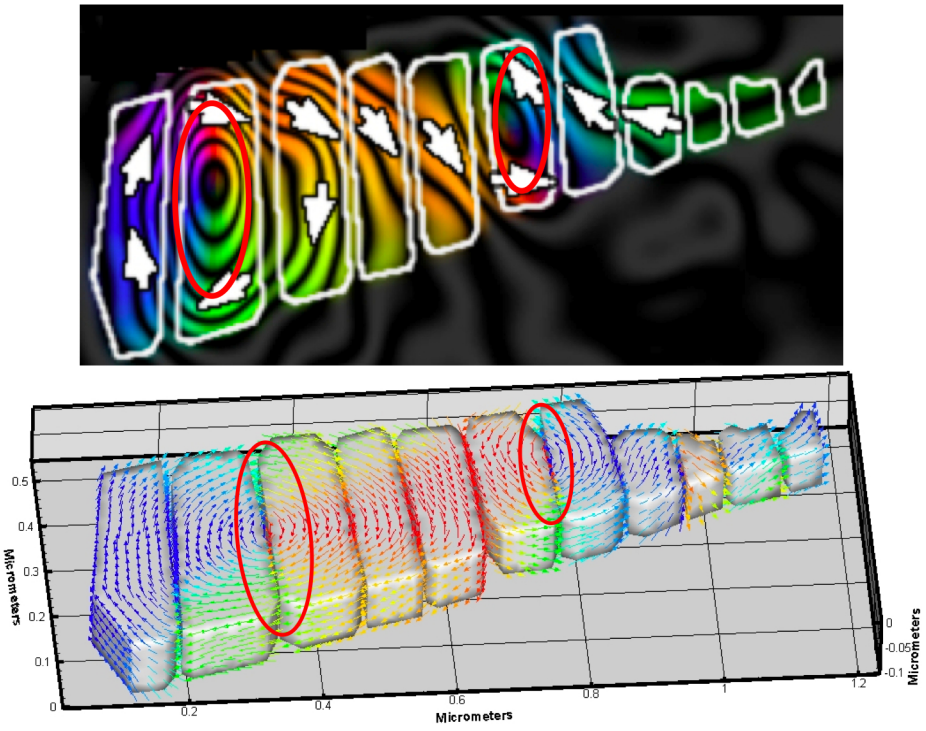

Figure 1.1: The top image [Feinberg et al. (2005) and Feinberg et al. (2006)] shows the direct observations of the in-plane magnetic field of magnetite lamellae (outlined in white) within a ulvöspinel host matrix. The bottom image shows the model simulation of the same system. Indicated in both direct observation and model are the vortex structures. The model result is a vector plot where each vector denotes the direction of the magnetisation at that point. The colour in both direct observation and model result indicate the direction of the magnetisation in the system. A fuller description of how to interpret both direct observations and model results can be found in sections 3.3.3 and 3.5.1 respectively.

1.1 Project Rationale

This body of work falls into two main areas. The first of these areas is examining the effect of the geometry of the system on the overall magnetic structure and its effect if any on the vortex positioning. In particular physical bridging within the system has been examined, discussed in Chapter 5, a mechanism by which a thin magnetite bridge exists between neighbouring magnetite lamellae. To test this the physical geometry created in a computer aided design package (CAD) was altered to allow simulations of various possible geometries and examine the effects on the magnetic structures observed.

The second area of work is the possibility of an indirect form of exchange interacting between the magnetite lamellae. To test for this required significant alteration of the existing micromagnetic code. The existing code is capable only of simulations of single phase, that is a system of only one material. Much of this study has been devoted to producing a micromagnetic simulation capable of modelling variations in the magnetic parameters within the sample. This model will be referred to as the 'multiphase model'.

Finally some case studies have also been examined. These case studies involve the application of the single phase model to examine specific biogenic irregular structures allowing the examination of their magnetic structures. Also included is an examination, using the multiphase magnetic model, of multiphase systems of common magnetic materials used within the field of palaeomagnetism. In addition to these multiphase systems other models examining the process of oxidation as observed within the magnetite-maghemite system are included.

1.2 Thesis Plan

Presented in Chapter 2 is a section containing some relevant background theory. The theory discussed includes a general introduction to magnetism followed by a more detailed examination of the theory governing micromagnetic systems.

This chapter also contains background information discussing the importance of micromagnetics within the field of palaeomagnetism and, furthermore, a geological background to palaeomagnetism. Finally a description is given of some of those chemical processes affecting palaeomagnetic studies and also the chemical systems of most prevalence within palaeomagnetic studies.

In Chapter 3 there is a short discussion of the current state of the art of micromagnetic modelling and its history presented with a detailed description of all the numerical micromagnetic computer code utilised within this study. This discussion of the micromagnetic modelling also introduces the geometry generation used within this study and how the fidelity of these micromagnetic codes can be tested. In addition to this is a discussion of the new multiphase model used for this study, including a discussion of the more complex geometry generation required to run this multiphase model.

Chapters 4, 5 and 6 contain a selection of results. Firstly in Chapter 4, using the single phase code, is a set of results from irregular geometries with both experimental and biological origins. Chapter 5 contains the results from the physical bridging section of the project. In Chapter 6, utilising the multiphase coding is a selection of results showing simulations of simple multiphase materials and also of more complex systems. In addition this section presents a short example of the oxidation process concerning magnetite and maghemite.

Finally, brief discussions and conclusions are included in Chapter 7. This chapter examines some of the more important findings from this study. Also addressed within this chapter is some discussion of possible future work pertaining to this research and some improvements which could have been made with increased time and resources.

Chapter 2

Theory

2.1 Magnetic quantisation

All matter, from simple atomic particles to macroscopic materials, exhibits magnetic properties. These magnetic properties are a result of all individual atoms having a magnetic moment associated with them, where this magnetic moment is a consequence of both the angular momentum of the electron orbiting the nucleus of the atom and of the spin angular momentum corresponding to each individual electron [Myers (2002)].

The magnetic contribution from the orbital component is a consequence of an effective current loop created by an electron orbiting an atomic nucleus. The motion of a charge e making a circular orbit of radius r will induce a current I, where v is the speed of the charge.

$$I = \frac{ev}{2\pi r} \tag{2.1}$$

Using Ampère's law we can express the magnetic moment associated with this current loop, μ_L.

$$\mu_L = IA = \frac{ev}{2\pi r}\pi r^2 = \frac{evr}{2} \tag{2.2}$$

However, through our understanding of Bohr's model of the atom, it is recognised that an electron can exist only in a predefined orbit radius, and as such an atom can exist only in certain energy states. It follows that the angular momentum L of an electron of mass m_e can only take certain quantised values. The value of the angular momentum is related to the quantum number of the system n, where n can take the value of a positive integer only.

$$L = n\hbar = m_e v r \tag{2.3}$$

The magnetic moment associated with the angular momentum of the electron μ_L can therefore be expressed as seen in equation 2.4.

$$\mu_L = \frac{ne\hbar}{2m_e} \tag{2.4}$$

In a classical setting the spin on an electron can be perceived to be the rotation of the electron around its centre of mass. Like the angular momentum of the system the spin value is similarly quantised and can take the value $\frac{\hbar}{2}$ or $\frac{-\hbar}{2}$. The value for the spin angular momentum s can therefore be expressed as follows where s is the spin quantum number and takes the value $\frac{n}{2}$.

$$S = \sqrt{s(s+1))}\hbar \tag{2.5}$$

Frequently the magnetic moment will be measured in terms of Bohr magnetons. The Bohr magneton is equivalent to the magnetic moment of one electron existing in the atomic ground state, therefore n will take a value of 1, where the variables e and m are respectively the charge and mass of the electron and $\hbar$ is Planck's constant. The value of the Bohr magneton is therefore $9.274 \times 10^{-24} JT^{-1}$.

$$\mu_B = \frac{-e\hbar}{2m} \tag{2.6}$$

To quantify the net magnetic strength, or the magnetic moment, of a system

we have to sum all the contributory magnetic sources within the system.

2.2 Domain theory

Although the previous section examines the atomic scale phenomena responsible for magnetism it is more useful to examine magnetic systems at a more microscopic scale which relates better to the scale of the subject matter that is examined in this thesis.

Magnetic materials can broadly be classified as either permanent or non-permanent magnetisation (paramagnetic). Those materials falling into the latter category will exhibit magnetisation only in the presence of an external magnetic field, this magnetisation being lost when this field is removed. In the case of the permanent magnet the induced magnetisation will remain even when the external field is absent. This phenomenon was first explained by Weiss (1907), where he postulated the existence of a strong molecular field which will cause neighbouring atomic moments to align resulting in a spontaneous magnetisation. There are various physical properties of a material which are responsible for the domain energy of a system. The main energies involved, and those which will be discussed in this section, are magnetocrystalline anisotropy, exchange energy and magnetostriction [Neel (1949)].

2.2.1 Magnetocrystalline anisotropy

The magnetic anisotropy of a system is the result of the material having a specific magnetic direction which is favoured, or, in the case of an isotropic anisotropy no favoured magnetic direction. There are a number of anisotropy contributions such as shape anisotropy and stress anisotropy. The contribution discussed in this section is, however, the magnetocrystalline anisotropy. The result of the magnetocrystalline anisotropy energy is such that the magnetisation will orientate along one or more crystallographic axes within the system. These preferential

magnetic directions are determined by the crystallographic structure and are referred to as the easy axes of magnetisation, as it is energetically favourable for the magnetisation to align along such axes. It is the excess energy required to move the magnetisation from the easy to the hard axis which is referred to as the anisotropy energy. The magnetocrystalline anisotropy energy of certain crystallographic systems can be affected by the system temperature. Highly symmetrical crystal systems are likely to have a far lower anisotropy energy than those with low symmetry systems [Kittel (1949b)].

On an atomic level the mechanism for the anisotropy cannot be the exchange energy, the exchange energy being directly related to the orientation of neighbouring spins within the system. However, it is also irrespective of the crystallographic axis of the system. Instead it is thought that the anisotropy arises from the spin-orbit interaction and the partial quenching of the orbit angular momentum.

2.2.2 Exchange energy

The exchange energy is a consequence of the interaction occurring between neighbouring spins within a system and can be represented as follows. Neighbouring spins can be either parallel or anti-parallel to each other depending on the value of the exchange integral, J, of the spin. These parallel and anti-parallel alignments can also have a degree of canting. When examining a single atom with z nearest neighbours, all orientated in the same orientation, the exchange energy can be expressed as seen in equation 2.7, where μ_B is the Bohr magneton, H_{mf} the Weiss molecular field and S the spin quantum number discussed previously in section 2.1. [Kittel (1949a)].

$$2zJS^2 = 2S\mu_B H_{mf} \tag{2.7}$$

2.2.3 Magnetostriction

Magnetostriction is another important effect within the magnetisation process. Magnetostriction results in the crystal system of a magnetic material deforming as an effect of the magnetisation process. This deformation is caused by added strain within the crystal system as a result of the magnetic interaction within the atoms forming the crystal structure. This strain affects all three principle axes within a crystal habitat altering the overall crystal structure and consequently the magnetosrystalline anisotropy will also be affected. Magnetostriction occurs to minimise the effect from this action. As such magnetostriction will also affect the magnetocrystalline anisotropy of the system and also the exchange energy [Neel (1955)].

2.2.4 Magnetic Domains

Magnetic domains are areas of uniform magnetisation within the microstructure of a magnetic material. As such it is this magnetic theory that is the basis for examining the micromagnetics of a system. The study of domains allows the determination, through examining the microstructure, of the macroscopic properties associated with a material. Due to an increased reliance on granular magnetic materials with dimensions within the nano and microscale within new technologies, such as those used within magnetic storage, there has been a greater drive to understand fully and exploit the phenomena associated with domain theory. A more detailed discussion of this section can be found in Huberts "Magnetic Domains" [Hubert and Schafer (1998)] and Dunlop and Ozdemirs "Rock magnetism fundamentals and frontiers" [Dunlop and Ozdemir (1997)].

The idea that a magnetic material contains discrete elementary magnets has been accepted from the beginning of the 19^{th} century, but experimental evidence of these structures was only determined in 1919 with the research of Heinrich Barkhausen [Barkhausen (1919)]. Barkhausen's research involved using an amplifier to give an audible signal whilst magnetising a material and it was found

that the audio signal obtained was discontinuous. In an extension of this research it was found that certain systems, under the same regime as Barkhausen's original experiments, produced only one discrete signal during the magnetisation process such that the system could be assumed to be jumping instantaneously from one magnetisation state to the other. This would indicate the existence of only one domain and, thus, is quite unlike Barkhausen's original work. Consequently, to explain these phenomena it was hypothesised that there must be propagation of some wall separating adjacent regions of opposite magnetisation, thus the idea of domain walls was introduced. Domains were only physically observed in 1935 with the work of Bitter and his research utilising fine magnetic powders of magnetite grains within a colloidal suspension which were attracted to the stray fields produced from boundaries between domains. The Bitter pattern method remains a useful tool today for examining domain structures [Szmaja and Balcerski (2002)].

These magnetic domains will often, without the application of an external field, be aligned such that no net overall magnetisation is observed. However, when an external field is applied, those domains favourably orientated with the applied field will grow at the expense of those domains which are not. This is a reversible process if an inverse external field is then applied to the system. However, the application of an external field can also result in the elimination of unfavourably orientated domains, with the area being occupied entirely by those favourably orientated domains, and unlike the previous example this process is not reversible [Hubert and Schafer (1998)]. The result of this irreversible process is the root of hysteresis within magnetic materials. When a material is subjected to an increasing magnetic field it will, when exceeding a certain field value, have all domains in the system aligned, therefore existing as a single domain system. However, as the external field is reduced to zero the magnetisation of the system will not return to zero, instead exhibiting a remanent magnetisation. This remanent magnetisation can only be removed by heating the material through its Curie temperature T_C, or in the case of non-ferromagentic materials the Néel

temperature T_N.

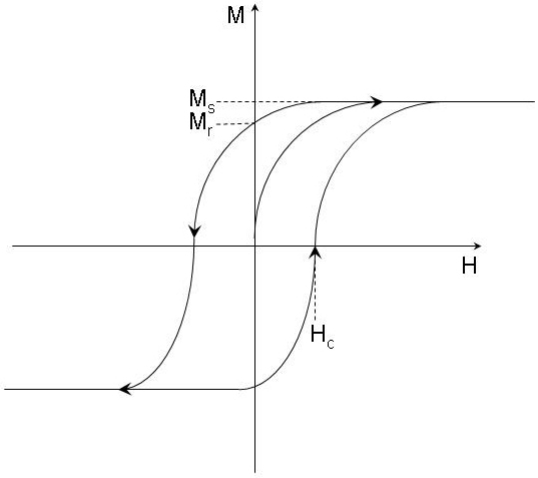

Figure 2.1: An example of hysteresis showing the residual magnetisation M_r, coercive field H_c and saturation magnetisation M_s

Figure 2.1 shows a hysteresis process within a magnetic material, where M and H are the magnetisation and magnetic field respectively, M_r is the residual magnetisation and H_c the coercive field of the system with M_s the saturation magnetisation. The spontaneous magnetisation of a magnetic domain is, on an atomic scale, an effect of the Heisenberg exchange interaction existing between neighbouring atoms within a crystallographic structure. It is similarly the Heisenberg exchange interaction responsible for the structure of the domain walls in a magnetic system. Domain wall width varies depending on the material they are present in, although they are generally in the range of hundreds of atoms wide. The structure of the domain wall is an effect of the alignment of the spins and will often undergo an angular displacement of 90° or 180°. An example of a 180° displacement, or 180° Bloch wall, can be seen in Figure 2.2.

The overall domain energy of the system is a summation of all the contributing energies, in this case the magnetocrystalline anisotropy, exchange energy, magnetolastic energy and magnetostatic energy.

All magnetic materials will contain one or more magnetic domains. A single

domain (SD) system will contain only one magnetic domain, and is therefore a system unable to support domain walls. The critical grain size for a material to display a SD structure will vary depending on its magnetic properties. In the case of magnetite a SD structure will be observed in grain sizes $\leq 0.08\mu m$ [Enkin and Dunlop (1987),Enkin and Williams (1994)], for haematite we would expect to observe SD structure in grains with dimensions $\leq 15\mu m$ [Banerjee (1971), Chevallier and Mathieu (1943)]. All other systems will contain multiple domains (MD). In the case of a pseudo-single domain system (PSD) the systems will behave as a single domain system embedded within a MD matrix.

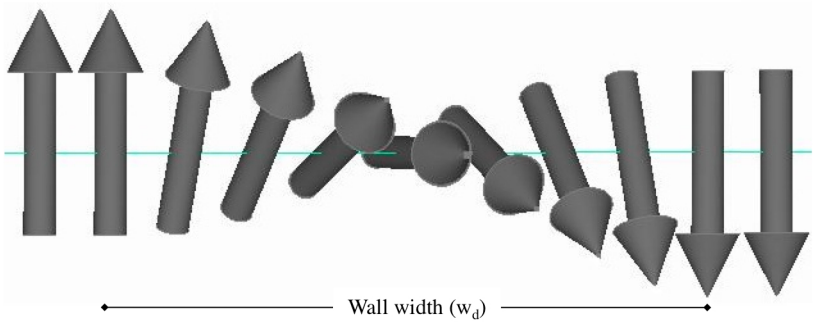

Figure 2.2: Dynamics of a 180^0 domain Bloch wall showing the rotation of the individual spins over the wall width W_d

2.3 Classification of Magnetic Systems

All magnetic materials are commonly classified depending on their magnetic properties. The following explains the main classifications which will be mentioned within this body of work.

2.3.1 Diamagnetism

All materials have a so-called diamagnetism associated with them. However, the strength of this type of magnetisation is dependent on the individual interaction

between the neighbouring atoms. Diamagnetism is only exhibited when an external magnetic field is applied to a system and the diamagnetism is the response of the individual magnetic moments within the system. Different substances can exhibit a variety of different magnetic properties and different structures.

2.3.2 Ferromagnetism

The simplest magnetic structure is ferromagnetism (Figure 2.3), first identified by Weiss, of which iron is the most common natural example. Within the ferromagnet all the individual atoms are identical and therefore exhibit an identical permanent magnetic moment, these individual moments aligning parallel to each other. This parallel alignment is a direct consequence of the exchange interaction between neighbouring spins.

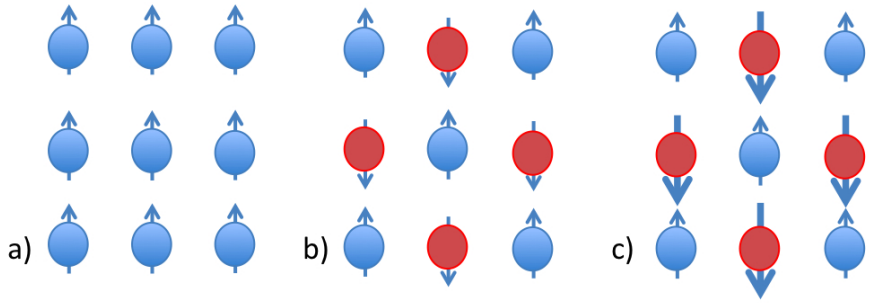

Figure 2.3: Figure showing sketches of a) ferromagnetism, b) antiferromagnetism and c) ferrimagnetism where the individual circles are the individual moments of the system, the arrows denoting the direction and the magnitude of the magnetic moments. As can be seen in a) the magnitudes and directions are all identical whereas in the b) and c) this is not the case.

2.3.3 Ferrimagnetism

Ferromagnetism (Figure 2.3) is an example of a structure where all the atoms are identical. However, most minerals will contain more than one type of atom and as a consequence will exhibit more complex magnetic structures. Ferrimagnetic

structures contain more than one type of atom and this structure is often exhibited by the ferrite spinel class of minerals to which magnetite, the most magnetic naturally occurring mineral, belongs. A material with a ferrimagnetic structure contains more than one type of atom and, within some temperature ranges, these different atoms will exhibit unequal magnetic moments and will align anti-parallel to each other [Young and Freedman (1996)]. A ferrimagnetic material will still exhibit a permanent magnetisation however, but this magnetisation will be less than that of a ferromagnetic material with an identical atom density.

2.3.4 Antiferromagnetism

A further common magnetic structure is antiferromagnetism (Figure 2.3). This magnetic structure contains atoms with identical magnetic moments orientated anti-parallel to one another and the consequence for this is that an antiferromagnetic structure will not exhibit an overall permanent magnetic moment as the individual magnetic moments will cancel each other out [Young and Freedman (1996)]. An extension to antiferromagnetism is canted-antiferromagnetism, the unique feature of this structure being that the individual magnetic moments are anti-parallel and rotated. A common example of this structure is haematite. Ferromagnetism, ferrimagnetism and antiferromagentism are all examples of ordered magnetic states [Young and Freedman (1996)].

2.4 Mineral Magnetisation

Palaeomagnetism is the study of the past magnetic direction and magnitude of the Earth's magnetic field. Magnetism has been instrumental in our understanding of geology for over 400 years. The Earth's magnetic properties were, after the Earth's spherical nature, the first attributes to be applied to our planet by De Magnete (Gilbert, 1640). Our understanding of the Earth's magnetic field has, over these hundreds of years, evolved significantly from this original belief that the

magnetic field was the product of a uniformly magnetised sphere to the currently accepted theory of magnetohydrodynamics within the fluid outer core of the Earth [Hamblin and Christiansen (1995)].

2.5 Remanent Magnetisation

The most abundant magnetic element within the Earth's crust is iron (Fe). Iron is also one of the most magnetic elements and, as such, many Fe bearing minerals are also extremely magnetic. Of these minerals, magnetite exhibits the greatest natural magnetic signal and is therefore pivotal within palaeomagnetic studies. It is the interaction of these magnetic minerals with the Earth's magnetic field which is the basis for palaeomagnetic recording and interpretations. Magnetic minerals, through a number of different physical methods, will retain a memory of the magnetic field, also referred to as a natural remanent magnetisation (NRM), at their time of creation.

2.5.1 Thermal and Metamorphic Remanent Magnetisation

Thermal remanent magnetism [Evans and Heller (2003)], TRM, is found within iron bearing igneous rocks and is the most reliable method by which a rock acquires a remanent magnetisation. Lavas containing iron are expelled at temperatures exceeding the Curie temperature and the material will therefore exhibit a paramagnetic magnetic system. In this paramagnetic state the magnetic moments are free to align themselves with the Earth's magnetic field. As the material cools below the Curie temperature this magnetic signal will be preserved within the rock, giving it a remanent magnetisation related to the magnetic field at its time of origin. Similarly this process will also happen under metamorphosis, those minerals carrying a remanent magnetisation being demagnetised by the increase in temperature and once more becoming free to align with the current magnetic

field. Over time processes such as crystallisation and other chemical processes within these magnetic minerals may result in a secondary magnetic remanence component and therefore the possible modification of primary remanence component within materials.

2.6 Exsolution

Of those processes which can give rise to a secondary remanent magnetisation component, the one of most concern within this study is the process of exsolution. The most common, and arguably the most important, occurrence of exsolution within geology is the production of perthite from exsolved alkali feldspar. Perthite is a term used to describe alkali feldspar with a characteristic exsolution texture. The form of this exsolution texture can give valuable information regarding the conditions of formation. When examining a phase profile, exsolution is easily identifiable by the hoop shaped solvus within the system.

The process of exsolution also affects the titanomagnetites, the most important solid solution with respect to palaeomagnetic interpretations [Price (1980)]. Exsolution from a solid solution is a consequence of the processes of both spinodal decomposition and nucleation and growth [Smith (1980)]. Spinodal decomposition and nucleation and growth both result in the separation of a homogenous system into one containing heterogeneities. Spinodal decomposition is described by the Cahn-Hilliard equation (equation 2.8).

$$\frac{\partial c}{\partial t} = D\Delta^2\mu \tag{2.8}$$

The Cahn-Hilliard equation expresses how the concentration c changes with time where D is the coefficient of diffusivity and μ is the chemical potential of the system [John (1965)]. Spinodal decomposition is caused by a perturbation within the concentration of a particular region of the system [John (1965)]. We would expect diffusion to correct the perturbation within this system, returning

it to its original homogeneous state. However, counter intuitively, a backwards diffusion process takes place causing increased segregation of the system into two distinct phases.

Nucleation and growth will also result in two distinct phases within an originally homogeneous material, but the mechanism by which this happens is different from that of spinodal decomposition. In the case of nucleation and growth the concentration of the homogeneous system is perturbed to an extent that an area of significantly higher concentration is created. The surrounding region of this high concentration nucleus will have a lower concentration, as it has been depleted by the perturbation.

The exsolution process results in the production of extremely small-scale structures, typically <0.5 μm, being formed within the titanomagnetites. The scale of the structures observed is a result of the speed at which this chemical process occurs. The fine structures exhibited are of clusters of closely packed lamellae interspersed within the host matrix. In this study we observe instances of magnetite lamellae within an ulvöspinel host matrix and magnetite lamellae within a haematite host matrix. Importantly the distinct regions are found to have very distinct boundaries separating the different phases.

2.7 Magnetite and Haematite Solid Solutions

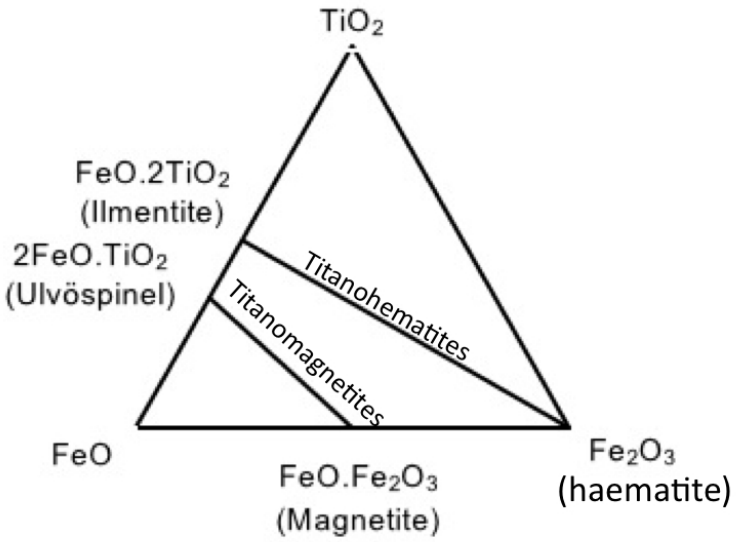

Figure 2.4: Phase diagram representing the systems of interest where the tie lines represent the solid solution series

The magnetite and haematite solid solutions (Figure 2.4) are the most significant solid solution systems within the field of palaeomagnetism. Magnetite is particularly important as it is a strongly magnetic naturally occurring mineral, and is highly abundant within crustal rocks. As a consequence of magnetite's importance within palaeomagnetic studies, much work, both experimental and theoretical, has been undertaken to understand and quantify magnetite's crystallographic structure and magnetic properties.

Magnetite ($FeOFe_2O_3$) belongs to the inverse spinel mineral class which has the general chemical formula XY_2O_4, where X and Y are transition metals. A solid solution involving Fe and Ti in this system is referred to as the titanomagnetite series [Deer et al. (1966)]. Magnetite has a T_C of 851 K. Ulvöspinel also exhibits an inverse spinel structure. Consequently, magnetite and ulvöspinel may exist as a solid solution at high temperatures but exsolve at lower temperatures. This structure contains both tetrahedral and octahedral bonding sites, with, in

the case of magnetite Fe, ions in place at both these sites surrounded by four or six oxygens respectively [Harrison and Putnis (1998)]. It is these different bonding sites which give rise to two distinctive sub-lattices within the structure and therefore a ferrimagnetic structure. Magnetite allows a great deal of Ti to enter the structure, resulting in a continuous relationship between both magnetite and ulvöspinel. Ulvöspinel, with a similar structure to magnetite, will also have two distinct lattices, although through the inclusion of titanium in this system it will exhibit an overall antiferromagnetic structure.

Another important consideration when examining magnetite is the effect of the Verwey transition. The Verwey transition marks a change in the crystalline phase of magnetite, where the magnetocrystalline anisotropy structure will alter from a cubic system to a uniaxial system. This transition is related to magnetite's temperature where below a value of $T_v = 122$K [Doriguetto et al. (2003)] a discontinuous reduction in the conductance of a sample will be seen.

In addition to magnetite, haematite is also important in palaeomagnetic studies as it is the most stable iron oxide under ambient conditions and is abundant within the Earth's crust. Due to haematite's importance, there has been extensive research carried out to characterise its intrinsic magnetic properties. However, despite this research, the magnetic properties still remain poorly quantified. In a similar fashion to magnetite and ulvöspinel, haematite and ilmentite exist as a solid solution at high temperatures, but exsolve into two distinct phases at lower temperatures. Haematite exhibits a trigonal structure and takes the form of layers of oxygen, in a close packed hexagonal structure, and layers of iron. These layers are perpendicular to the triad or c-axis of the system and, as a result, haematite displays a canted-antiferromagnetic structure. Ilmentite similarly exhibits a trigonal structure and also has an antiferromagnetic structure.

Haematite is affected by the Morin transition, at which point the perpendicularly aligned antiferromagnetic ordering will align parallel to the c-axis as it passes through the Morin temperature T_M. The value of the Morin temperature is found to be independent of grain size for grain sizes of $20\mu m$ to 6mm with a

value of $\sim$ 240-260K [Özdemir et al. (2008)]. For smaller grain sizes the Morin temperature is dependent on the grain size, with smaller particle sizes exhibiting a greatly decreased T_M. A hematite particle of 8-20nm will typically go through the Morin transition at $\sim$ 4K [Bødker et al. (2000)].

Chapter 3

Micromagnetic Modelling

3.1 Introduction

This chapter gives a brief overview of recent developments in the field of micromagnetic modelling, reviewing some of the major advances within this field since its beginning in the 1930s. Also discussed is the micromagnetic model used within this body of work, originally created by Wyn Williams and Philip Ridley of the University of Edinburgh and Bangor University respectivley, which has been used in prior studies [Williams and Dunlop (1989), Evans et al. (2006), Williams et al. (2010)].

The work outlined in Chapter 2 and Chapter 3 sections 3.2, 3.3, 3.4, 3.6 and 3.7 are descriptions of well recognised mathematical and experimental techniques, or, in the case of section 3.7, well known magnetic theory. The work in these sections was not undertaken by myself. The work following section 3.7 was personally undertaken throughout this project.

The micromagnetic code used within this study relies on a finite element method (FEM) written entirely using FORTRAN 95 and uses several library functions within the group of ODEPACK (second order partial differential equation) solvers [Brown et al. (1989)]. Both a description of the finite element discretisation and also the mathematics used to describe the individual energies

within the magnetic system are discussed. The micromagnetic code uses both an energy minimisation and a dynamic solver to obtain a stable magnetic domain structure. The energy minimisation, although relatively fast computationally, is prone to false convergence and may follow unrealistic paths. The dynamic solver utilises the Landau-Lifshitz-Gilbert equation. The dynamic solver takes far longer than the energy minimisation to converge, however, the solution is far more robust [Williams et al. (2010)]. To be as efficient as possible a combination approach is adopted where the energy minimisation is executed followed by the dynamic solver, where the final energy iteration becomes the initial solution for the dynamic solver. The FEM method is advantageous to this study as it allows irregularly shaped geometries to be modelled, like those seen within nature, compared to the fast Fourier transform (FFT) method which requires a regular grid. Finally, contained within this chapter is a discussion of the adaptations made to allow the micromagnetic code to handle models that require multiphase geometries and subsequently some examples of the multiphase code using theoretical situations are given.

3.2 History

Due to the role of magnetic structures within technology, such as magnetic storage used within the computing industry, understanding and exploiting the effects of such structures is of great importance [Cowburn (2002)]. Micromagnetic modelling gives one the ability to examine systems of magnetic particles and also allows the exploration of magnetic systems that would otherwise be either too complicated or financially inefficient to examine in any other way. Prohibitive costs would make some experimental studies impossible.

The first micromagnetic calculations, as previously mentioned in Chapter 1, were carried out in 1935 by Landau and Lifshitz [Landau and Lifshitz (1935)]. These first calculations considered only certain energy contributions of the system and were applied to a simple system comprising of a domain wall contained within

an infinitely large system. A major development within this field came during the 1960s with the inclusion of the individual moments within domain wall structures to describe the interactions within these regions, as opposed to the original practice of using a continuous vector to describe the transition between adjacent domain structure. These calculations were carried out in 1963 by [Fidler and Schrefl (2000)]. Since the 1980s micromagnetic modelling has advanced greatly, mostly due to the increasing accessibility of more advanced and more powerful computer processors which have allowed the modelling of larger structures and far more complicated systems containing multiple interacting grains. Such models have allowed the further examination of magnetic effects such as intergrain exchange and magnetostatic interactions and their effect on the coercivity and remanence within a system [Fukunaga et al. (1999)]. Models have also been generated to examine the long range magnetic forces between magnetic grains and the effects of exchange coupling within systems [Ramesh et al. (1988)].

3.3 Comparison of Models with direct observations

In order to fully examine the fidelity of micromagnetic models it is important to be able to compare simulations with direct observations. It is this ability to directly observe micromagnetic structures, at the nanoscale, which has allowed one to both better understand these magnetic systems and permitted the development of micromagnetic modelling. As mentioned in the previous section the increased need to understand the magnetic recording properties of grains at the sub-micron level has made it necessary to directly observe such structures to further advance these technologies.

3.3.1 Off-axis electron holography

In response to this need, the process of off-axis electron holography, an extension of transmission electron holography, has been developed and is now being increasingly used throughout the sciences. This technique has been applied extensively within the material sciences, although it is also being used within the field of Earth sciences [Harrison et al. (2002)] and biological sciences. With regards to the latter, many images have been created of the off-axis magnetic field within magnetosomes produced by nanoscale chains of magnetite, or in rarer cases goethite particles. Within the geosciences, holographic microscopy allows us to observe the in-plane magnetic structure within samples used for palaeomagnetic interpretations. All the holograhy images within this body of work have been supplied by Rafal Dunin-Borkowski, Takeshi Kasama, Joshua Feinberg and Nathan church, these images have been produced in both the University of Cambridge and the Danish Technical Institute.

3.3.2 Physical generation of holography images

Holographic microscopy works using a similar set-up to the conventional transmission electron microscopy set-up. Off-axis holography, now the predominant method for holographic microscopy, is used in this technique as opposed to the more traditional process of 'in-line holography'. The main difference between these methods is the inclusion of a Möllenstedt-Düker biprism within the former method which has been used within this study [Midgley (2001)]. The biprism is a charged wire with the role of tilting the reference wave with respect to the imaging wave which causes the interference of the two waves and ultimately the production of the hologram [Tonomura et al. (1986)]. This technique relies heavily on highly coherent electron sources to ensure the phase difference is an effect of the sample only. Physical stability of the microscope is also important.

As the reference wave is required to pass through a vacuum, it is most likely that the region of interest (ROI) within the sample being used is at the edge.

A consequence of this is that often the depth will not be continuous within the ROI (see section 4.2). The voltage applied to the biprism is selected to obtain the best fringe contrast and this voltage will vary depending on the nature on the experiment.

3.3.3 Interpretation of holography images

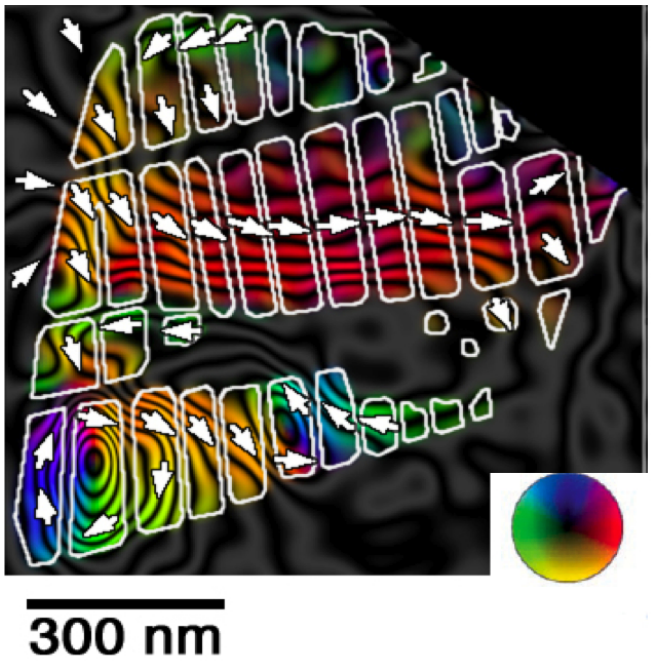

Figure 3.1: Off axis electron holography of a magnetite-ulvöspinel exsolution texture [Feinberg et al. (2005) and Feinberg et al. (2006)]. The white bounded highly coloured sections are the magnetite lamellae with the surrounding areas the ulvöspinel host matrix. The colour indicates the in-plane magnetic structure. Note the decrease in colour intensity in the centres of the vortex structures positioned on the second and sixth lamellae on the bottom row of lamellae.

The interpretation of these direct observations as seen in Figure 3.1 is as follows. The colour map indicates the direction of the magnetisation within the sample. In the case of Figure 3.1 blue indicates an upward magnetic direction with yellow a downward direction and so on, the intensity of the colours in the system is indicative of the magnitude of the magnetisation within the system. It is noticeable that some of the smaller magnetite lamellae in this system have

lower intensity associated with them than some of the larger lamellae, thus indicating a lower in-plane magnetisation. It is also important to observe a lower intensity at the vortex centres which this case are associated with the magnetisation being directed straight out of the plane. In Figure 3.1 the white arrows on the image also illustrate the direction of the magnetic field. All further electron holography images can be interpreted in the same way. It is prudent to mention that throughout this study micromagnetic numerical simulations which are comparable to direct observations will use the same colouring criteria as far as possible, as seen for example throughout Chapters 4, 5 and 6.

3.4 Finite element discretisation

This section examines the finite element method and how it is applied to a micromagnetic system. The finite element method has been used since the 1950s and 1960s mostly within the field of mechanical engineering, although it is now used extensively within many different fields. The region to be modelled is subdivided into a series of elements creating a mesh (Figure 3.2) of, in this case, linear tetrahedral elements. Each vertex of each tetrahedral element has a node associated with it and therefore each element can be described by a basis of four nodes [Zienkiewicz and Taylor (2000)].

This use of tetrahedral elements is particularly advantageous as it allows a finite element mesh to better conform to an irregularly shaped system. The mesh size, and therefore the node separation, will ultimately determine the resolution within the system.

Essentially a set of functions is defined which must be both continuously differentiable and also obey any boundary conditions applied to the problem. These boundary conditions are specific to the nature of the system that is being solved. An n-term solution ϕ_n is found such that we have equation 3.1 [Scholz (2003)].

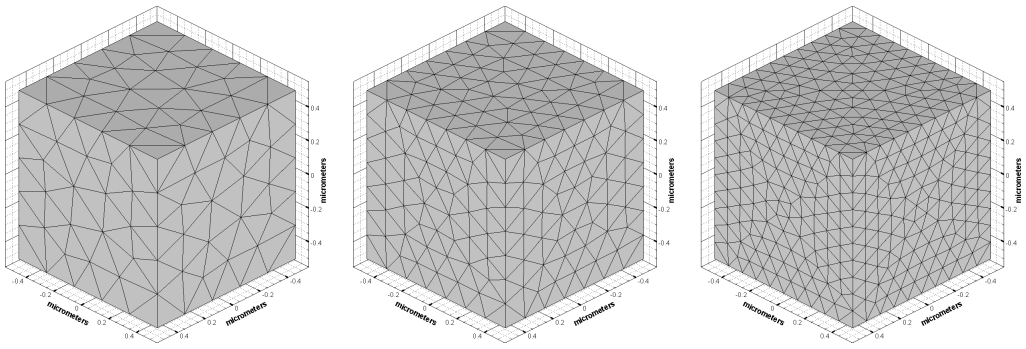

Figure 3.2: Examples of different mesh with varying mesh size applied to a cube geometry. From left to right the mesh size is decreased which in turn will cause an increase in resolution of the associated model and an increase in computation time.

$$\phi_n = \sum_{i=1}^{n} c_i \psi_i \tag{3.1}$$

In this expression all $\psi_i \in \Psi$, where Ψ is the trial function of the system. The parameters c_i are to be determined and therefore each individual element in the system has a trial function associated with it. The global solution of the system is simply the sum of all the individual trial functions within the system.

3.5 Geometry Generation

All the meshed structures are generated within a software package called CUBIT, containing both a geometry and mesh generation toolkit, computer aided design package (CAD), all produced by the Sandia corporation. CUBIT allows the generation of simple three dimensional (3D) geometries such as simple brick structures, cylinders and toroids where the defining dimensions such as lengths and radii can be user assigned. These simple geometries are used throughout the majority of the theoretical examples within this study. However, CUBIT also allows the bottom up generation of 3D geometries of an irregular nature. This system of generation allows much more freedom with the geometries produced and is therefore used to produce all the irregular systems within this study.

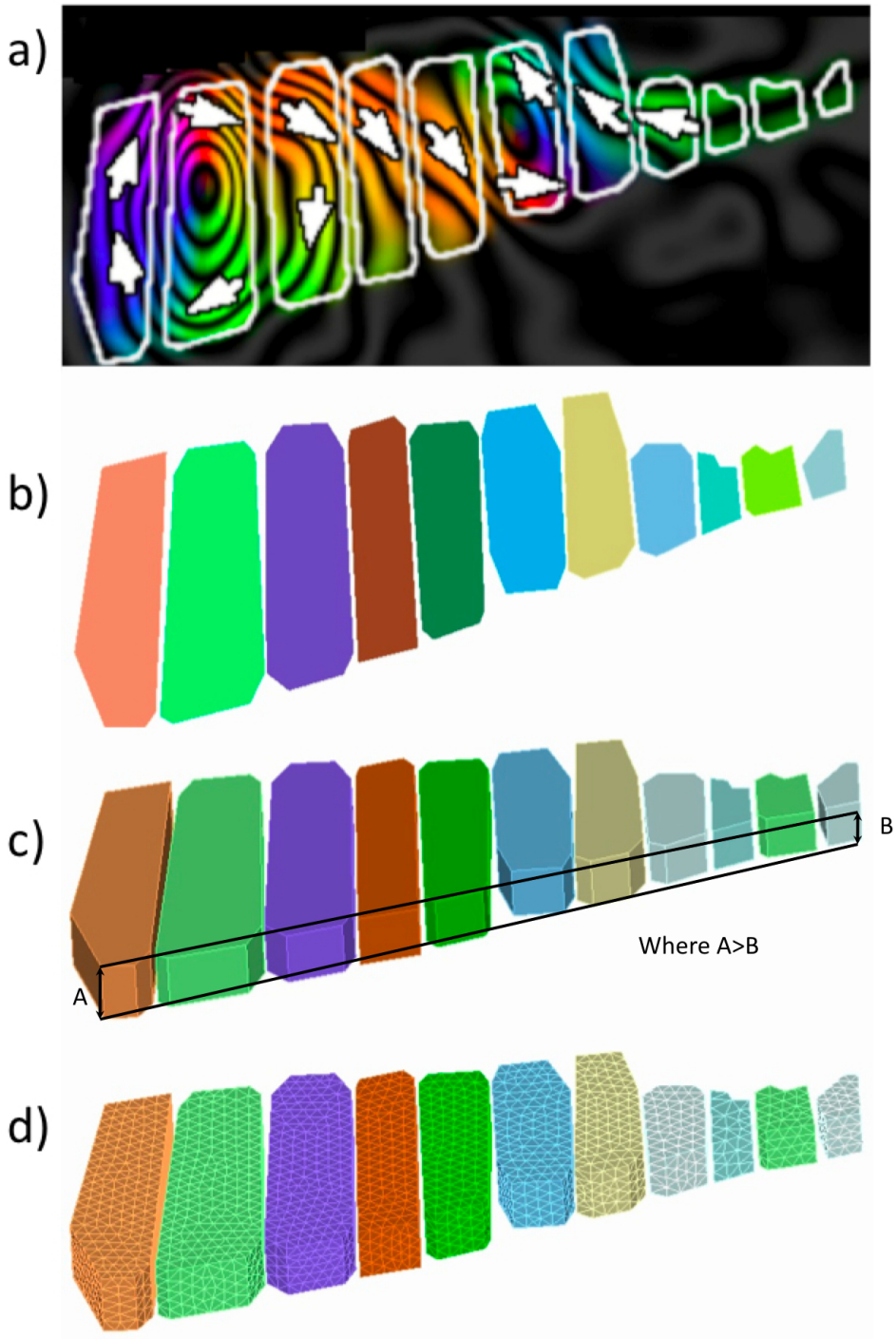

Figure 3.3: Geometry generation process from direct observation to 3D meshed structure. a) is the original 2D image where the grain boundaries are marked in white. b) shows the vertex generation of the 2D system. c) shows the lofted 2D system to make the 3D system and d) shows the 3D structure with the tetrahedral meshing criteria applied.

Irregular geometries of grains, matching those observed experimentally, are generated in the following way (Figure 3.3). Using the off-axis electron holography images a two dimensional geometry can be created. Firstly, points are placed round the boundary of the structures via a GetData a graph digitising package that returns xy coordinates for a selection of selected points. The outlines chosen for the structures are the best estimate of where the structure boundaries exist. These points are then used as coordinates to produce vertices within CUBIT and from these vertices an outline can be produced of all the individual blocks within the system. This outline can then be used to create a surface corresponding to the two dimensional (2D) holographic image of the structures. Finally these surfaces can be extended in the z direction to give the overall 3D geometry. The depths associated with each volume are an estimate based on the information available from the physical samples and a combination of simulations to find the optimum depth by examining the computational output. This process is described in greater detail within Chapter 4. Finally, this geometry is filled with a linear tetrahedral mesh.

This tetrahedral mesh can be altered in dimension to achieve a better fit to irregular geometries, however it must be noted that highly irregular geometries when meshed may result in poorly formed tetrahedral elements and can also cause difficulty within the modelling process. Within CUBIT an element block can be applied, the purpose of which is to assign a unique identification number (ID) to every node contained within the block where the node corresponds to a vertex of a tetrahedra. Each tetrahedral element therefore, is defined by a set of four node IDs. This information is exported as a unstructured mesh which includes the x, y and z coordinates of each node and an element list giving the node IDs contained in each element which allows the generation of the node connectivity for each element. This data is exported from CUBIT in either a genesis or patran file format. In the case of the genesis format this information is not ASCII and must be converted using the netcdf libraries.

The material constants and magnetic parameters that are used within the

micromagnetic code to define the material being modelled, such as initial field direction and intensity for the system, are read into the computer program from a separate input file. This file also contains various parameters necessary for initiating the library functions correctly. An example of an input file can be found in Appendix B. The material constants are applied to every single node in the system.

3.5.1 Interpreting model results

This section gives a brief overview on how model results are interpreted. Figure 3.4 gives an example of a model result of a simple geometry. This result is a normalised vector plot where each vector indicates the magnetic direction at each point within the geometry. The colouring of the vectors is proportional to the direction of the vectors. In the case of Figure 3.4 the colour blue denotes that the magnetisation is directed in the negative y direction and red the positive y direction. The axis in the top right hand corner indicates the axis rotation for this model. The use of colour within these models emphasises the magnetic structures seen within the models and, particularly within multiphase cases, allows differences between phases to be clearly observed.

Another method is used in the multiphase results and can be observed in Figure 3.5. To allow differences between different magnetic phases to be identified, even if the differences are extremely subtle, the geometry is displayed as partially transparent. With the transparent volume the vectors within the body of the geometry can also be observed. For additional clarity, planes within the geometry can be highlighted and coloured fully with respect to the vectors on that plane. In the example seen in Figure 3.5 three planes through the geometry have been highlighted: one in material 1, one in material 2 and one on the boundary. On comparing the planes in material 1 and material 2 it is evident that there is a difference between the two phases since the vortex is shaped differently. This difference, although subtle, is made more obvious by highlighting these planes as

it becomes immediately apparent that they are different. The other advantage is that, as a 3D geometry is being displayed as a 2D image, using the transparency the structure throughout the geometry can be observed more clearly.

All the multiphase structures within this chapter and Chapter 6, with the exception of the oxidation results, are displayed using the method shown in Figure 3.5, although unlike in this figure only two planes have been highlighted, one in material 1 and one in material 2.

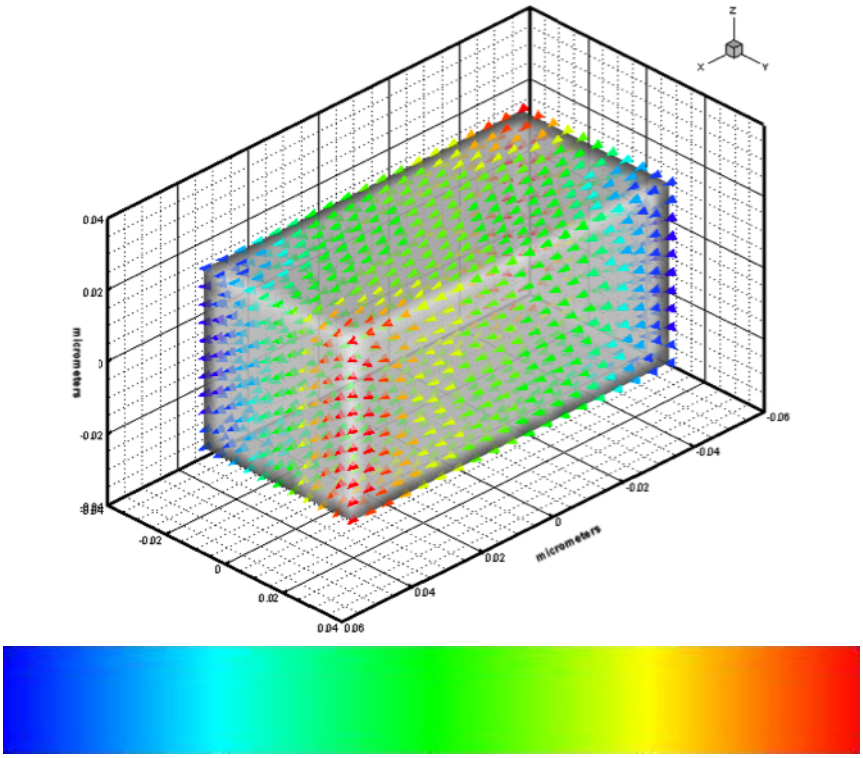

Figure 3.4: Image showing the model of a magnetite system. Along the bottom of the image is the colour bar which determines the direction of the magnetisation vector with respect to, in this case, the y plane where red denotes a positive y direction and blue a -negative y direction. The colouring is selected either to correspond to a direct observation or to give the best description of the magnetic structure.

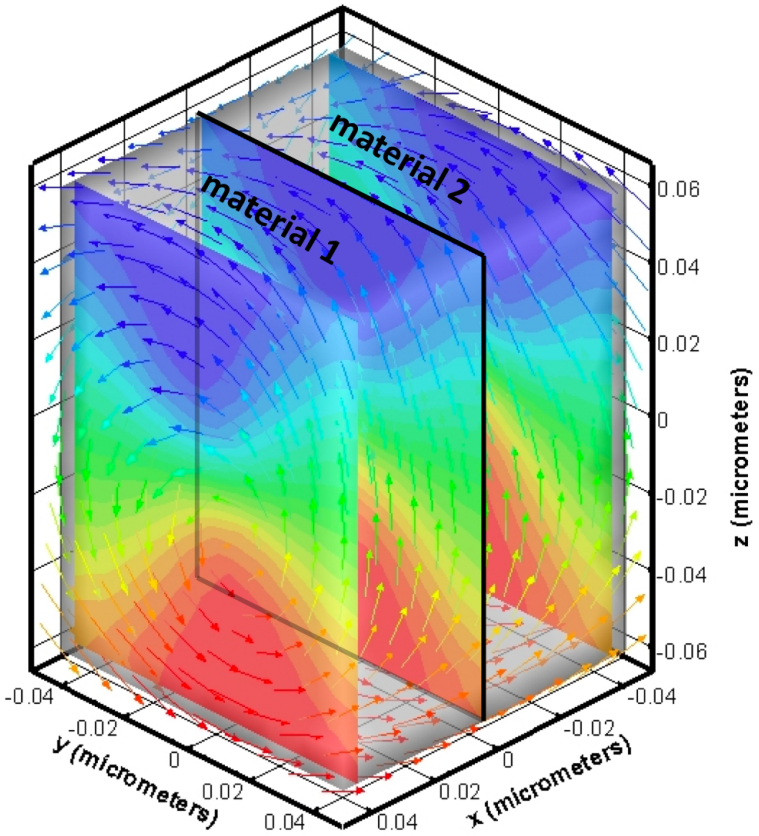

Figure 3.5: This image is of a multiphase structure split through the x plane. In this example three faces through the structure have been fully coloured in corresponding to the vectors on the surfaces. In this example faces in materials 1 and 2 have been highlighted and also the boundary face between the two materials.

3.6 Energy Calculations

Within the micromagnetic model the total energy of the system is a summation of the individual energy contributions. Both the energy minimisation and dynamic solver rely on this information. The following equation (equation 3.2) describes the total energy, the Gibbs free energy, for a volume V where the summation includes the exchange energy ($E_{A_{ex}}$), the magnetocrystalline anisotropy energy (E_{K1}), the external field energy (E_{ext}) and the demagnetisation energy (E_{demag}) of the system. The anisotropy and exchange energies are short range and calculated using local magnetisation information whereas the demagnetisation energy is long range and the energy density at any location needs the magnetic structure of the whole grain, or system of grains to be known.

$$\int_V \Big(E_{A_{ex}} + E_K + E_{ext} + E_{demag} \Big) dV \tag{3.2}$$

The following sections examine these energy contributions, in turn outlining the mathematics used to calculate them. The only one not included is E_{ext} as this calculation is trivial and uses a user defined external field direction and magnitude which is applied to every node within the system. The values of A_{ex}, Ms and K_1 are defined for every node within the system where these values are the exchange constant, saturation magnetisation and the first order magnetocrystalline anisotropy constant respectively.

3.6.1 Exchange Energy

The exchange energy of the system can be expressed as follows (equation 3.4) where A_{ex} is the exchange constant an M_s the saturation magnetisation.

$$E_{A_{ex}} = \int_V \frac{A}{M_s^2} |\nabla \boldsymbol{m}|^2 dV \tag{3.3}$$

$$\text{where} \quad |\nabla \boldsymbol{m}|^2 = \frac{\partial m_i}{\partial x_i} + \frac{\partial m_i}{\partial y_i} + \frac{\partial m_i}{\partial z_i} \tag{3.4}$$

The summation is over the entire volume and so is for all i where i is the number of nodes within the system and $\boldsymbol{m}$ the magnetisation associated with each node. Each node has an x, y and z magnetisation component.

3.6.2 Magnetocrystalline anisotropy energy

The magnetocrystalline anisotropy is related to how the magnetisation of the grain aligns with the crystallographic axis of the mineral being modelled. A magnetic system will have both easy and hard axes of magnetisation where greater energy will be required to align the magnetisation with the hard axes, and the easy axes are the minimum energy orientation for the magnetisation.

Further to this, anisotropy of a system will vary depending on the crystallographic structure of the system. The magnetite system can exhibit a cubic crystallographic system where the energy contribution can be expressed as shown in equation 3.5 and in all the proceeding models of magnetite. Unless explicitly stated a cubic anisotropy structure is assumed.

$$E_k = VK_1(\alpha_1^2\alpha_2^2 + \alpha_1^2\alpha_3^2 + \alpha_2^2\alpha_3^2) + K_2\alpha_1^2\alpha_2^2\alpha_3^2 \qquad K1 \ll K2 \tag{3.5}$$

As an approximation, uniaxial anisotropy is sometimes used and can be calculated as shown in equation 3.6, where the angle θ is calculated between the magnetisation vector and the easy axis of the system. Thus the maximum value is obtained at the point which the magnetisation direction is rotated to $90\,^\circ$ from the easy axis, being the maximum deflection from the easy axis which can be obtained. The value K_1 is the magnetocrystalline anisotropy constant for the material being simulated.

$$E_k = VK_1 \sin^2\theta \tag{3.6}$$

In the case of the cubic anisotropy structure the α values are the direction

cosines between the magnetisation vector and the x,y and z axis. The cubic anisotropy expression also contains a second term involving K_2, the secondary magnetocrystalline anisotropy constant. Due to the relative magnitudes of K_1 and K_2 only the first section of the expression is used for the energy calculation.

3.6.3 Demagnetisation Energy

The demagnetisation field, H_{demag}, of a magnetic system is the field produced to counteract the overall magnetisation of the system and can be expressed as follows (equation 3.7) and related to the magnetisation M with equation 3.8. This energy calculation is also the most computer intensive part of the model.

$$H_{demag} = -\nabla^2 \Phi \tag{3.7}$$

$$\nabla^2 \Phi = 4\pi \nabla \cdot \boldsymbol{M} \tag{3.8}$$

The potential Φ must be solved everywhere, both internally and externally in the system and therefore the total potential can be expressed as a summation of both the internal and external contributions of the entire system.

$$\Phi = \Phi_{internal} + \Phi_{external} \tag{3.9}$$

In equation 3.9 the $\Phi_{external}$ is calculated by integrating down on to the boundary surface. The internal contribution $\Phi_{internal}$ is solved such that the second order ordinary differential equation (equation 3.10) is obtained.

$$\nabla^2 \Phi = M_s \pi \nabla \cdot \boldsymbol{M} \tag{3.10}$$

Poisson's equation is therefore being solved, where boundary conditions can be applied to the system and where the Poisson equation, due to its nature is an elliptical value boundary problem. The general form of the Poisson equation is seen in equation 3.11 where ϕ and f can be either real or complex functions.

$$-\nabla^2\Phi = f \tag{3.11}$$

A mixed boundary condition using both the Dirichlet and Neumann conditions, outlined in the following list, is used to solve the system where s is a boundary surface element of the system and *g(s)*, *j(s)* and *h(s)* are all functions. This combination is used to account for both a boundary and non-boundary element within the system.

Dirichlet	$\Phi = g(s)$
Neumann	$\frac{\partial\Phi}{\partial n} = j(s)$
Mixed	$\frac{\partial\Phi}{\partial n} + \sigma(s)\phi = h(s)$

Rayleigh Ritz equation

As mentioned previousy, this problem, (equation 3.11) is solved using the Rayleigh Ritz method which is an example of the Galerkin method [Maier and Polizzotto (1987)]. The Galerkin approach allows us to convert a differential equation problem to a discrete problem.The shape matrix of the system can be expressed as shown in equation 3.13, where it is important to remember that each of the interpolating polynomials has the same number of terms present in the element. For example, for a triangular element, three terms would be required and for, in this case, a tetrahedral element, four terms [Davies (1985)].

$$N_e(x,y) = [N_1^e(x,y), N_2^e(x,y)...N_n^e(x,y)] \tag{3.12}$$

$$\text{where} \quad N(x,y) = a_0 + a_1x + a_2y \tag{3.13}$$

The polynomials $Ni^e(xy)$ are a set of interpolating polynomials chosen such that at the node coordinates (x_i, y_i) equation 3.14 holds. A full discussion of the formulation of the shape functions can be found in Appendix A.

$$\begin{aligned} &N_i^e(x_i, y_i) = \delta_{ij} \\ &\text{where } ij = 1 \ldots \text{s} \\ &N_i^e(x_i, y_i) = 1 \\ &N_i^e(x_j, y_i) = 0 \text{ where i} \neq \text{j} \end{aligned} \tag{3.14}$$

Using these equations the function $I[\phi]$ as shown in equation 3.15 can be expressed where the second term is the boundary condition imposed on the surface c_1 using the combined boundary condition constructed from both the Dirichlet and Neumann conditions mentioned previously.

$$I[\phi] = \sum_e \iint_R \left\{ \left(\frac{\partial \phi^e}{\partial x} \right)^2 + \left(\frac{\partial \phi^e}{\partial y} \right)^2 - 2\phi^e f \right\} dx\, dy + \sum_e \int_{c_1} (\sigma(\phi^e)^2 - 2\phi^e h)\, ds \tag{3.15}$$

The solution can then be obtained from the series of simultaneous equations formed from equation 3.16.

$$\sum_e \frac{\partial I^e}{\partial \phi_i} = 0 \tag{3.16}$$

Within equation 3.16, $\frac{\partial I^e}{\partial \phi_i}$ can be expressed as shown in equation 3.17.

$$\frac{\partial I^e}{\partial \phi_i} = \iint_{R_c} \left\{ \frac{\partial}{\partial \phi_i} \left(\frac{\partial \phi^e}{\partial x} \right)^2 + \frac{\partial}{\partial \phi_i} \left(\frac{\partial \phi^e}{\partial y} \right)^2 - 2 \frac{\partial \phi^e}{\partial \phi_i} \right. dx\, dy + \int_{c_1} \left\{ \sigma \frac{\partial}{\partial \phi_i} \left(\phi^e \right)^2 - 2 \frac{\partial \phi^e}{\partial \phi_i} h \right\} ds \tag{3.17}$$

A full description of this mathematical system can be found in greater detail in Davies (1985). These equations are solved using the DVODE solver, part of the Fortran ODEPAK suite of solvers. The DVODE solver uses a step process to solve systems of first order ordinary differential equations [Brown et al. (1989)].

3.7 Dynamic solver

The Landau Lifshitz Gilbert (LLG) equation (equation 3.20) describes mathematically how the magnetic moments within a material will rotate, through the process of Larmour procession, to align in their equilibrium positions [Kittel and Abrahams (1953)]. The equilibrium position will also correspond to the minimum of the energy in the system. In 1935 Landau and Lifshitz proposed a dynamical model for the processional moment of magnetisation as shown in equation 3.18.

$$\frac{\partial m}{\partial t} = -\gamma M \times H_{eff} \tag{3.18}$$

In this expression $\frac{\partial m}{\partial t}$ is the rate of change of the magnetisation and H_{eff} the effective magnetic field. The value γ is the gyromagnetic or magnetomechanical ratio of the system and is the ratio of the magnetic dipole moment of a system to its angular momentum. e is the electronic charge and m_e and c the mass of an electron and the speed of light respectively and the value g is the Landé splitting factor.

$$\gamma = \frac{g|e|}{2m_e c} \tag{3.19}$$

The dynamical system of magnetisation however is a dissipative system. As the Landau Lifshitz expression is technically a Hamiltonian expression which assumes that time is reversible, it can not fully describe a dissipative system. To correct for this, a dissipative term was introduced and this additional expression has the effect of forcing the magnetisation in the direction of the effective field.

$$\frac{\partial m}{\partial t} = -\gamma M \times H_{eff} - \frac{\gamma}{M} \times (M \times H_{eff}) \tag{3.20}$$

In 1955 Gilbert observed that Landau and Lifshitz's original expression could be derived from a Lagrangian formulation. However, in the case of this Lagrangian formulation the generalised coordinate system is instead expressed in terms of the M_x, M_y and M_z components of the magnetic system. Using this Lagrangian

analogy for the system, the easiest way to include a dissipative term within the system is to introduce a viscous force with components proportional to the time derivatives of the general coordinates.

$$\frac{\alpha}{M_s} \times \frac{\partial m}{\partial t} \tag{3.21}$$

Therefore the Landau Lifshitz with the Gilbert term becomes

$$\frac{\partial m}{\partial t} = -\gamma M \times H_{eff} + \frac{\alpha}{M_s} \times \frac{\partial m}{\partial t} \tag{3.22}$$

The value α is the dampening parameter used for the system. Throughout this study α will always take a value of one. Testing has been done to examine the effect of α on systems. The modification of α has a negligible effect on the system as a whole but does increase substantially the computation time to solve the system. For example, the following models show identical systems where only the Gilbert damping constant has been altered to take the values of 0.01, 1 and 100 (Figure 3.6). As can be observed, this drastic altering of α has little to no effect on the final solution for the system, the only difference being the time taken to converge to the solution, which varied from minutes to hours depending on the value chosen.

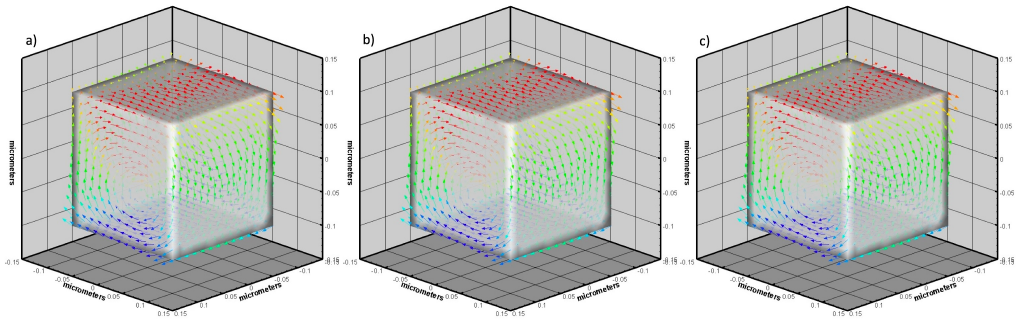

Figure 3.6: Figures a), b) and c) show that there is no effect using three different values of 0.01, 1 and 100 from images a) to c) on the magnetic strucure of the system.

3.8 Modelling magnetic materials with more than one magnetic phase

3.8.1 Geometry Generation

As the magnetic constants K_1, M_s and A_{ex} of the system are defined at each node, to model a system containing more than one material it is necessary to be able to distinguish to which material each node belongs. A further consideration is to recognise that there will be boundaries within the system between different materials. To do this the geometry generation is more complex than that seen in section 3.5. Although the distinct bodies are created in the same way as in section 3.5 there now exists a situation where some bodies are in contact, and therefore have one or more common surfaces.

The effect of this can be seen in Figure 3.8 where we have a large magnetite block containing three smaller magnetite blocks. The overall result of this model should be identical to that of the magnetite block seen in Figure 3.7 without the three interior blocks. However comparing the results of Figure 3.8 and Figure 3.7 we see that this is not the case. Instead we in Figure 3.8 b) that the overall structure is not SD as in Figure 3.7 but instead exibits a vortex structure. In addition to this it can be seen in Figure 3.8 c) that the interior blocks have a magnetic structure which is very much independent from the encapsulating outer block. Thus interaction is required across the boundary between the two structures.

To solve this problem the coexistent boundaries are merged to create one shared boundary. If Figure 3.9 image b) is now examined, it can see that when using this meshing criteria we obtain the same result as obtained in Figure 3.7 where the structure was designed as one solid block. The merging, shown in Figure 3.10, has the effect of collapsing any boundaries in contact into one shared surface, thus a sharp boundary exists between the structures with a set of shared nodes on that boundary surface as can be seen in Figure 3.10 image c). It is

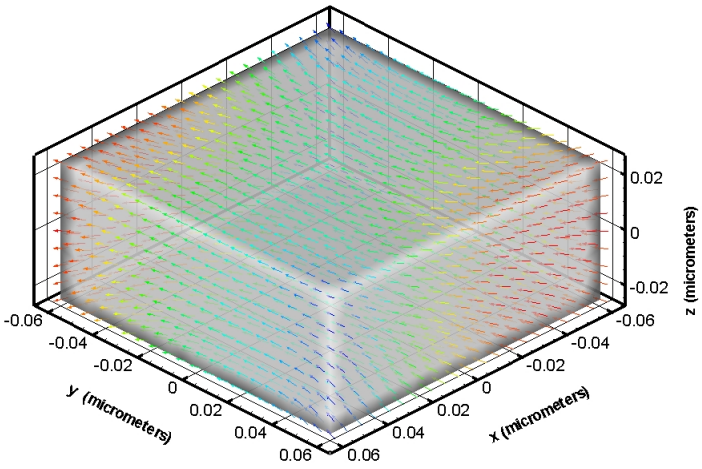

Figure 3.7: A model of a homogeneous magnetite block. In this case the system has a SD structure.

assumed that for all these multiphase systems, all boundaries between materials are sharp.

The second step is to apply groups to the exported geometry. Two groups contain the node IDs which belong to each of the materials and a further group is selected which contains those node IDs which are on the boundary between the two materials. When this information is used by the model it allows each node to have a material flag applied to it. Initially all the material flags are given a value of 0. If the node belongs to material two the flag is then changed to a 1 and lastly if the node belongs to a boundary the flag value is changed to 2. It is important that the information is read into the code in the correct order as the flags are overwritten each time new information is read in.

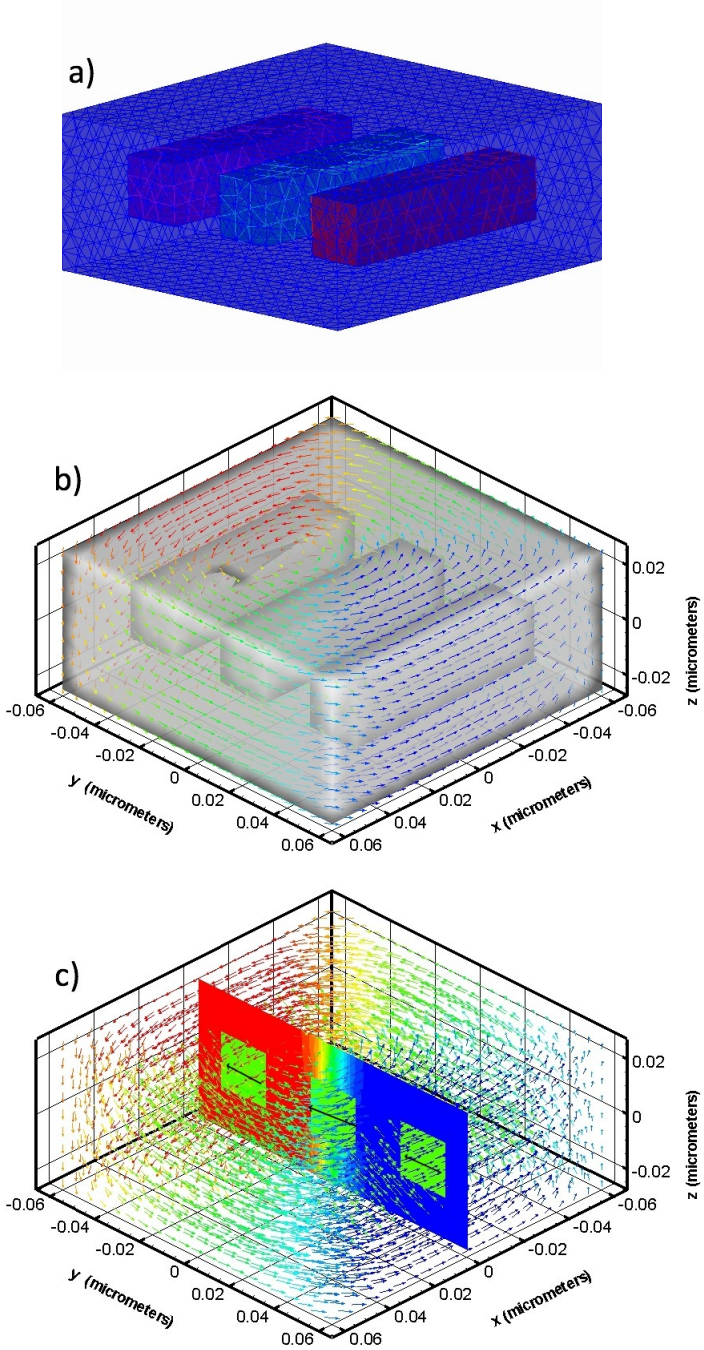

Figure 3.8: Image shows the magnetite block with identical dimensions to Figure 3.7 although containing three smaller magnetite blocks. Image b) shows the overall magenic strucure of this system. Image c) highlights the differences in structure between the smaller blocks and the surrounding block. The cross section is green for the interier blocks indicating a homogeneous magnetisation as indicated by the arrows. The remainder of the cross section is coloured showing the overall vortex strucure in the rest of the block. Also imortant is that this overall strucure differes from that seen in Figure 3.7

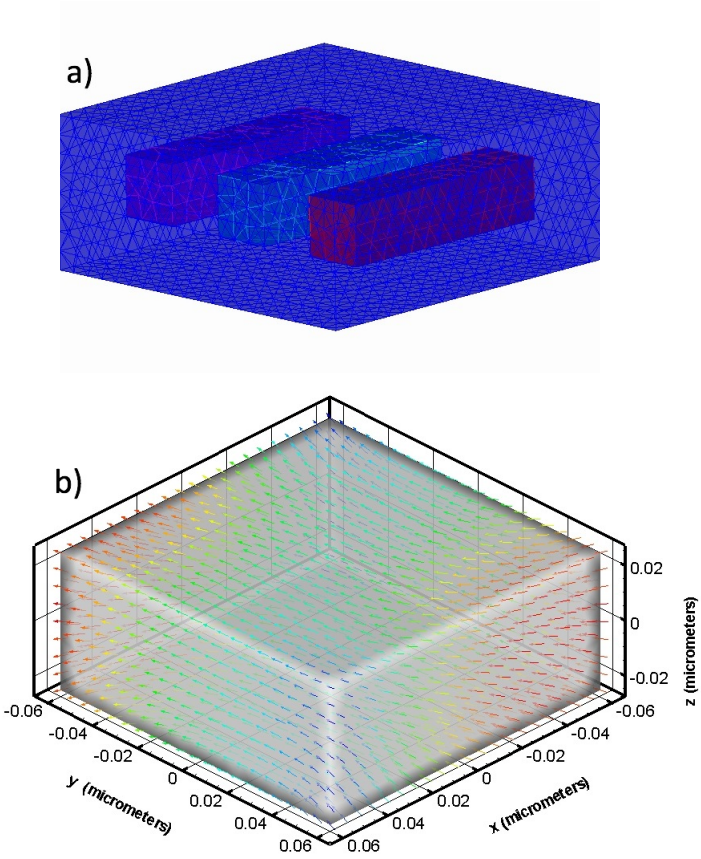

Figure 3.9: In this figure image a) shows the geometry used with three smaller magnetite blocks within the larger magnetite block from Figure 3.7, however this time the merging criterion has been applied. Image b) shows the result of this with the magentic strucure being identical to that seen in Figure 3.7.

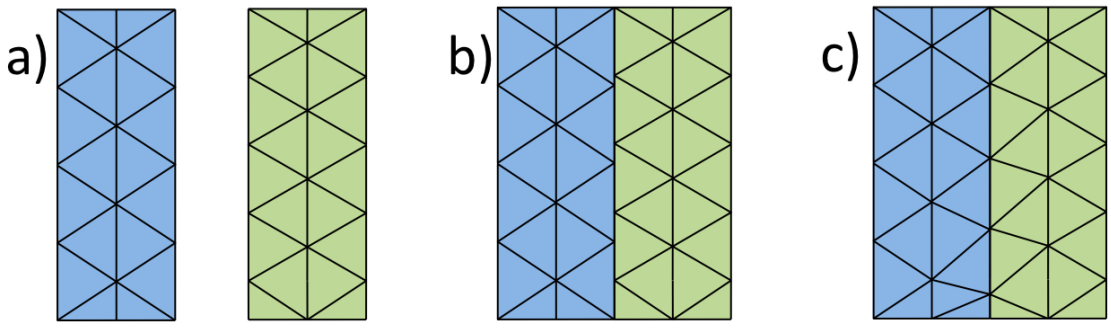

Figure 3.10: From left to right we have: image a) two geometries, image b) the two geometries with a boundary between the two, however, we can see that the nodes on the boundary do not match up thirdly we have image c) where the merging criterion has been applied and the nodes are coincident on the boundary.

3.8.2 Energy Revisions

The behaviour across a material boundary in a system is largely unknown. For all subsequent models, unless explicitly stated, the constants on the boundary between the materials are calculated as an average of the material constant for the adjacent materials.

However, a number of models were run to examine the effect of altering the constants on the boundary nodes. This was done by running models where the boundary nodes took the value of one of the materials and not an average value. Varying which material the boundary belonged to caused a negligible effect on the overall observed magnetic structure.

Furthermore, a multiphase system was modelled where the change in the constants was more gradual across the boundary. This was done by extension of the geometry generation in section 3.8.1. where another two sets of nodes were selected at either side of the boundary as seen in Figure 3.11 images a) and b). These sets of nodes were then given their own unique set of constants which could be either more similar to the material constants or the boundary constants or could take an average value of both the boundary and material constants.

Figure 3.11 shows the results where a graduated boundary has been altered in size. A geometry with x and y dimensions of 0.1 μm and a z dimension of 0.02 μm was created. Two boundary regions were applied to this geometry, one extending a distance of 0.01 μm on either side of the boundary (Figure 3.11 a) and c)) and the other a distance of 0.025 μm (Figure 3.11 b) and d)). The constants used within this system can be seen in Table 3.1 where only M_s has been altered to give a simple test case.

It is evident that altering the mid-layer has a pronounced effect on the overall magnetic structure observed. The first model with 0.01μm mid-layer has a far less gradual transition from material 1 to material 2 than can be seen in the model with a 0.02 μm mid-layer.

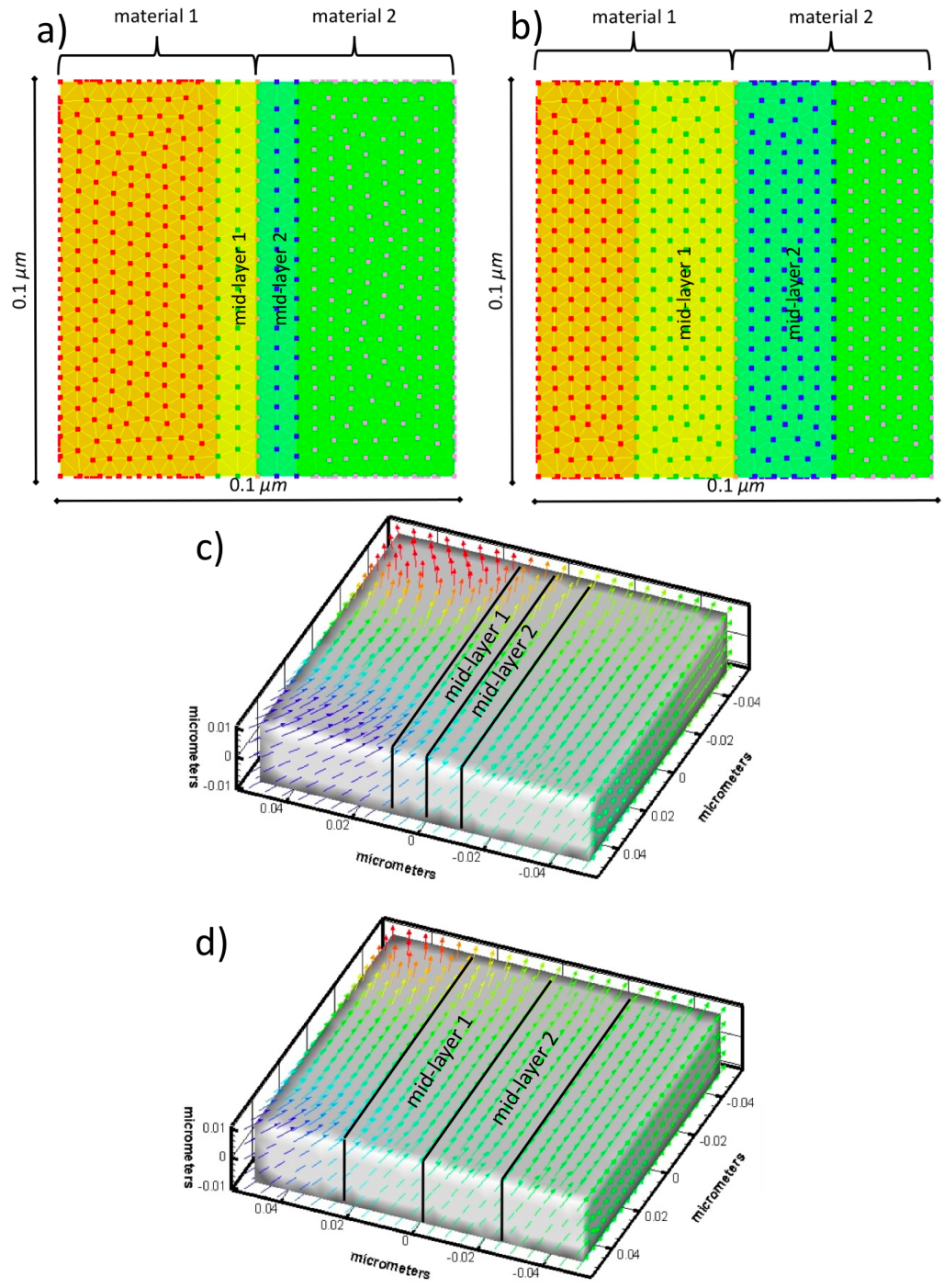

Figure 3.11: Images a) and b) show the geometries including where the mid layers extend 0.01μm and 0.025μm from the boundary respectively. Images c) and d) show resulting models of the 0.01μm 0.025μm mid-layer. Image c) with the smaller mid-layer shows a less gradual transition between the two materials than the example using the larger mid-layer in d). The values of the materials are given in Table 3.1.

Table 3.1: Values used for Figure 3.11 values for magnetite (Material 1) are from Heider and Williams (1988) and Hunt et al. (1995)

Constant	Material 1	Material 2
Magnetocrystalline anisotropy (K_1)	$-1.24 \times 10^4 J/m^3$	$-1.24 \times 10^4 J/m^3$
Exchange (A_{ex})	$1.34 \times 10^{-11} J/m$	$1.34 \times 10^{-11} J/m$
Saturation magnetisation (M_s)	480 kA/m	48 kA/m

3.8.3 Multiphase Results

This section contains some results using the multiphase model. A simple SD system showing some flowering was generated similar to that seen in Figure 3.4. This geometry, as seen in Figure 3.4 was split down the xy plane and a number of models were run altering the material properties within one side of the system. Table 6.3 contains the material properties used for each side of the volumes shown in Figures 3.12 to 3.14.

The subsequent models will all have one half of the geometry with a magnetite structure (labelled volume 1, image a) in each of the Figures 3.12 to 3.14 show the full magnetite structure) and the other half, volume 2, with constants similar to magnetite. The colouring of the systems is not uniform as the colour maps have been chosen to best highlight the magnetic structures of the individual systems. In addition to favourable colouring of the magnetic structure, the back and front faces, one belonging to each material of the system have been highlighted so that the difference between the two materials is as clear as possible.

The first Figure (Figure 3.12) shows two materials, volume 1 magnetite, volume 2 with M_s reduced where both systems use the uniaxial anisotropy criteria. As can be seen, the multiphase system incorporates the properties of both the single phase models. It can clearly be seen that the model with reduced M_s, in Figure 3.12 image b), has a far more homogeneous SD structure than the magnetite structure which exhibits flowering. In the multiphase structure, Figure 3.12 images c) and d), it can be observed that the reduced M_s part of the structure has a far more homogeneous structure than the magnetite section of the system.

In Figure 3.13 the effect of having volume 2 of the material with a reduced value of M_s and a cubic anisotrpy can be seen. The effect of this in the single-phase model, Figure 3.13 image b), is to have the overall structure perpindicular to that of the magnetite case in Figure 3.13 a) which follows the long axis of the material. The multiphase system, Figure 3.13 images c) and d), however, has the magnetite phase exhibiting a magnetic structure similar to that of the singlephase magnetite model yet is far more homogenous than volume 2 which now has a magnetic structure following the direction of the long axis of the volume.

In Figure 3.15 the effect of rotating the anisotropy of one phase is examined. In this case we see that the difference between the magnetite and altered magnetite phase are negligible.

Figure 3.14 has volume 2 as a magnetite with a reduced value of A_{ex}. This singlephase model of volume 2, Figure 3.14 image b), has a far more complex magnetic structure than the magnetite phase with a vortex structure in the zy-plane. The multiphase model, Figure 3.14 images c) and d), retains the vortex structure through the entirety of the structure yet the form of this vortex structure is not continuous through the boundary between the two materials as highlighted in the front and back surfaces of the volume.

The volume dimensions used and the alteration of the constants selected was done to give simple test cases. Further the contants were chosen as it was able to predict the effect they would have on the system. The results from these systems are in good agreement with what would be expected *e.g.* in Figure 3.14 a reduced value of A_{ex} would result in a less homogeneous structure which is observed in Figure 3.14 image b). Also using simple test case with dimensions in the SD range would imply that multiphase structures of these dmensions would be likely to inncorporate the magnetic structures of both volume 1 and volume 2 in the full structure.

Table 3.2: Constants for the following multiphase models, the figure to which the constants correspond is shown in the table. Each figure is annotated to make it clear which part of the structure is material 1 and which part is material 2.

Figure	Material	Material Constants A_{ex}, K_1, M_s, anisotropy form, Anisotropy rotation				
figure 3.12	Material 1	$1.34 \times 10^{-11} J/m$	$-1.24 \times 10^4 J/m^3$	480 kA/m	uniaxial	0°
	Material 2	$1.34 \times 10^{-11} J/m$	$-1.24 \times 10^4 J/m^3$	48 kA/m	uniaxial	0°
figure 3.13	Material 1	$1.34 \times 10^{-11} J/m$	$-1.24 \times 10^4 J/m^3$	480 kA/m	cubic	0°
	Material 2	$1.34 \times 10^{-11} J/m$	$-1.24 \times 10^4 J/m^3$	48 kA/m	cubic	0°
figure 3.15	Material 1	$1.34 \times 10^{-11} J/m$	$-1.24 \times 10^4 J/m^3$	480 kA/m	cubic	0°
	Material 2	$1.34 \times 10^{-11} J/m$	$-1.24 \times 10^4 J/m^3$	480 kA/m	cubic	45°
figure 3.14	Material 1	$1.34 \times 10^{-11} J/m$	$-1.24 \times 10^4 J/m^3$	480 kA/m	cubic	0°
	Material 2	$1.34 \times 10^{-10} J/m$	$-1.24 \times 10^4 J/m^3$	480 kA/m	cubic	0°

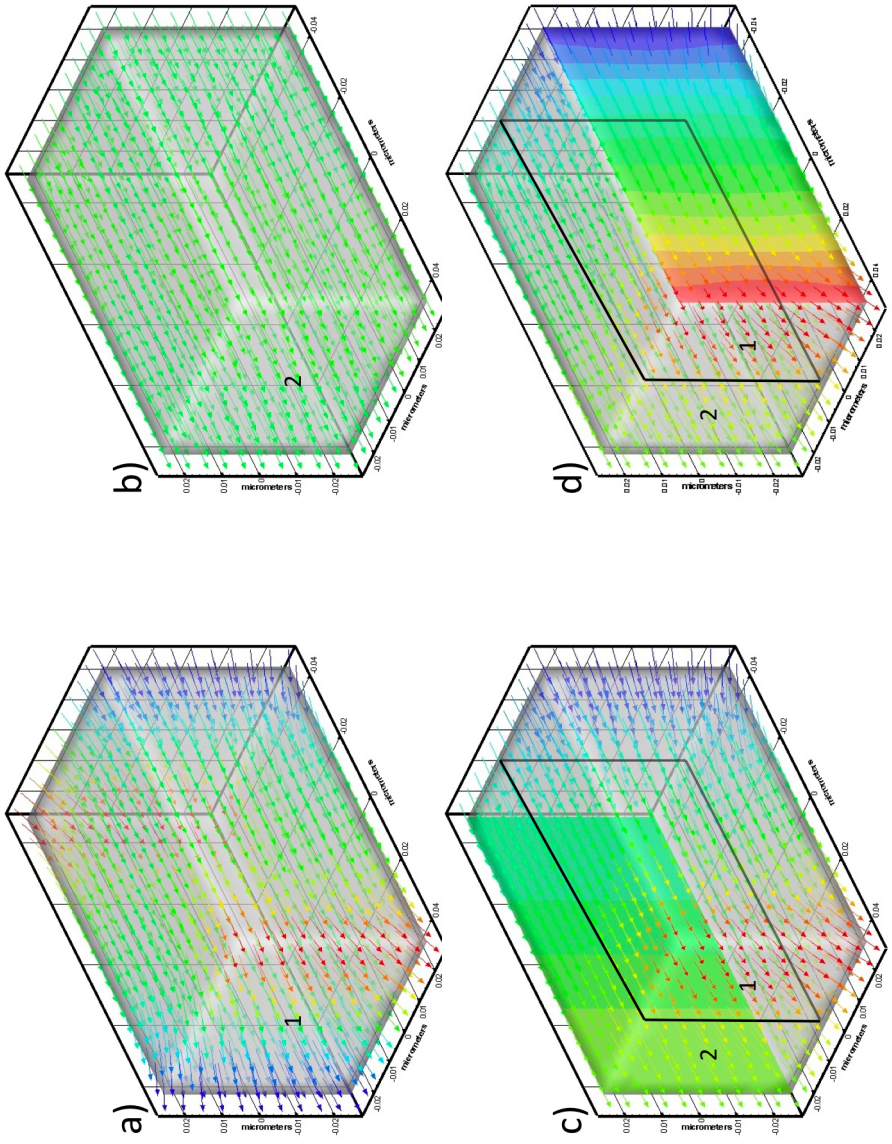

Figure 3.12: Figure showing both material one and material two in images a) and b) respectively.Images c) and d) show the multiphase model with image c) highlighting the magnetic structure in volume 2 and image d) the magnetic structure in volume 1. In this example the uniaxial anisotropy form has been used and the M_s value altered. In this case an increase in homogeneity can be seen in image b) and this structure is observed in volume 2 of the multiphase structure seen in images c) and d).

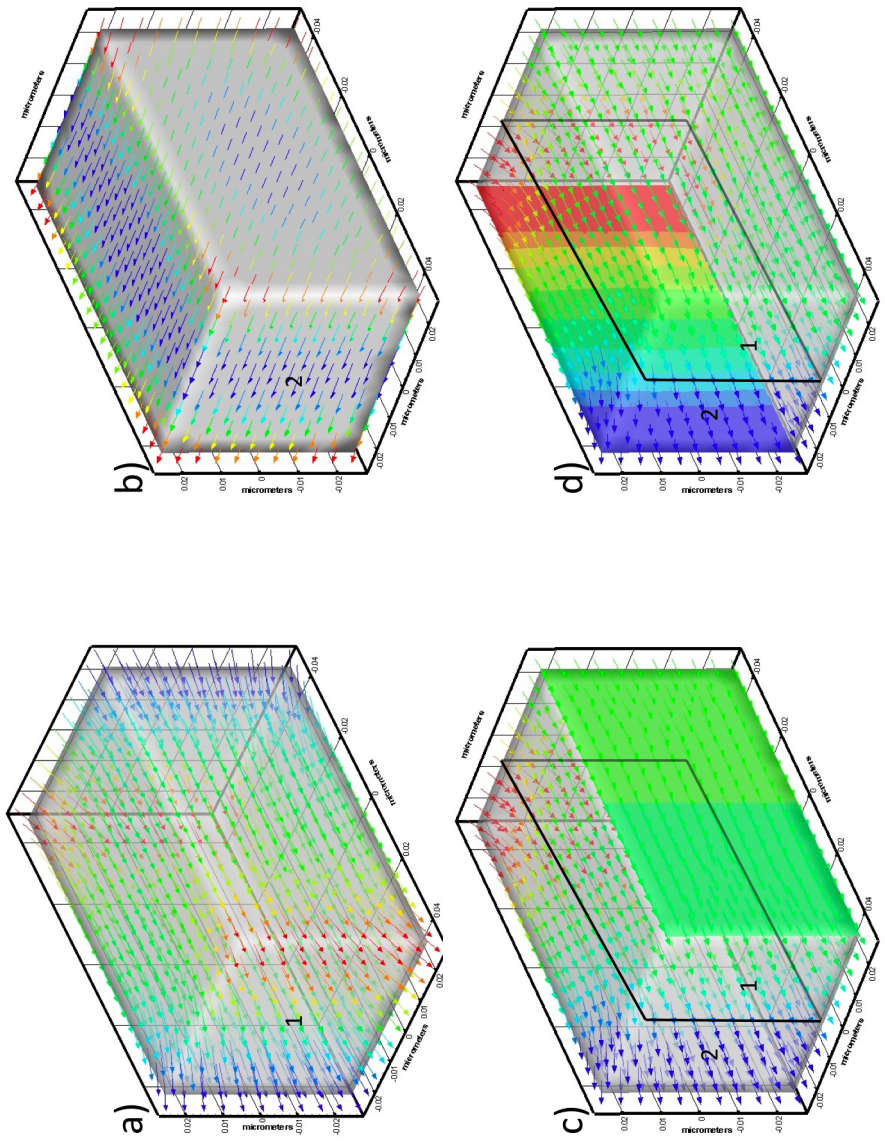

Figure 3.13: Figure showing both material one and material two in images a) and b) respectively. Images c) and d) show the multiphase model with image c) highlighting the magnetic structure in volume 2 and image d) the magnetic structure in volume 1. In this example the value of M_s has been reduced in volume 2 resulting in a the magnetic structure being perpendicular to that that seen in image a). In images c) and d) volume 2 is less homogeneous than volume 1.

Figure 3.14: Figure showing both material one and material two in images a) and b) respectively. Images c) and d) show the multiphase model with image c) highlighting the magnetic structure in volume 2 and image d) the magnetic structure in volume 1. In this example no difference is seen between images a) and b) and consequently the multiphase system in c) and d) appears no different to those systems in a) and b)

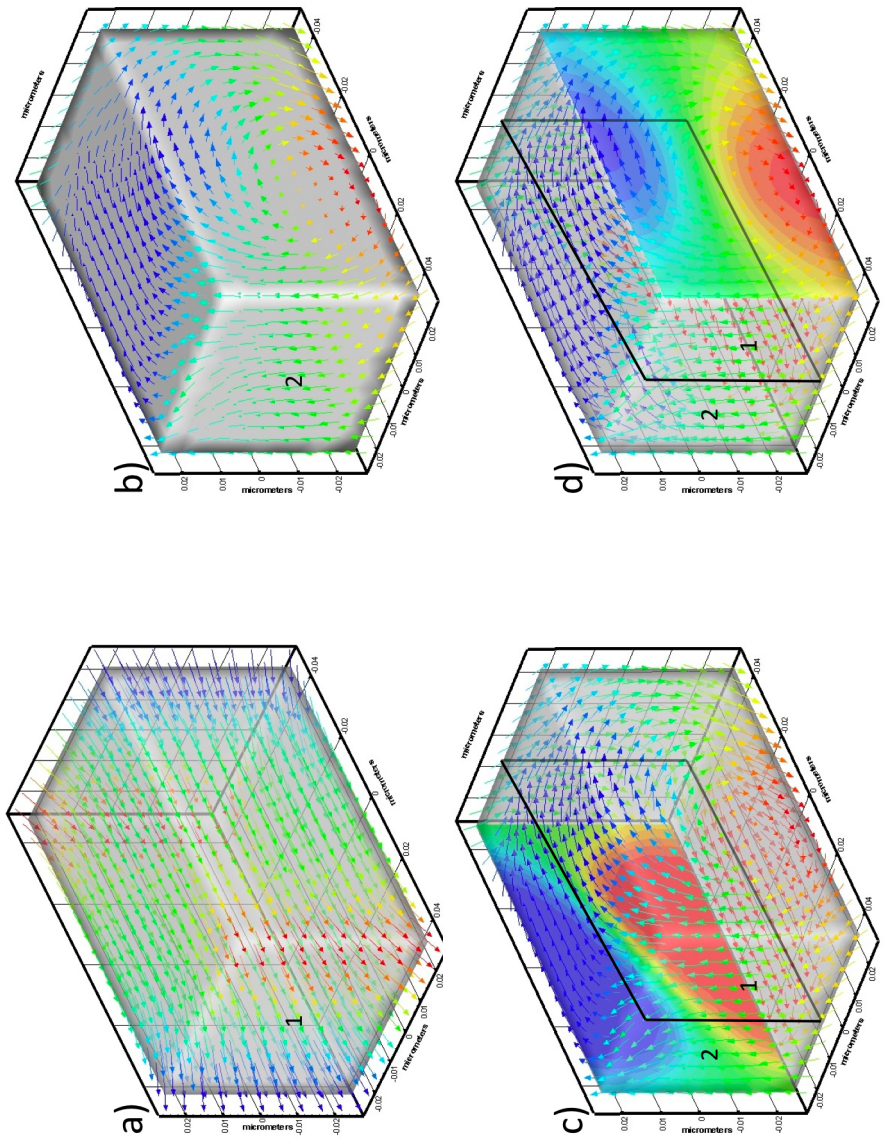

Figure 3.15: Figure showing both material one and material two in images a) and b) respectively. Images c) and d) show the multiphase model with image c) highlighting the magnetic structure in volume 2 and image d) the magnetic structure in volume 1. In this case image b) shows a very different strucure from image a). The multiphase strucure in c) and d) although resembling the structure in image b) more still exibits a change in strucure between the two phases.

Figure 3.16 has a geometry more similar to an exsolution texture with individual lamellae structures, this was done to test the multiphase using a structure more similar to the complex direct observation.s It can be seen in the single-phase model where the material is uniformly magnetite that the structure displays some flowering at the edges, although the centre of the structure is homogeneous. Figure 3.16 also shows the multi-phase results where the constants of the lamellae structures have been slightly altered. In image Figure 3.16 image b) can be seen the result of altering the value of M_s to $2.4 \times 10^5 J/m^3$, half that of magnetite, and in Figure 3.16 image c) the results of altering A_{ex} to a new value of $1.34 \times 10^{-12} J/m$, 10 times less than that of magnetite. Again, simple changes in the constants were chosen as in both cases as the effect of such changes is known.

In both cases in Figure 3.16 images b) and c), an increase is observed in the heterogeneity of the system regardless of the constant which has been altered. It can clearly be seen that the magnetite regions retain a similar structure to the overall structure observed when the system is entirely magnetite. In Figure 3.16 images b) and c) it can be observed that there is an increase in the flowering at the left hand and right hand edges of the system. It can be noticed that the regions adjacent to both the magnetite lamellae have a magnetic structure dissimilar to those same regions observed in the full magnetite model. The overall structures in these examples are in good agreement to what would be expected with these constant changes.

All the following multiphase systems within Chapter 6 use this multiphase model. Any differences in the approach used to model these systems will be discussed within the appropriate sections.

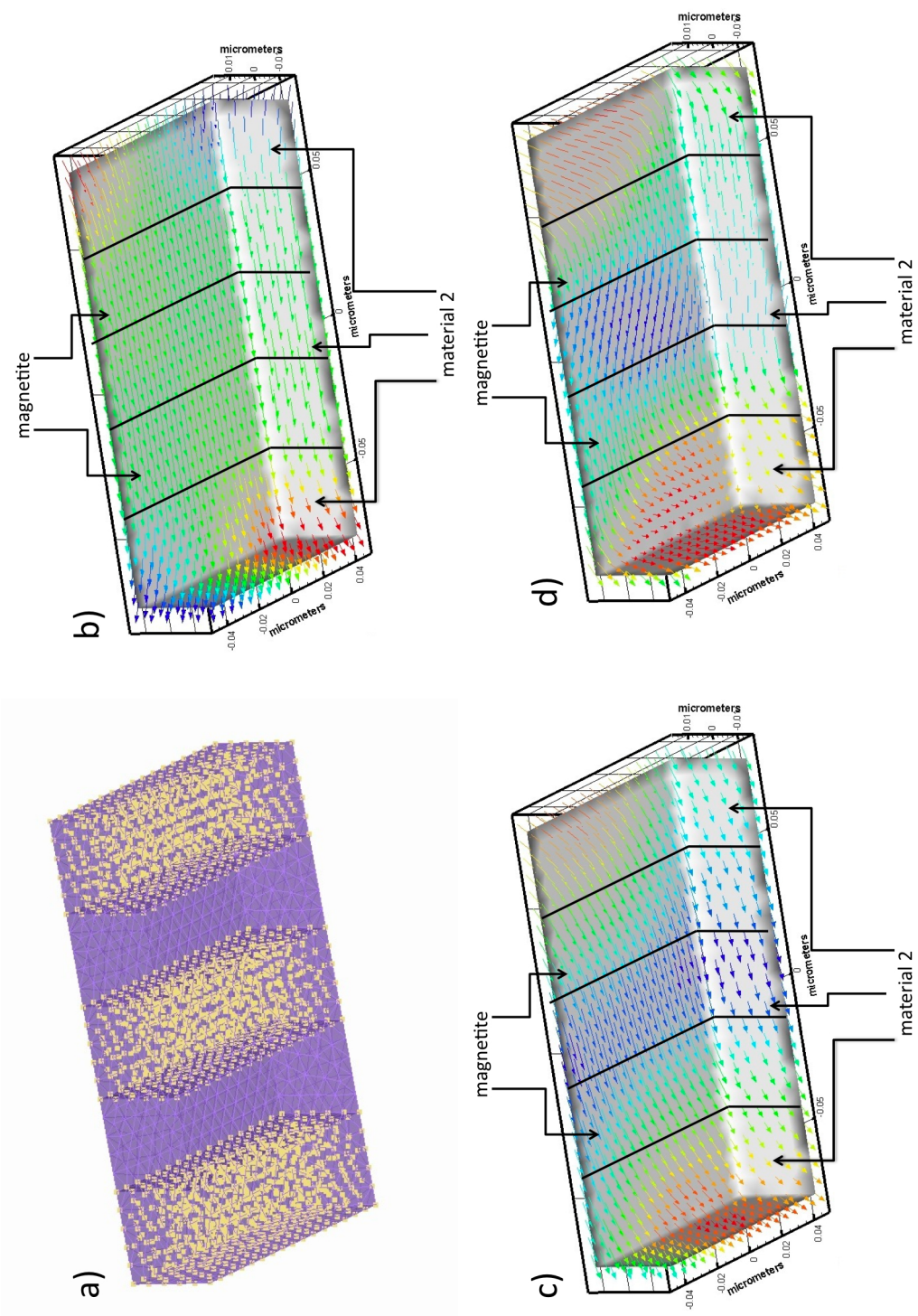

Figure 3.16: Figure showing a multiphase system where the yellow nodes indicate the regions which are attributed to the values of material two. Image a) shows the single-phase magnetite system. Images b) and c) show the results where only the values of M_s and A_{ex} are altered respectively.

Chapter 4

Applying FEM to Irregular Geometries

4.1 Introduction

The use of a finite element method (FEM) micromagnetic model, as previously discussed in Chapter 3, is particularly important as it allows the modelling of irregular structures. This chapter examines the results of some irregular structures that are often observed, and can be produced through both chemical and biogenic process.

We expect that grain shape will have a large effect on the resultant magnetic structure within the grain, as has been reported in a number of papers [Williams et al. (2010)]. Williams et. al. observed the importance of geometry in magnetosome chains where the smaller end structures greatly effect the overall strucure. In this chapter therefore, we examine the effects of geometry modification that may be un-resolvable from experimental observations but that may affect the form of the magnetic structure that is nucleated.

The effects of geometry modification are examined using two different systems. The first part of this chapter, section 4.1, examines a recently found irregular biogenic magnetite and the comparison between direct observations and models.

Section 4.2 examines how well direct observations can be used to create the mesh input for this micromagnetic model. This section describes some of the assumptions used to create the mesh inputs for the models. These assumptions have been used within the exsolved samples modelled throughout Chapters 5 and 6.

4.2 Geometry smoothing

A study was undertaken to examine the effect of edge shape on certain grain geometries. This was undertaken to determine if there were any significant alterations within magnetic structures when the geometry of the system was altered. Physical generation of the geometries to test this was performed by first creating the chosen geometry and then by blending, or smoothing, the edges of the geometries, where the degree of smoothing applied to the edges could be altered by changing the smoothing factor. In this case a cuboid geometry was constructed. Figure 4.1 shows the yz plane of this geometry, the smoothing factor is increased from 0.05 in Figure 4.1 a) to 0.2 in Figure 4.1 d). As the smoothing factor is increased the geometry changes from a cuboid with rounded corners to a cylinder.

4.2.1 Cuboid

Figure 4.2 shows a suite of simulations where the cuboid's x axis edges were subjected to edge smoothing criteria with a maximum smoothing producing a cylinder with diameter equal to that of the original cuboid's width. The cuboids are assumed to be magnetite and the constants used are found in Table 4.1. The magnetocrystalline anisotropy form of the system was assumed to be cubic.

The dimensions of these models were chosen as they are above the critical single domain (SD) size for magnetite and more comparable in size to those models seen in section 4.2.2. The effect of the four smoothing criteria can be seen in Figure 4.1 which shows the cross section of the yz plane where the long axis of

Table 4.1: Values used for Magnetite [Heider and Williams (1988) and Hunt et al. (1995)]

Constant	Value
Magnetocrystalline anisotropy (K_1)	$-1.24 \times 10^4 J/m^3$
Exchange (A_{ex})	$1.34 \times 10^{-11} J/m$
Saturation magnetisation (M_s)	480 kA/m

the cuboid is in the x direction. The models of the geometries of Figure 4.1 can be seen in Figure 4.2. A fine enough mesh was required so that the meshing could adequately represent the curvature of the edges. It can be observed that geometry adaptation like this does have an effect on the magnetic structure modelled within the system. This is particularly clear when viewing the yz plane of the system as the increased curvature of the edges results in the production of a vortex state around the x-axis. This structure is entirely absent in the geometry with the least smoothing and becomes more regular in the other geometries as the smoothing is increased.

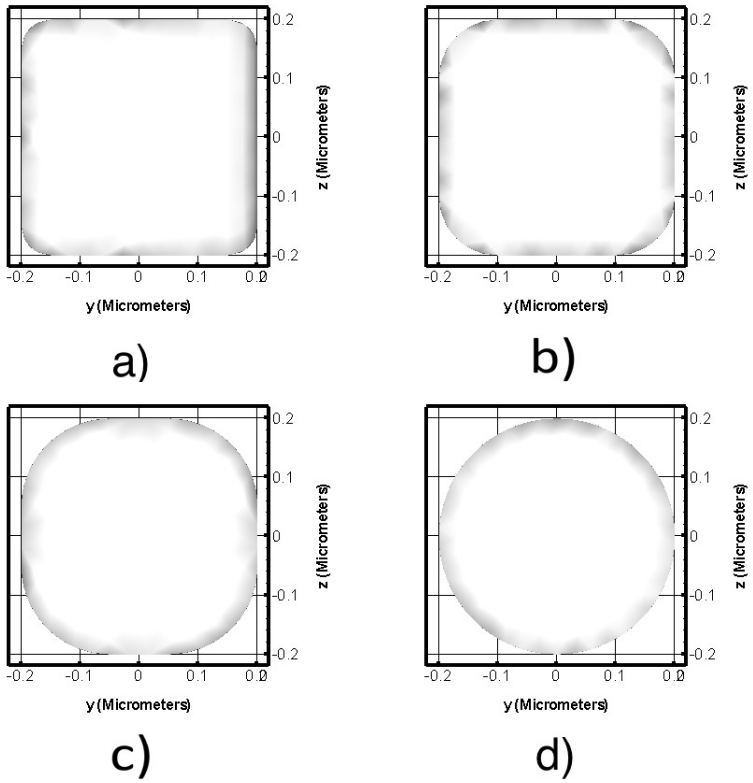

Figure 4.1: Figure shows the effect on the geometry when smoothing the edges of the system. These images show the yz plane of the cuboids modelled in Figure 4.2. Image a) shows a smoothing factor of 0.05, image b) 0.10, image c) 0.15 and image d) 0.20.

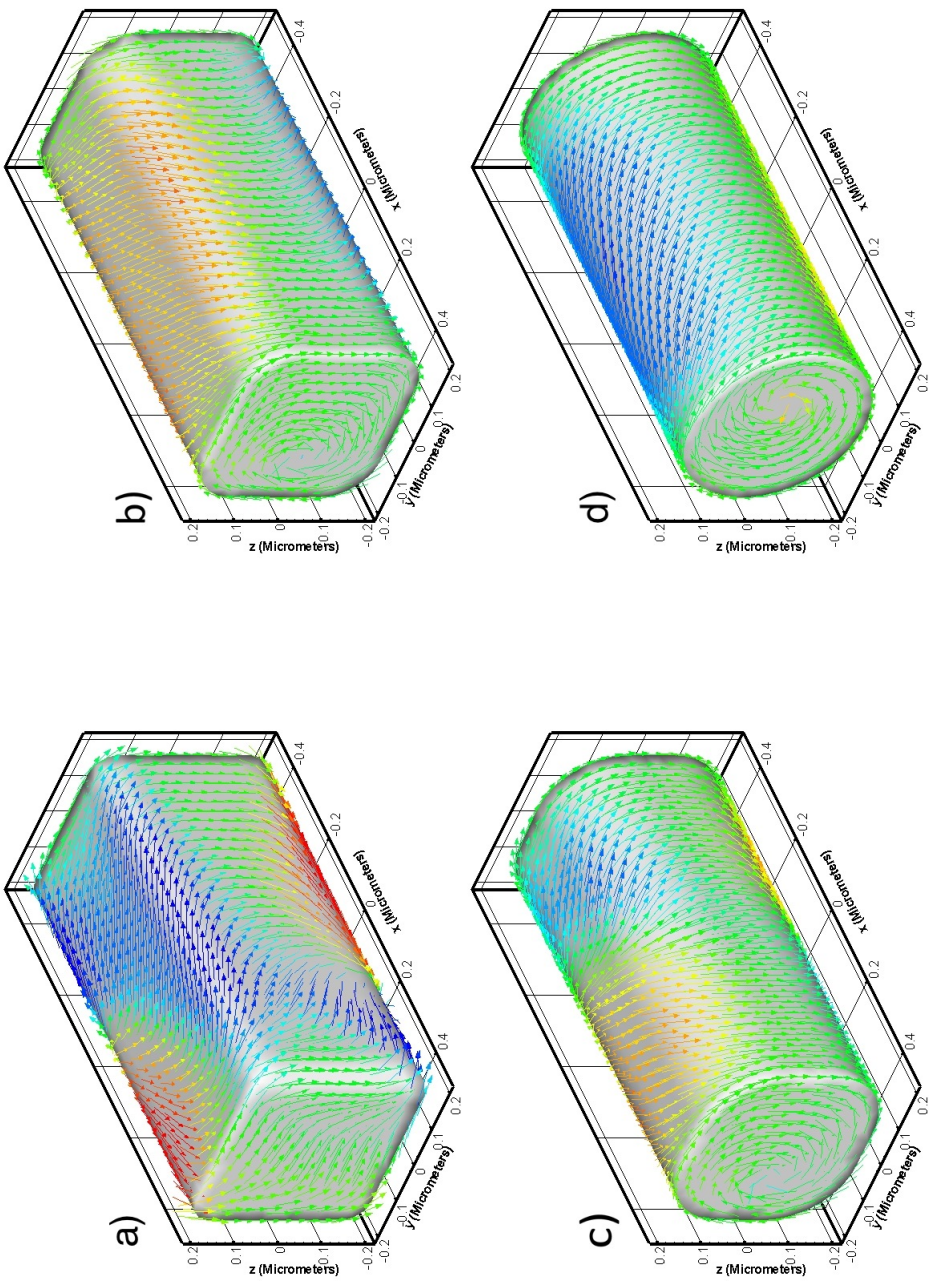

Figure 4.2: Figure containing the results for edge smoothing with images a)-d) having smoothing factors of 0.05, 0.1, 0.15 and 0.2 respectively. The meshing criteria is consistent throughout the models as is the applied colour map. As the curvature is increased from image a) to image b) we see the formation of a vortex structure centered on the yz face of the geometry and less variability in the magnetisation direction in the xy and xz planes. In images c) and d) we see the magnetisation more closely following the curvature of the geometry.

4.2.2 Irregularly shaped magnetosomes

It is well known that many magnetotactic bacteria use magnetite, and to a lesser extent goethite and greigite [Blakemore (1975), Kirschvink et al. (1985), Petersen et al. (1986), Bazylinski et al. (1994)], particles for magnetic sensing. These magnetic particles are produced by biosynthesis within the organism and take the form of magnetosomes - membrane bound chains of SD magnetic particles. The chains can exhibit a range of dimensions and often one chain will contain different dimensions of particles, frequently with smaller sized particles found at the ends bounding larger particles in the interior of the chain.

Ultimately the geometry adaptation used in section 4.2.1 were undertaken to examine the effect of smoothing topography on the magnetic structures discussed by Schumann et al. (2008). The structures, constructed of biogenic magnetite, are exceptionally large in comparison to most magnetosomes by several orders of magnitude. Although there are living bacteria with magnetosomes of a very similar shape they have maximum dimensions of approximately 170 nm [Kirschvink et al. (1985)]. These structures, seen in Figure 4.3 a), b) and c), exhibit a spearhead-type structure with the z-axis ranging from $2\mu m$ to $4\mu m$ and are found as single crystals a sketch of this structure is shown in Figure 4.3 d). These particles are from clay rich sediments spanning the Paleocene-Eocene Thermal Maximum (PETM) from a borehole in Ancora, New Jersey. It is hypothesised that these particles exhibit such large particle dimensions in response to the unique environment in which they were formed.

The off axis electron holography of Schumann et al. 2008 indicates that these large structures are SD in nature, which is contradictory to conventional domain theory where the SD threshold for magnetite is $0.08\mu m$ [Thomson et al. (1994)] (Figure 4.4). It is proposed by Schumann et al 2008 that this magnetic structure is a result of a pinning effect caused by the geometry of the structures disallowing more complex magnetic structures forming within the system.

It is on the basis of these contradictory results that micromagnetic modelling

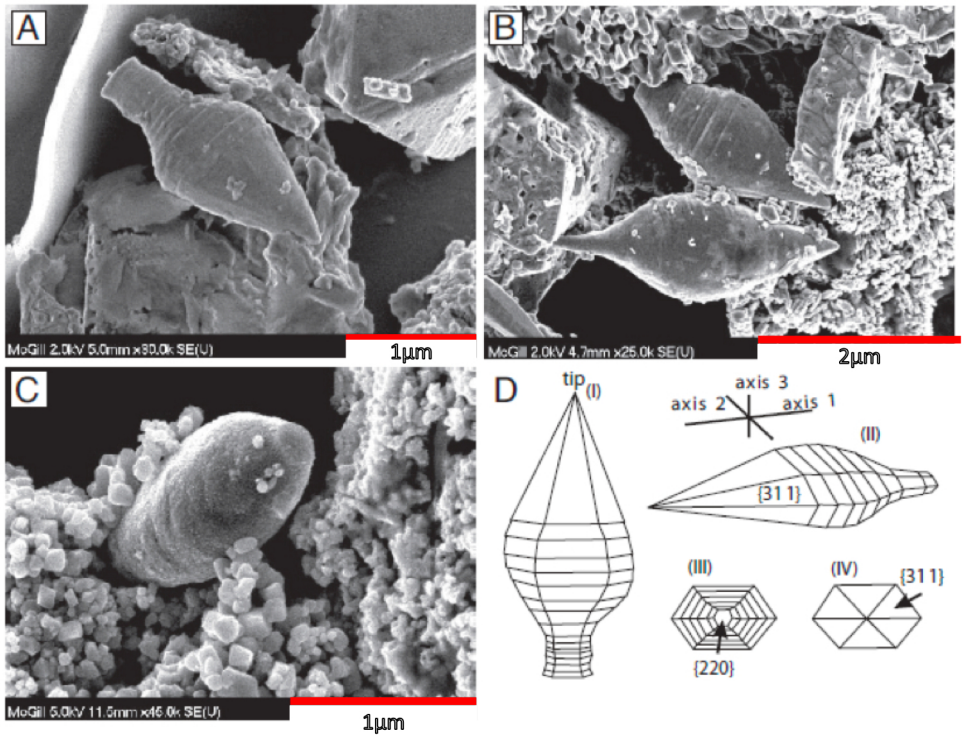

Figure 4.3: Figure taken from Schumann *et al* 1998, showing in images A, B and C the biogenic magnetites. Note particularly in C the smoothness of the samples. Image D shows the overall geometry of the structures.

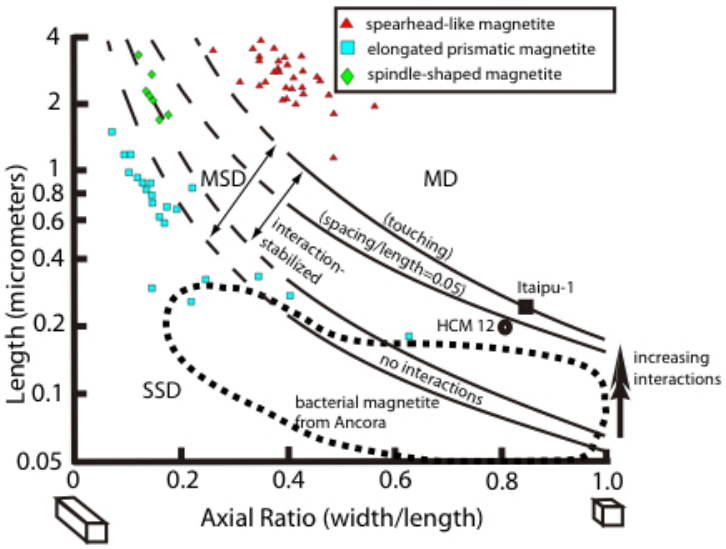

Figure 4.4: Figure taken from Schumann et al. (2008) showing the relationship between magnetite grain dimensions and magnetic structure. The structures used within this section are marked as the red triangles note how they plot within the MD section of the plot.

has been done to investigate if a micromagnetic simulation of these systems will also show a SD domain system. To do this a spearhead-like geometry was produced of similar dimensions. The dimensions used were at the smaller end of the reported size threshold for these structures as they would be more likely to exhibit a SD structure than the larger ones. Since it was suggested that the geometry played an important part in determining the overall magnetic structure, the structure of the geometry was altered to examine any possible effects from smoothing of the surface to examine what effect this would have.

4.2.3 Irregularly shaped magnetosome modelling results

The magnetite constants used in the micromagnetic model are given in Table 4.1 and the initial magnetisation direction was along the [010] direction which is also the long axis within this system. It is important to note that the samples are unlikely to be pure magnetite, however, for the purposes of modelling the

constants for magnetite have been used.The following images show the results of different levels of smoothing on the structure (Figure 4.5). It can be observed that in all cases the overall magnetic structure is not SD, i.e. a homogeneous magnetisation is not seen within the structure, although the structure does change considerably in response to the altered geometry. Various changes are evident as the smoothing of the system is altered, for example the vortex structure seen on the cylindrical stalk in the figures is evident in Figure 4.5 images a) and d) but absent in c) and d) further, the main vortex structure seen in the body of the spear changes direction from Figure 4.5 a) to b) and then again from c to d). However, overall these structures do not show a homogeneous magnetic structure and therefore do not behave as SD structures.

Subsequently, a selection of models were run with rotated anisotropy to examine any possible effect this may have on the resulting models (Figure 4.6). Again, despite these changes, it can be observed that these structures are not homogeneous and therefore would not display a SD magnetic structure. This result disagrees with those of Schumann et al. 2008 and could allude to inaccuracies in the imaging process. A multi-domain (MD) structure strongly indicates that their functionality would not be a magnetotactic one. It is possible, however, that the functionality of these structures was related to the non-magnetic properties of the structure.

It has been documented [Lowenstam (1962)] that magnetite has played a role in dentical capping in chitons radula or "teeth", the chiton being a primitive marine molusc. These teeth are used as tools to scrape sediments and ultimately aid in feeding. Magnetite is frequently found in these structures due to its hardness, although most studies find magnetite only as a percentage of the overall composition of these structures [Li et al. (1989)]. Additionally these structures would be of an appropriate geometry for these functions.

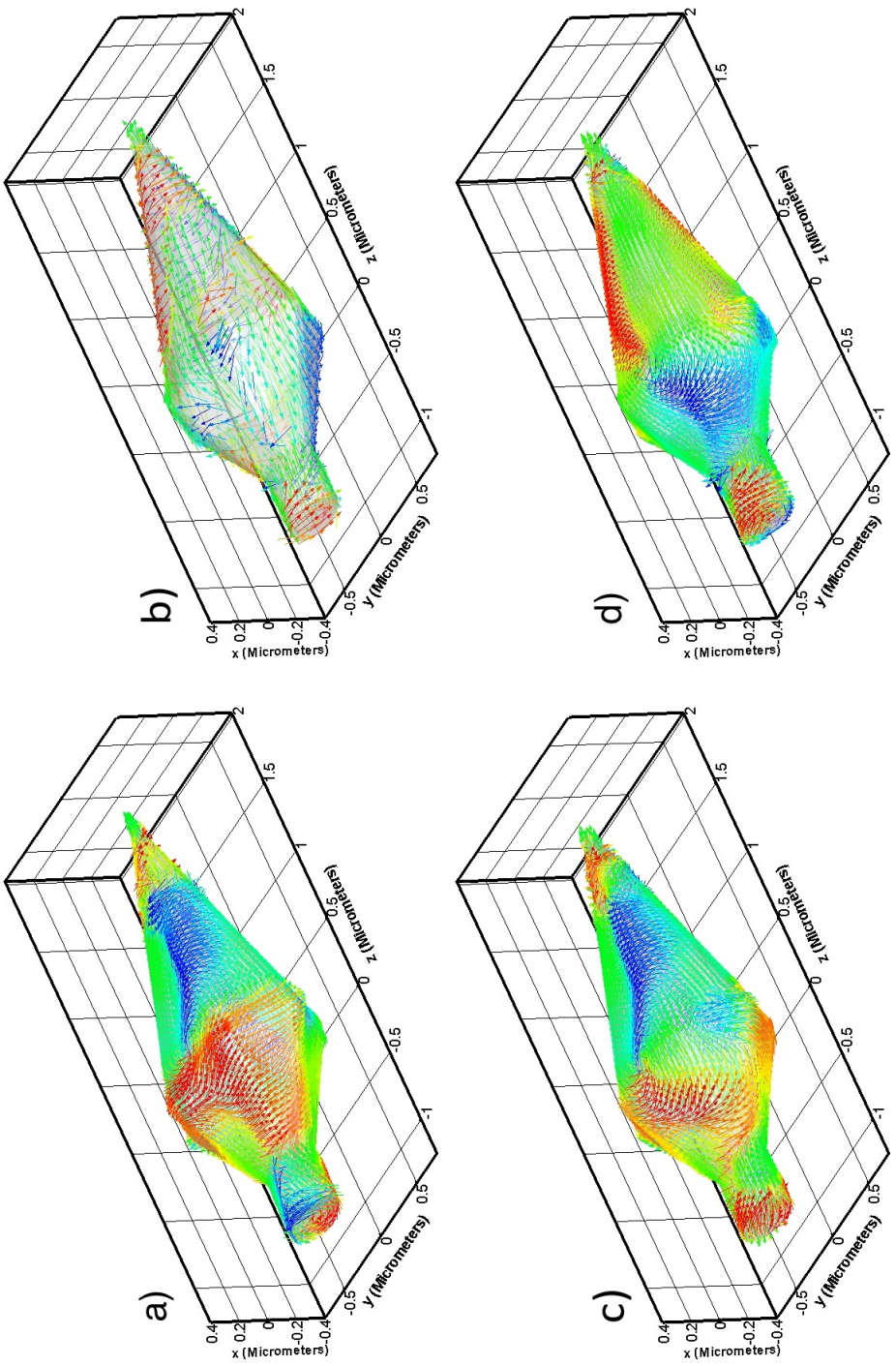

Figure 4.5: Series of models showing the magnetic structure of the geometry as the smoothing factor is increased. Model a) has no smoothing factor and b), c) and d) have factors of 0.05, 0.1 and 0.15 respectively. None of the images show a SD structure. A change in magnetic structure is seen as the smoothing is increased from a) to d). The main vortex reverses in direction from a) to b) and c) to d) and small vortex is in the stalk portion of a) and d) but absent in b) and c)

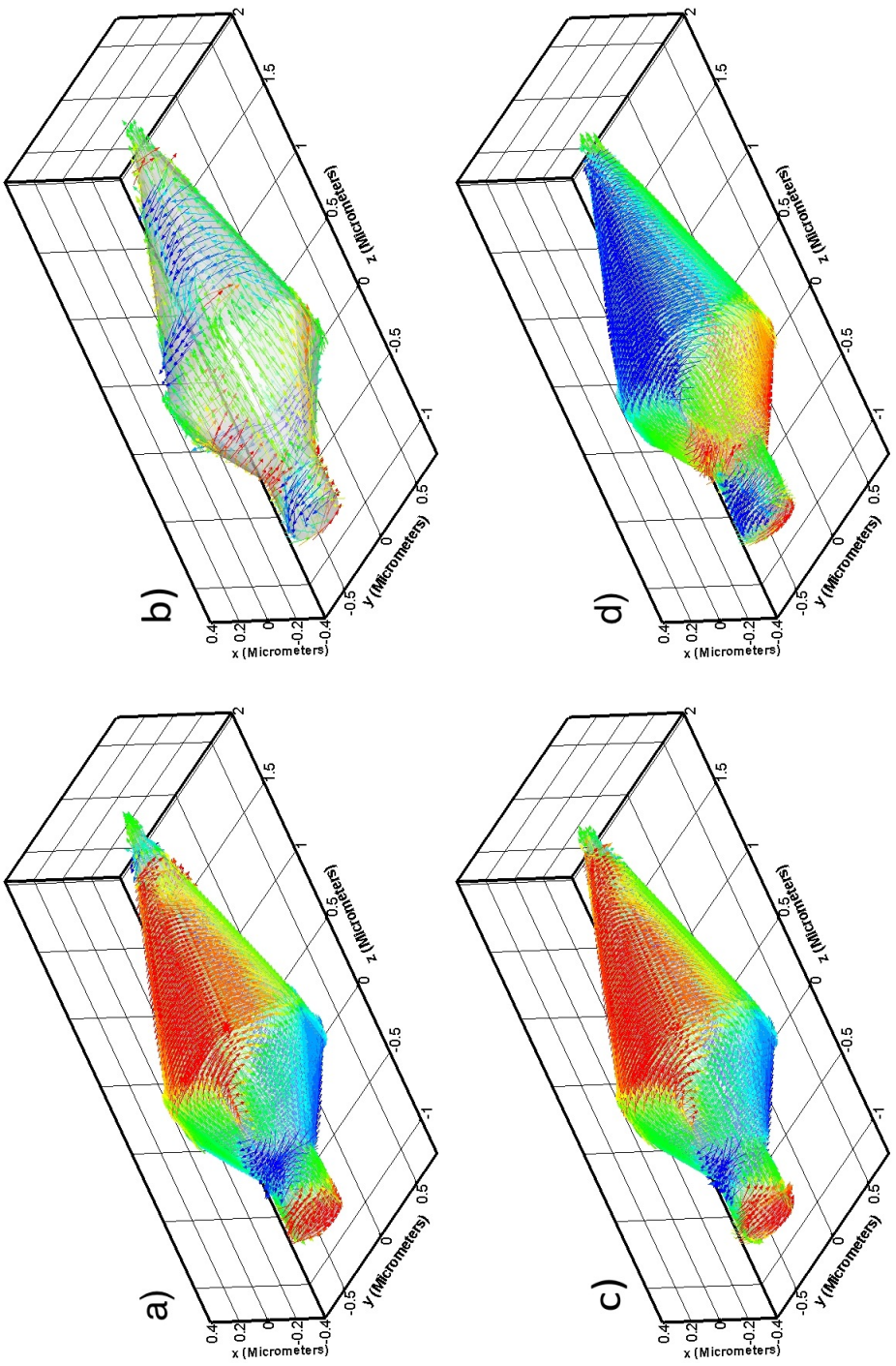

Figure 4.6: Series of models showing the magnetic structure of the geometry as the smoothing factor is increased. Model a) has no smoothing factor and b), c) and d) have factors of 0.05, 0.1 and 0.15 respectively. Additionally the anisotropy has been rotated around the x axis by 45°. None of the images show a SD structure. A change in magnetic structure is seen as the smoothing is increased from a) to d). The main vortex reverses in direction from a) to b) and c) to d) and small vortex is in the stalk portion of b) and d) but absent in a) and c)

4.3 Magnetite Lamellae

All the information used to generate the geometry of the irregular structures is shown in Figure 4.7 [Feinberg et al. (2005), Feinberg et al. (2006)]. The image also shows the Fe concentration map of the sample and a holographic transmission electron microscopy image. Also included on the concentration map are the associated thicknesses of the individual lamellae in nm; these are included as black numbers on alternate lamallae. As can be seen in Figure 4.7 this sample is actually a wedge with the lamellae to the far left being far thicker than the smaller blockier lamellae on the right. Furthermore it is difficult to ascertain exactly where the boundaries of the individual lamella are since the image does not have sharply defined edges to the grain. It can be assumed that the boundary between the phases is sharp [Evans and Wayman (1970)]. It is important to note that the entire sample is quite large, but only the bottom portion has been used for micromagnetic modelling. This is due to the entire structure being too large to model in its entirety, from this point on all the models of this system use only the bottom row of lamellae.

4.3.1 Effect of varying separation between neighbouring lamellae

Using the available information (Figure 4.7) as a starting point, various assumptions must be made in the generation of the lamellae geometry shown in Figure 4.7 such as; the exact thickness of the sample, how the depth varies from one lamella to the next and the distance between the lamellae. The first set of models were generated in order to examine the effect on the magnetic structure of the location of the boundaries between the individual lamellae and the host matrix. Two micromagnetic solutions were produced by varying the distance between the lamellae with the optimum solution, i.e. the soloution most closely resembling the direct observations, being chosen as the most likely geometry. It has been

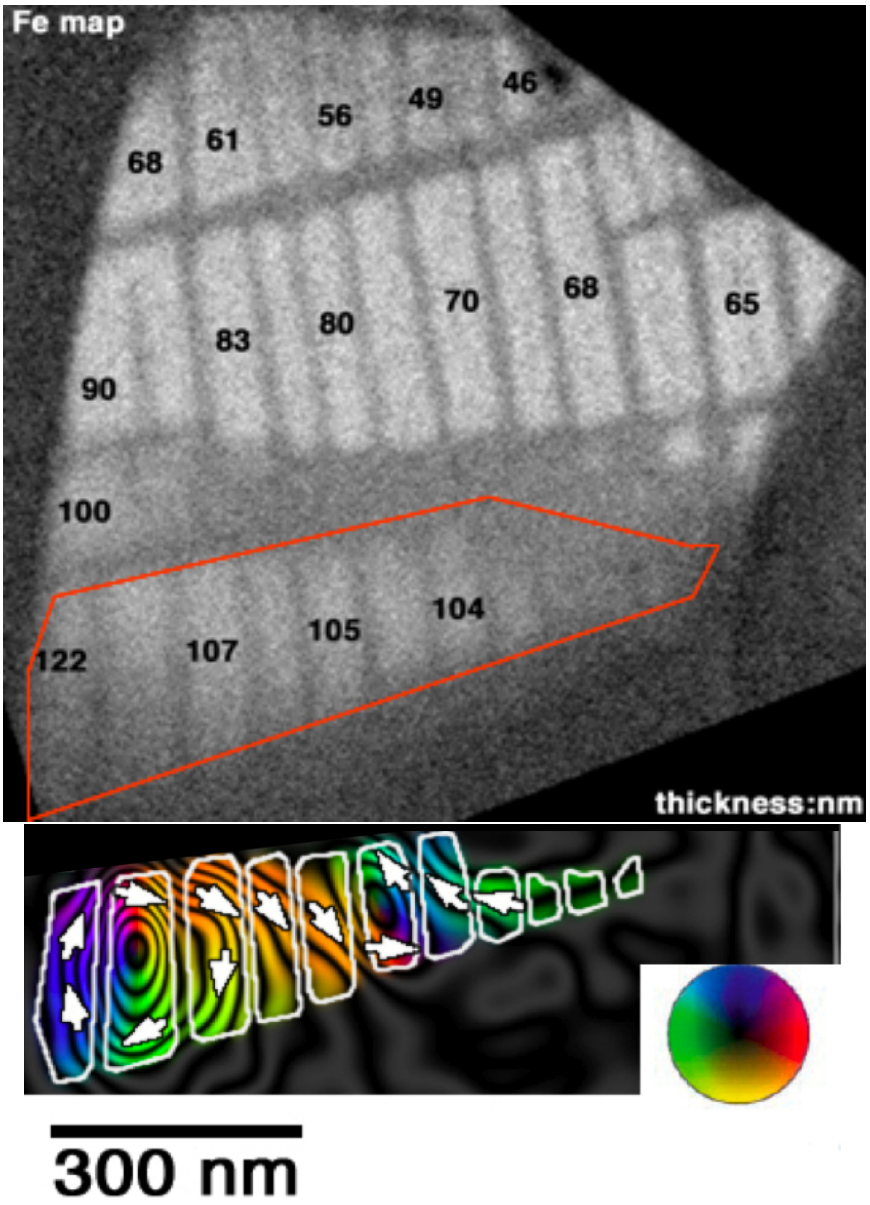

Figure 4.7: The raw data used to generate the 3D structure used within the model taken from Feinberg et al. (2005) and Feinberg et al. (2006). The top image shows the Fe map of the structure, the lighter sections indicating higher Fe concentrations, the area used within the models being outlined in red. The bottom image is the holographic TEM image with the boundaries marked. On the Fe concentration map the black numbers on the individual lamellae correspond to the approximate thicknesses of the magnetite lamellae in nm.

observed in Evans et al. (2006) that lamella separation in assemblies of interacting grains will effect the overall structure of the system. Figure 4.9 shows the two different lamellae separation distances tested, one with approximately 10 nm separation, Figure 4.9 image b), and the other approximately 20 nm, Figure 4.9 image c). The constants used for magnetite can be seen in Table 4.1, and the applied magnetic field direction is orientated with respect to the xy plane of the sample as can be seen in Figure 4.8.

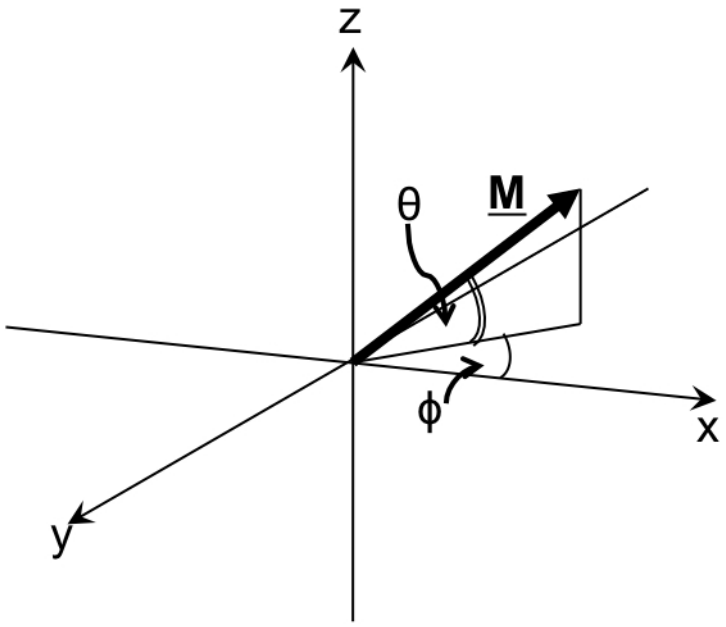

Figure 4.8: Orientation of the magnetic field where θ is 30° and is a consequence of the orientation of the sample during the off-axis electron holography process. ϕ is 20°

The results of these two separation distances seen in Figure 4.9 show that Figure 4.9 image b) with the reduced separation has a magnetic structure that is much closer to the direct observations shown in Figure 4.9 image a). All the models of this system shown in Chapters 5 and 6 use this separation distance.

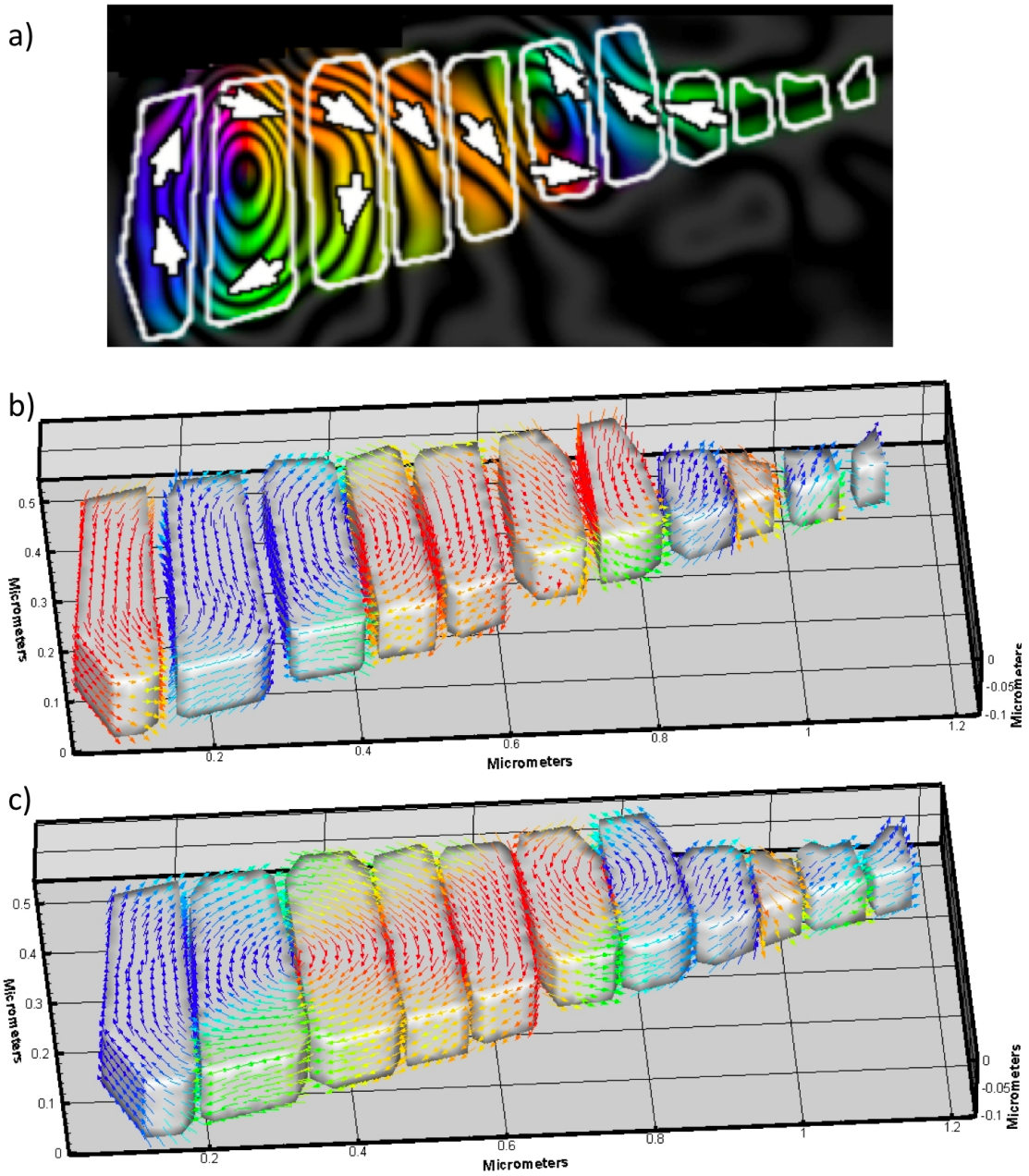

Figure 4.9: Two models showing the differences observed when altering the lamellae separation within the system. Image a) has an average separation of 20 nm whereas image c) uses a separation of approximately 10 nm. Image a) shows the direct observations. It can be observed the magnetic structure in image c) is more similar to the direct observations than that of image b)

4.3.2 Effect of varying the lamellae thickness

The thickness of the sample was varied to try to find the thickness that produced a modelled micromagnetic solution closest to that observed experimentally. Although the physical thickness of the sample is given in Figure 4.7 as ranging between 120-90 nm from left to right it is likely that not all of this thickness contributes to the overall magnetic structure being observed. Therefore to model this system the thickness of the geometry would have to be altered accordingly. Due to this uncertainty three different thickness criteria, 120-90 nm, 90-60 nm and 60-90 nm were modelled and the results can be seen in Figure 4.10.

The Figure 4.10 image a) run with the smallest thickness shows a homogeneous SD structure, quite unlike the structures seen in the direct observations and therefore this thickness criteria can be dismissed. The differences between Figure 4.10 image b) and Figure 4.9 image c) are far more subtle. However, it can be seen that the thicker of the two models in Figure 4.10 image c) has more magnetic structure within the z component of the sample. The direct observations can show us only the in-plane magnetic field of any sample. However, as this is essentially a thin film, we would expect that the magnetisation would lie primarily within the xy plane of the film. Ultimately the 90-60 nm thickness criterion was selected and, as with the lamellae separation, is used in all the following models of this sample.

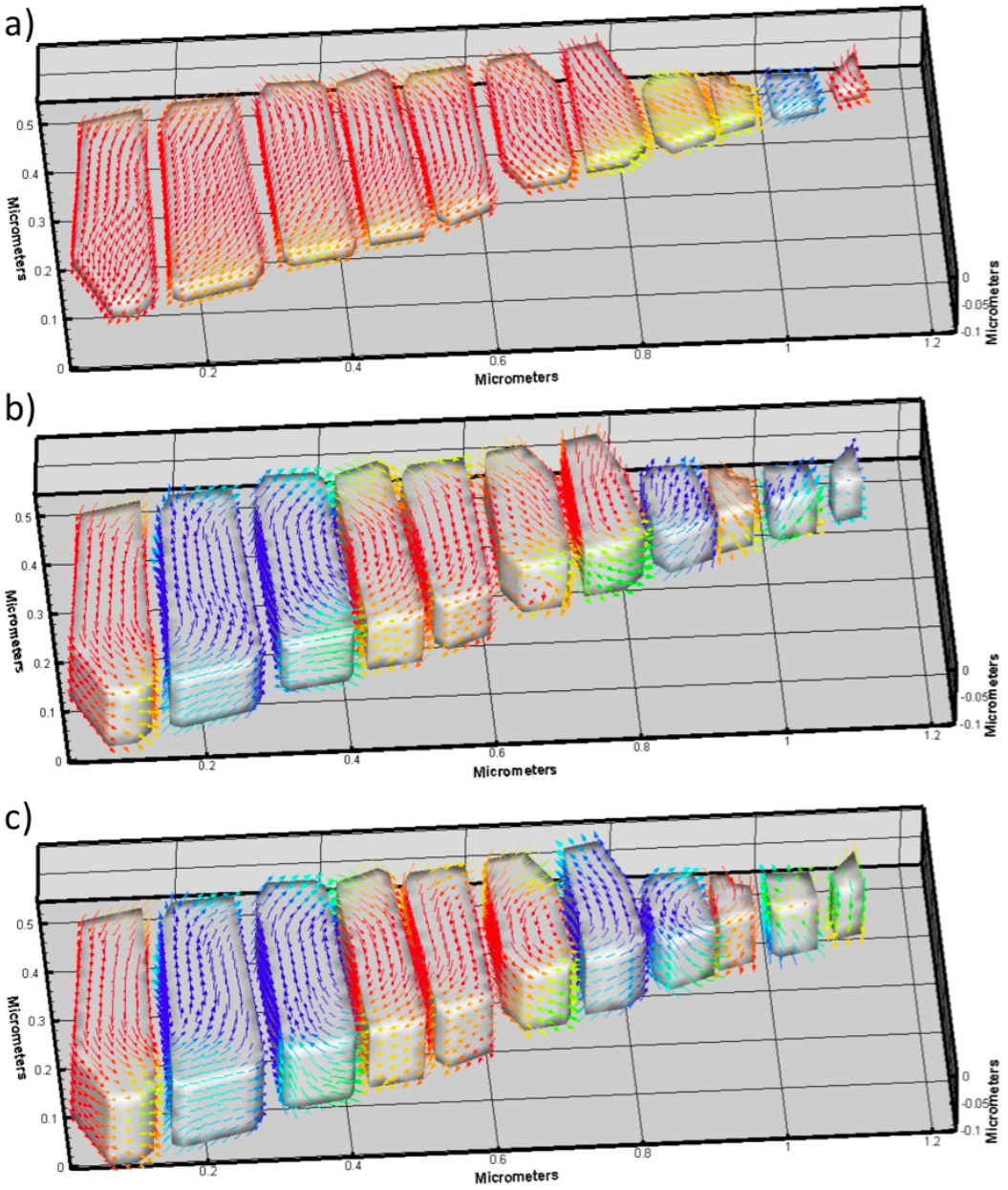

Figure 4.10: Three models showing the differences observed when altering the thickness of the geometry. Image a) has an average thickness of 60 nm, image b) 90m and image c) 120 nm. Image a) has a predominantly SD structure. Images b) and c) are very similar however image c) has more of the magnetisation directed out of the plane.

Chapter 5

Physical Bridging

5.1 Introduction

As has been observed within Chapter 4, Figures 4.10 and 4.9, all the micromagnetic models, regardless of lamellae separation or depth, show the vortex centres situated on the boundary of the magnetite lamellae. In the case of the direct observations the vortex centres are seen to situate themselves within the middle of the body of the lamellae, that is well away from the grain edge (Figure 5.1). This is a surprising observation, as it would be expected to see the vortices nucleating at grain edges where the exchange energy is minimised.

This chapter explores some of the possible variability within the geometrical and chemical structure of the system which could account for those discrepancies observed between the direct observations and micromagnetic modelling results.

Detailed in this chapter is the investigation of the effect on the modelled magnetic structure if a thin bridge of magnetite exists between the distinct magnetite lamellae within the sample. This bridge, to be unresolved by the off-axis electron holography, would have to lie at the base of the sample between the intergrowths and have a depth of no more than 10 nm (Figure 5.2). Although unlikely, due to the mechanism by which exsolution takes place (see section 2.6), this hypothesis allows the examination of the effect of increasing the interaction between the

magnetite lamellae on the magnetic structure. In addition to bridging between the lamellae the topography of the bridges was also altered to examine the effect of this on the system (Figure 5.7).

Throughout all these examples the values of the material parameters used for these simulations are as shown in Table 4.1 and are the values for magnetite at 300 K. In addition the initial field direction used in the numerical models is identical to that of the experimental observations and is shown in Figure 4.8.

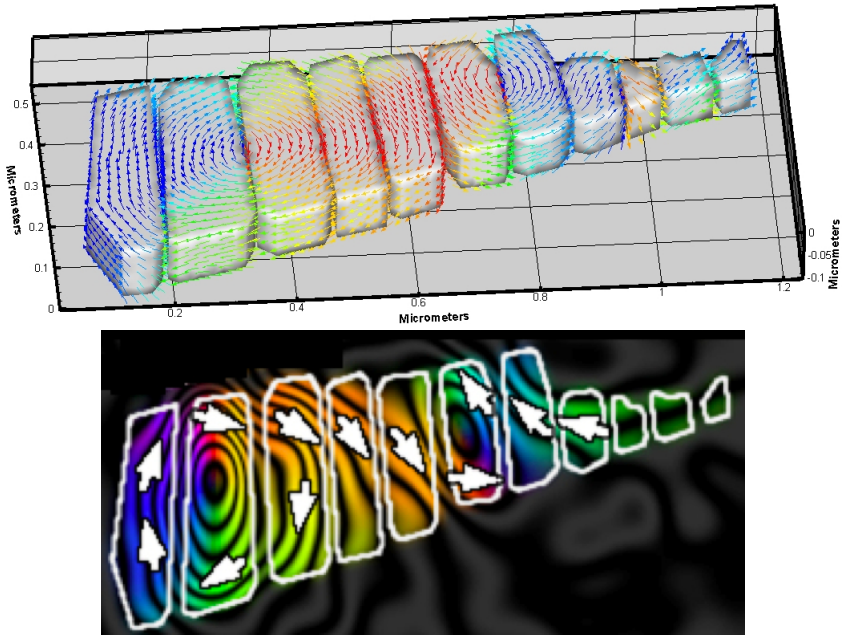

Figure 5.1: Image showing the model results of the irregular geometry, above, and the direct observation by off-axis electron holography, below

5.2 Thin magnetite bridge

To investigate the hypothesis that magnetite lamellae are bridged by additional magnetite, a suite of models have been generated where the individual magnetite lamellae are connected via a thin bridge of magnetite ranging in depth from 5-15 nm (Figure 5.2). This simulation uses the previous irregular geometry seen in section 4.2 but has the addition of a geometry between the adjacent lamellae, as

shown in Figure 5.2.

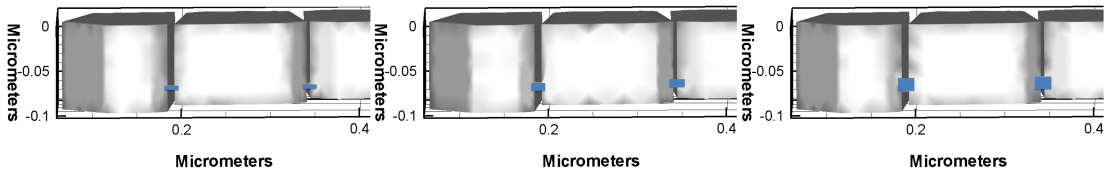

Figure 5.2: Image of the physical bridge between the lamellae, in this case taking depths of 5, 10 and 15 nm. The bridging runs near the base of the image and is highlighted in blue.

The following diagrams are the results from the simulations with the altered bridge depths. The bridge depths chosen give a range of bridge geometries that pass through the cut-off depth of 10 nm. This can be resolved by the off-axis transmission electron holography, therefore, although those bridges under 10 nm may be present but would not be resolvable experimentally. The initial magnetic field direction is the same as seen in Figure 4.8 for all the models.

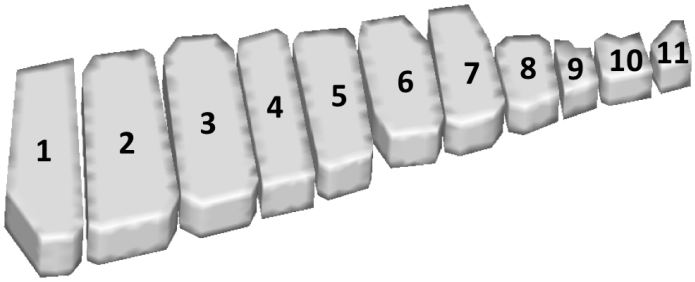

Figure 5.3: Individual lamellae within the system will be referenced using this numbering criteria counting from left to right. This will be used within Chapter 6 also.

Throughout the discussion of all the models of this particular sample the individual lamellae are given numbers, the numbering criteria for this shown in Figure 5.3. This numbering convention is also used in Chapter 6.

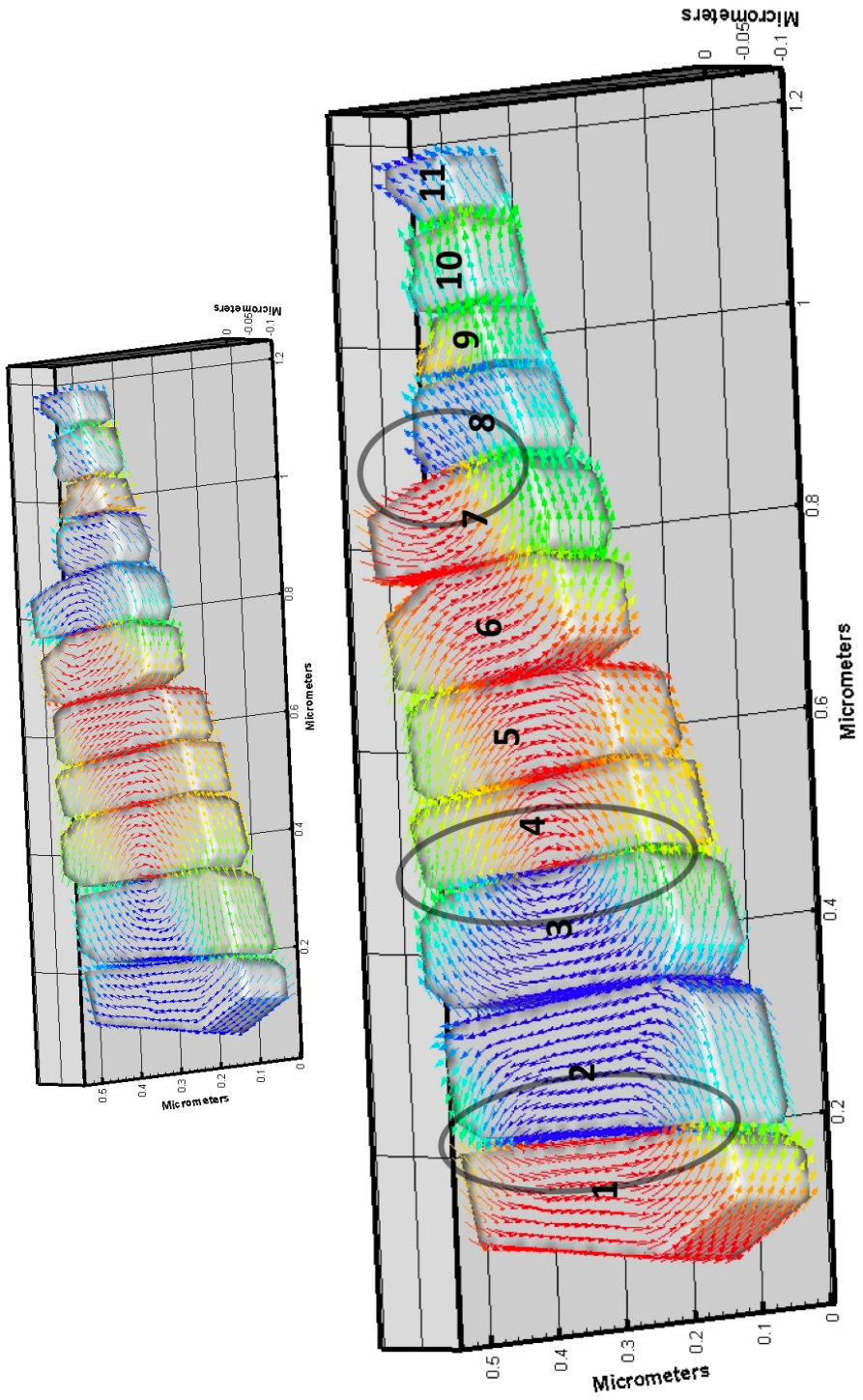

Figure 5.4: The top image is the non-bridged model. The bottom image is a simulation with a thin magnetite bridge of approximately 5 nm lying at the base of the system. All the material properties are consistent with the original. Lamella 1 has a magnetisation direction opposite to that of the non-bridged model. Vortices have been circled and can be observed nucleating at the adjacent boundaries of lamellae 1 and 2 and lamellae 3 and 4. The vortex seen in the top non-bridged model between lamellae 6 and 7 is absent, however, as indicated, a partial vortex is seen between lamellae 7 and 8.

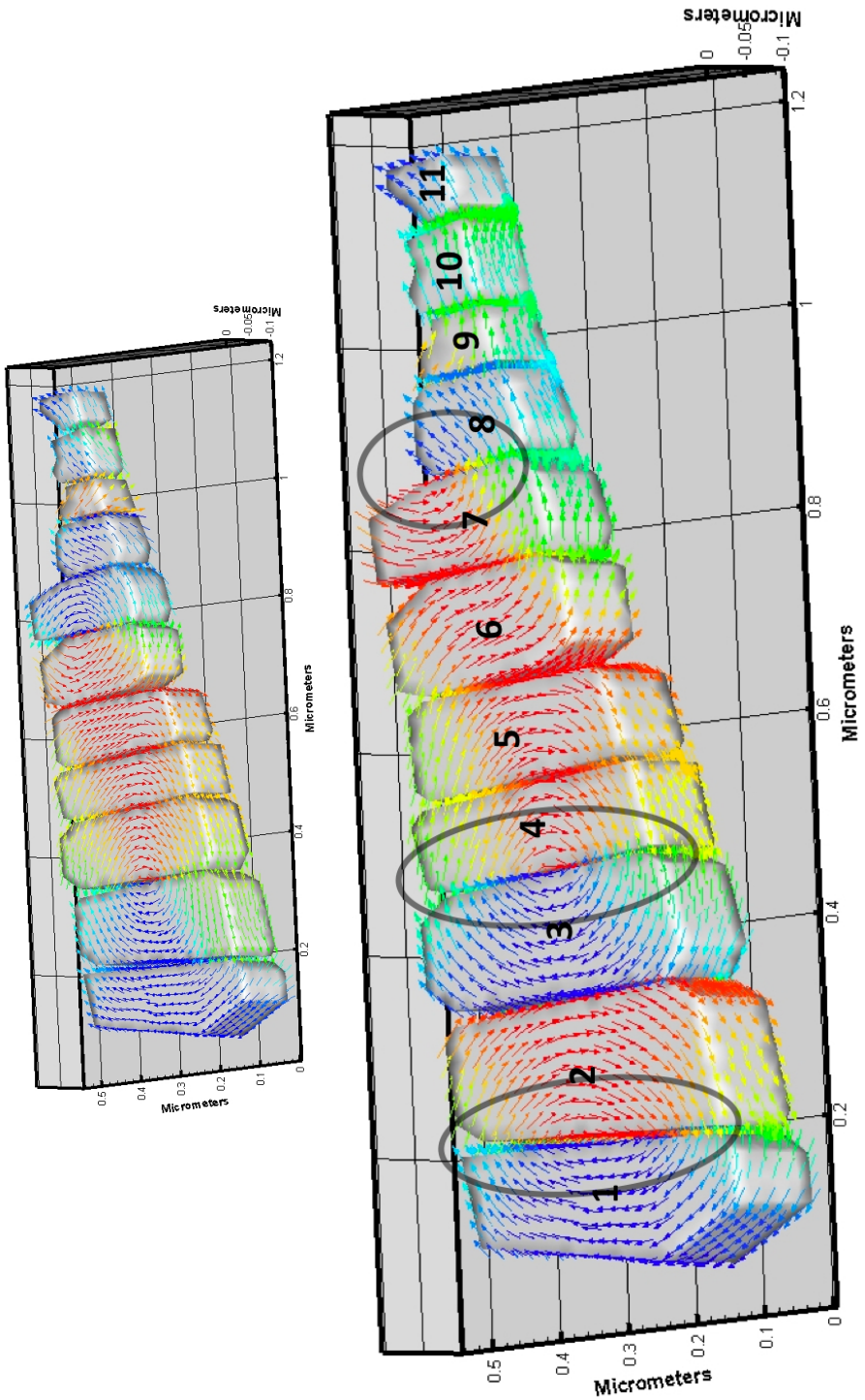

Figure 5.5: The top image is the non-bridged model. The bottom image is a simulation with a thin magnetite bridge of approximately 10 nm lying at the base of the system. All the material properties are consistent with the original. Vortices have been circled and can be observed nucleating at the adjacent boundaries of lamellae 1 and 2 and lamellae 3 and 4. The vortex seen in the top non-bridged model between lamellae 6 and 7 is absent, however, as indicated, a partial vortex is seen between lamellae 7 and 8.

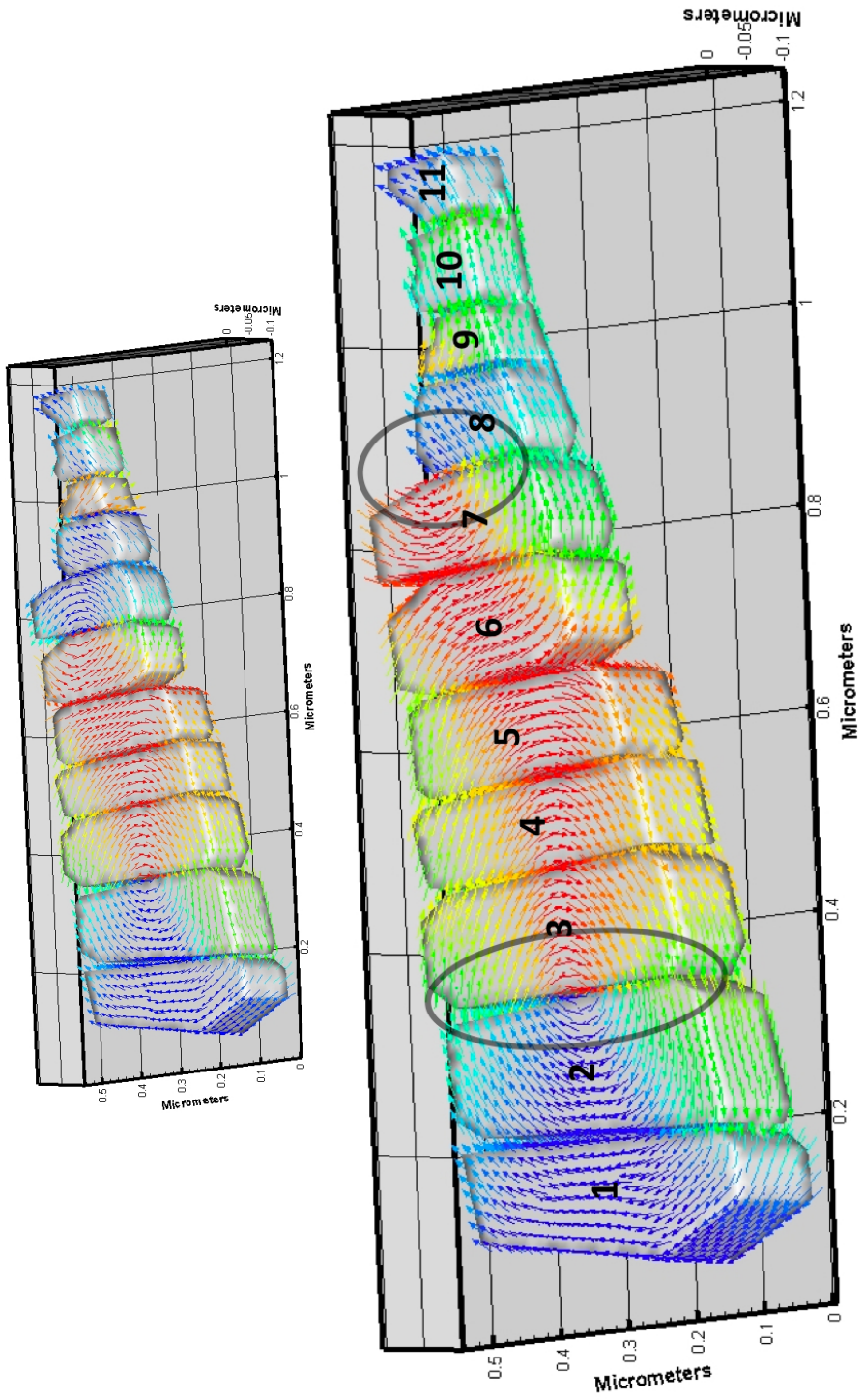

Figure 5.6: The top image is the non-bridged model. The bottom image is a simulation with a thin magnetite bridge of approximately 15 nm lying at the base of the system. All the material properties are consistent with the original. This model is a close match to the non-bridged model, where a vortex can be seen nucleating at the adjacent boundaries of lamellae 2 and 3. The vortex seen in the top non-bridged model between lamellae 6 and 7 is absent, however, as indicated, a partial vortex is observed between lamellae 7 and 8.

The thickest bridge model, Figure 5.6, looks very similar, but is not identical to the results for the full model with no bridging; however, the results for the 5 nm and 10 nm bridging examples are quite different. In observing the 5 nm bridge model it is evident that there is an increase in the total number of vortex structures in the sample. It is however important to note that in all these cases the vortex centres are still situated at the boundaries between the lamellae and not within the lamellae themselves. In this first case these vortex structures are between the first and second, third and fourth, then seventh and eighth lamellae when counting from the left. Interestingly it is seen here that the first lamella has the magnetisation direction in the opposite direction to the non-bridged model. The 10 nm bridging model, again, does not resemble the non-bridged model as much as the 15 nm bridge case. In this case also more vortex structures can be seen with the vortex centres being positioned at the lamellae boundaries.

In all these solutions the fourth to the seventh lamellae have the same structure and remain the same as the non-bridged case, with the smallest four lamellae also remaining unchanged regardless of the bridge dimensions, although they do differ significantly from the non-bridged model. Although the smallest lamellae display a single domain (SD) structure in the non-bridged model, their magnetic orientations differ from one another whereas in all the bridge models they align with each other. The latter structure is in close agreement with the direct observations of the system, although the magnetisation is consistently in the opposite direction to that seen in the direct observations.

5.3 Altered thin magnetite bridge

A further development within this study was to alter the shape of the bridges themselves in order to examine the effect this would have on the magnetic domain structure nucleated in the system. The bridge geometries were altered by removing wedge-like sections from the free ends of the bridge resulting in a volume reduction of it. The following diagrams show the degree of alteration used to

create these altered geometries (Figure 5.7). The c factor is a measurement of the distance cut into the bridge from the original free edge of the bridge to the apex of the removed triangular wedge. The c values used were 60nm, 80nm, 90nm and 100nm, where this distance was cut from both sides of the bridge. For those lamellae where the overall length was less than 200 nm (lamellae five, six and seven) the c factor used was that of the largest c which would still result in there being bridging of some form between the adjacent lamellae. It was also attempted to produce a similar alteration effect but with a more curved geometry. This ultimately did not work because it required too fine a mesh size to adapt to the small scale curvature within the system. Instead the volume removed each time was triangular in shape which was more appropriate when using a tetrahedral meshing scheme.

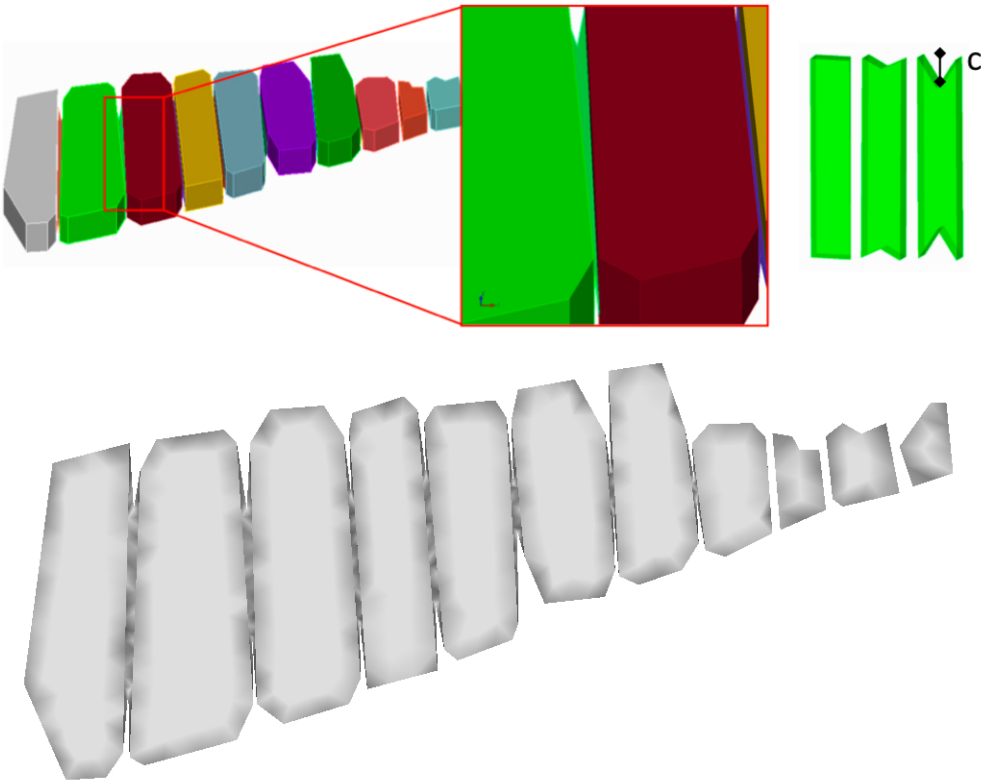

Figure 5.7: This is a simple diagram representing the geometry of the altered bridge structures used in section 5.3, with c marked on the altered geometry. The bottom image shows a plan view of a fully bridged structure.

Figures 5.8 to 5.11 show a series of models where the bridge topography was altered using various different c values. For ease of comparison the top image in each figure is the model of the non-bridged structure.

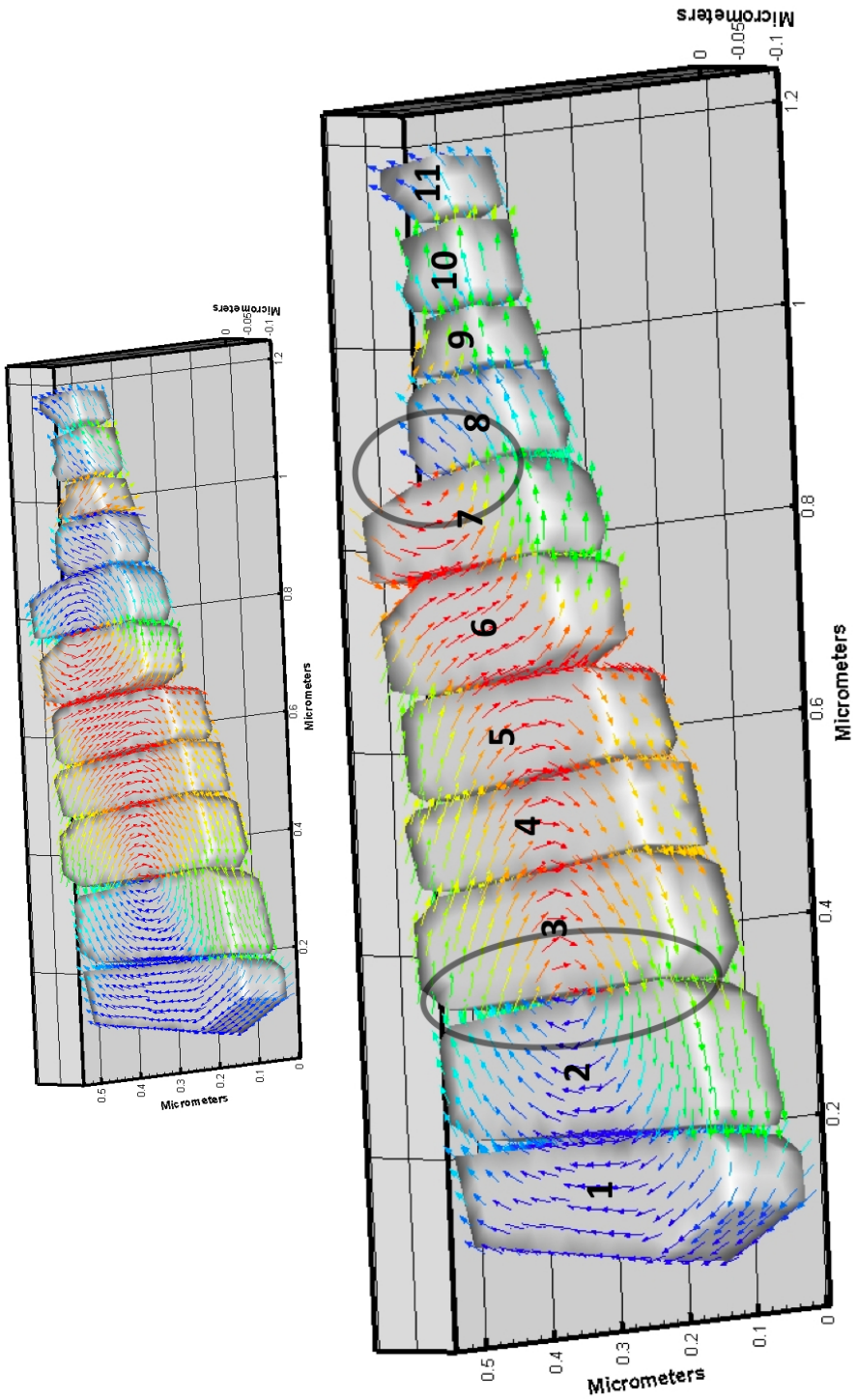

Figure 5.8: The top image is the non-bridged model. The bottom image is the result from the model using a cutting factor of 60nm. All the material properties are consistent with the original. This model is almost identical to Figure 5.6 where a vortex is observed on the boundary between lamellae 2 and 3 as seen in the non-bridged case and a partial vortex structure is seen on the boundary between lamellae 7 and 8.

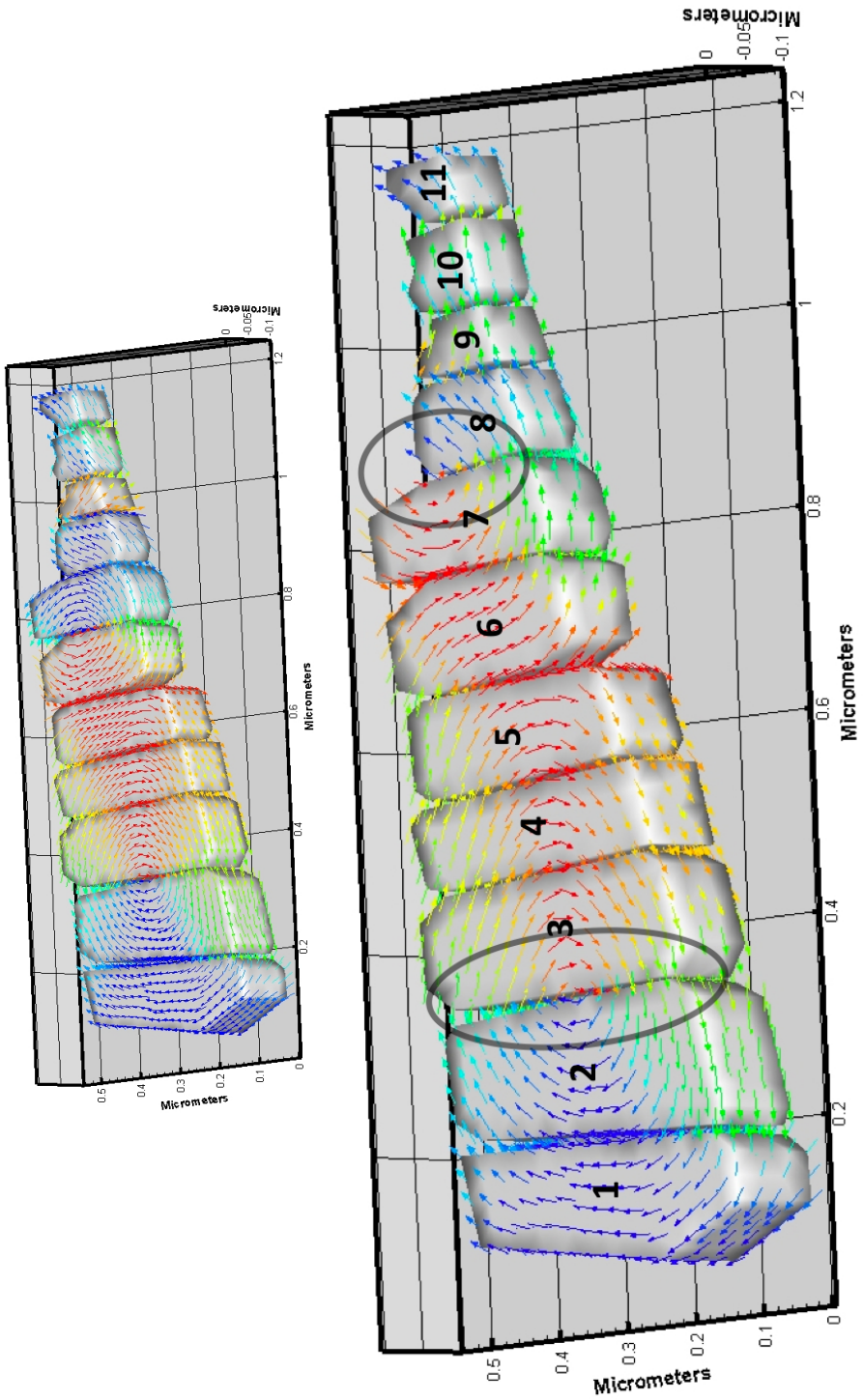

Figure 5.9: The top image is the non-bridged model. The bottom image is the result from the model using a cutting factor of 80nm. All the material properties are consistent with the original. This model remains unchanged from Figure 5.8 with the 60nm cutting factor, where a vortex is present between lamellae 2 and 3 and a partial vortex can be seen between lamellae 7 and 8.

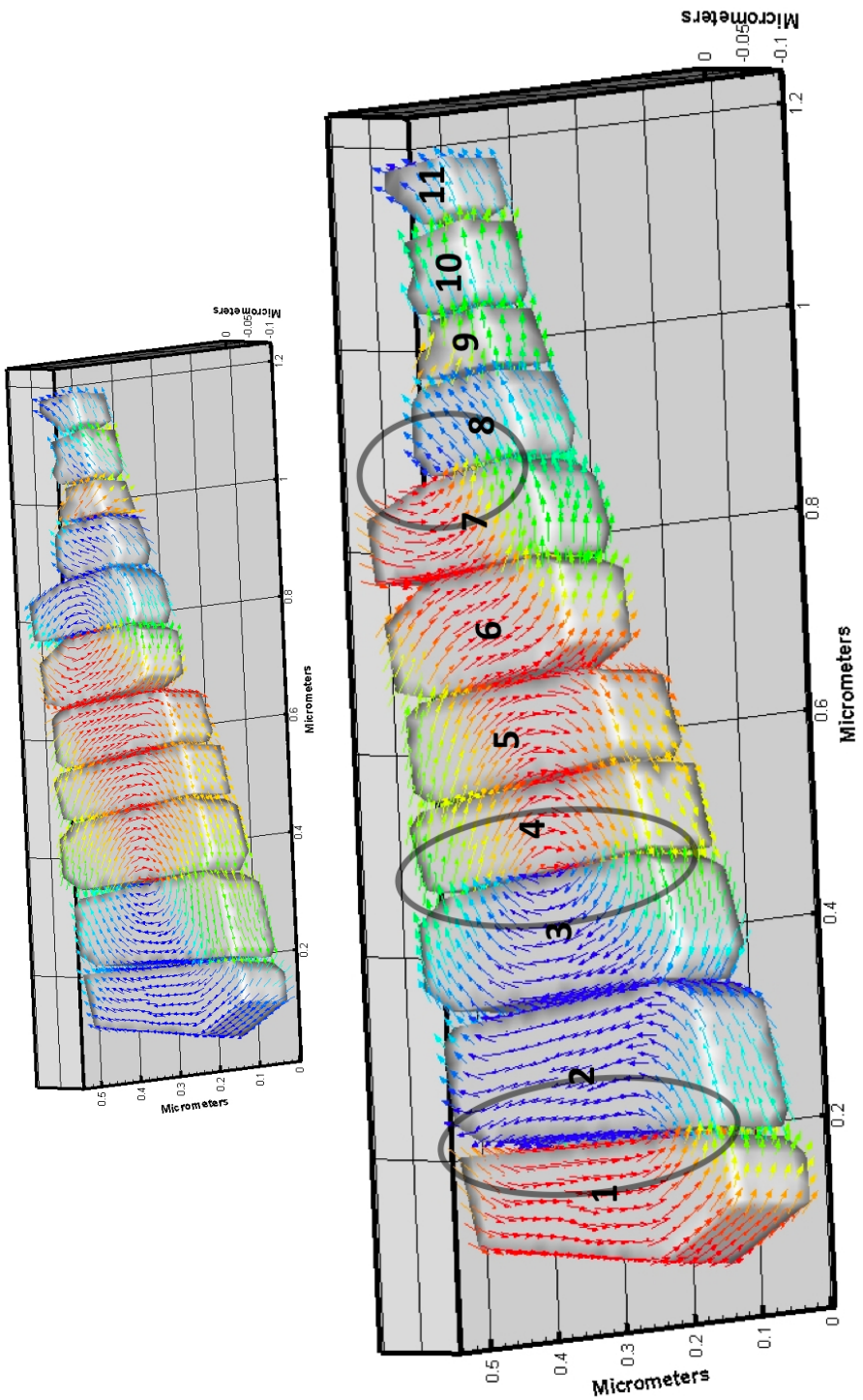

Figure 5.10: The top image is the non-bridged model. The bottom image is the result from the model using a cutting factor of 90nm. All the material properties are consistent with the original. This model differs significantly from the previous models in Figures 5.8 and 5.9. Two vortex structures are observed between lamellae 1 and 2 and between lamellae 3 and 4. The partial vortex structure between lamellae 7 and 8 is however still present in this model. With the additional vortex and the magnetisation of the 1^{st} lamella in the opposite direction to that of the non-bridged model, this structure is very similar to that seen in Figure 5.4 with an unaltered bridge of 5 nm.

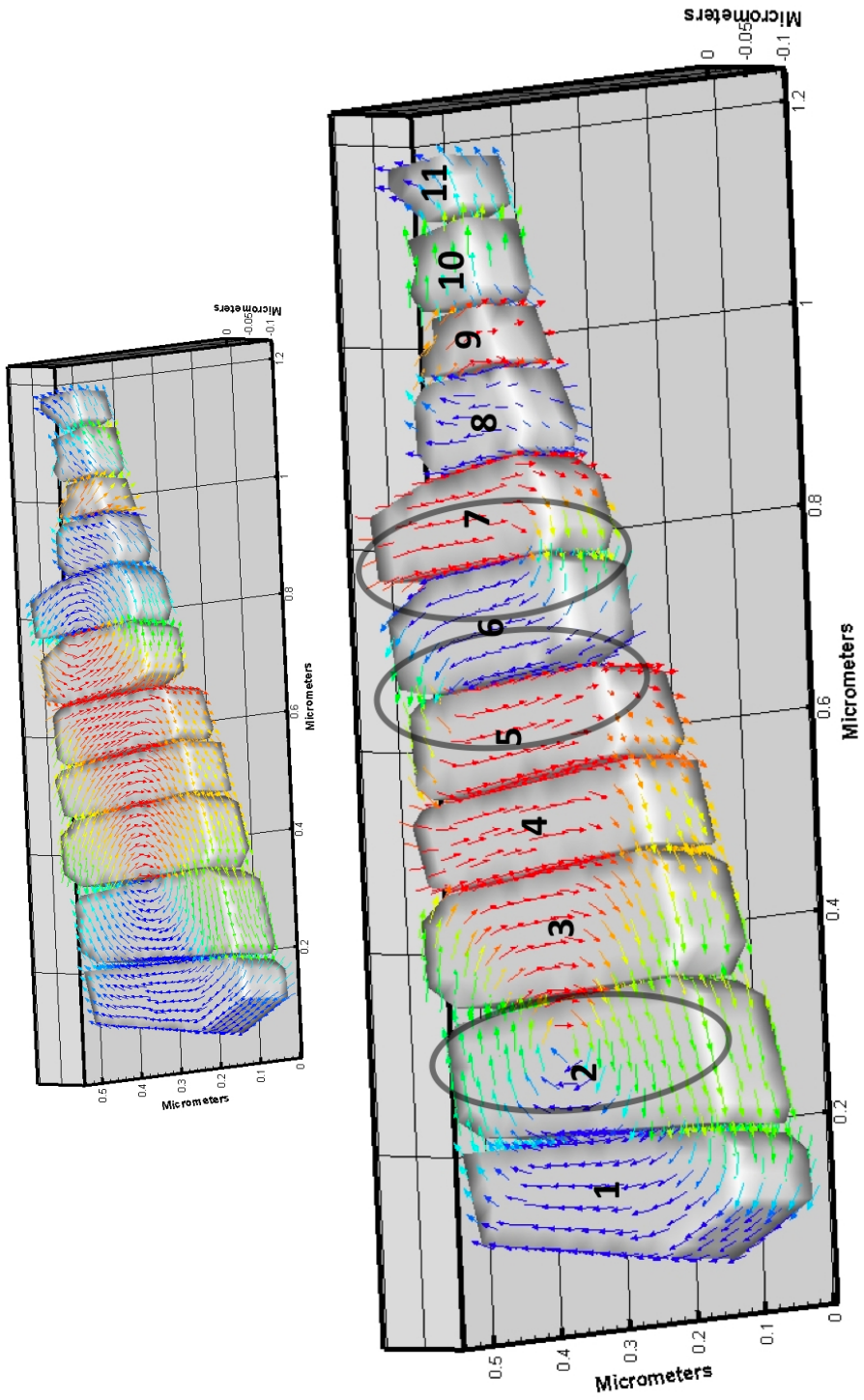

Figure 5.11: The top image is the non-bridged model. The bottom image is the result from the model using a cutting factor of 100 nm. All the material properties are consistent with the original. This model differs from all the other results in this chapter as a vortex, although close to the edge, can be seen within lamella 2 as evident within the direct observations. However, although a vortex-like structure is observed between lamellae 6 and 7, there is a similar vortex-like structure between lamellae 5 and 6. The magnetisation direction of lamellae 6 and 7 in this model is in the opposite direction to that observed in the non-bridged model.

The modified bridge geometries also show some interesting results.The first of the altered bridges in Figure 5.8 does not differ significantly from the non-bridged case, although, once again, the smaller blocky lamellae (lamellae eight, nine, ten and eleven) are more homogeneous and aligned with each other. This has been consistent within all the samples involving no altered topography. The following two models, Figure 5.9 and Figure 5.10, both have the first lamella with a magnetic direction in the opposite direction to the non-bridged model and Figure 5.9 looks to be nearly identical to Figure 5.4. Figure 5.10, although again with the first lamella with the magnetisation in the opposite direction, also has the fourth to the seventh lamellae displaying a different magnetic structure for the first time in these simulations. This also appears to affect the smallest lamellae which now resemble the non-bridged model.

It is the final simulation which is of most interest, since it can be seen that in the largest of the lamellae (lamellae numbers two and three), the vortex location is slightly displaced. The displacement of the vortex is more similar to that of the experimental observations of this sample, where the placement of the vortex is found within the interior of the lamellae as opposed to positioned on the boundary between lamellae. Interestingly, this model also shares similar features with the model in Figure 5.10 on the left hand side of the sample. This vortex positioning development is interesting, as it indicates that the position of the vortex within the system can be controlled by the level of interaction existing between the lamellae. The following models are an extension of this bridging idea to examine the effect of having far larger bridging structures and therefore more direct interaction between the lamellae.

5.4 Increased thickness bridging

This section examines the effect of adding a far thicker magnetite bridge between the adjacent lamellae (Figure 5.12). Although unrealistic, as a bridge with those depths would definitely be resolvable using electron holography, this was a way to

examine the effect of increasing the exchange interaction between lamellae, which might encourage nucleation of the vortices away from the grain edges.

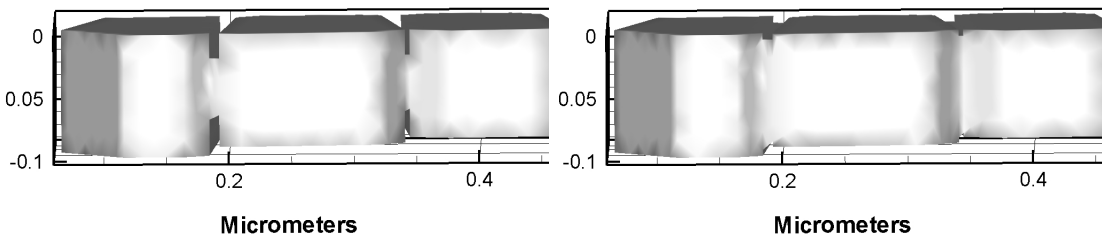

Figure 5.12: Example of the bridging in the case where the depth between the lamellae is altered and where the bridge runs along the centre point of the system. All the material properties are consistent with the original.

Those models were run with only the largest lamellae within the system. Also, although various depth models were run, only two have been included, a depth of 50nm and a depth of 90 nm, because the differences between the 50-80 nm models were negligible. It can be observed that the 50 nm model resembles the model with no bridging and also the model with a 15 nm bridge lying at the base of the system seen in Figure 5.6. However, if we compare the two images in Figure 5.13, we see that the vortex centre has moved towards the centre of the second lamella. This result is very similar to the results observed for the altered bridge topography seen in Figure 5.11.

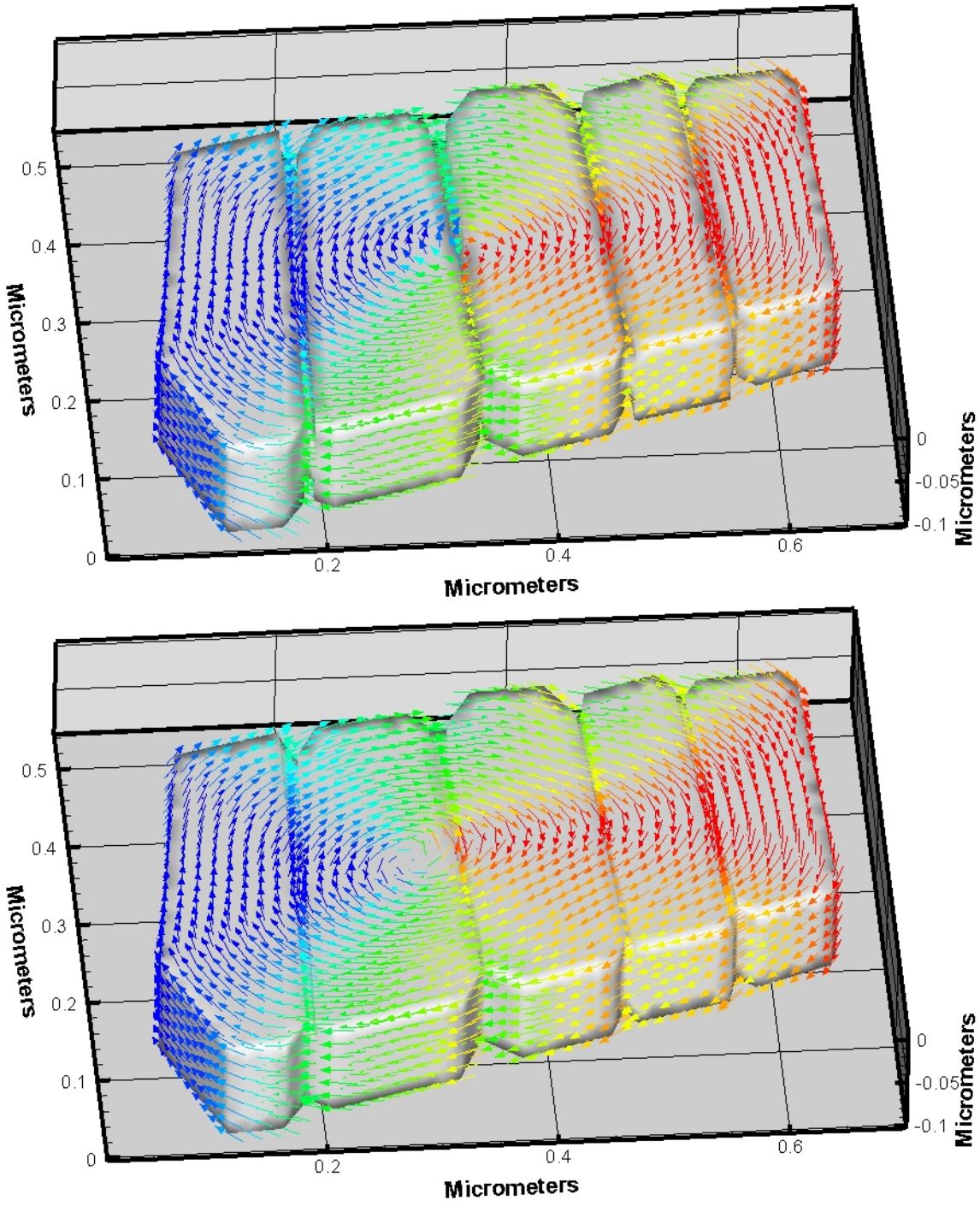

Figure 5.13: Two images showing the modelled magnetic structure from the geometry style shown in figure 5.12. This image shows a bridge with dimensions of 50 nm (top) and 80 nm (bottom). Only the lamellae 1 to 5 were modelled in this study. As can be observed, the overall structure of both systems is very similar. However, the 80 nm bridged model shows a slight movement of the vortex structure from the boundary of lamellae 2 and 3 into the body of lamellae 2. The positioning of the vortex is similar to that seen in Figure 5.11 with the cutting factor of 100 nm.

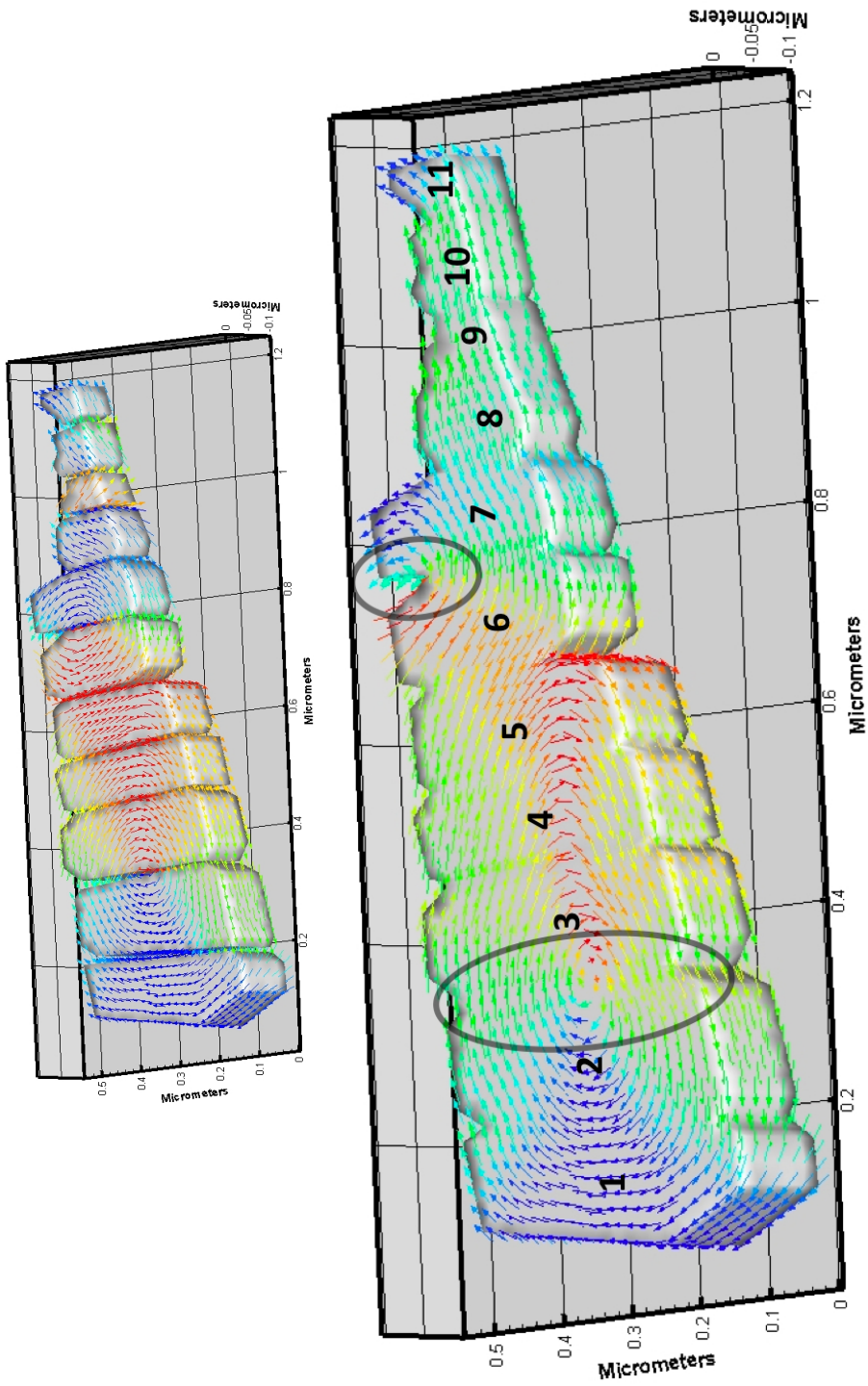

Figure 5.14: Image of a full magnetite structure. This model retains some of the main features observed in the non-bridged structure. In particular the vortex on the boundary of lamellae 2 and 3 is still present. The full vortex observed in the non-bridged model between lamellae 6 and 7 is absent although there is a partial vortex structure between these lamellae at the topmost edges of the structures.

The final model, Figure 5.14, is the result obtained when the entire system is assumed to be magnetite and therefore the entire structure is a continuous magnetic block. Although obviously not realistic it is interesting to examine the effect this has. It can be seen from the result in Figure 5.14 that the location of the vortex centre is still centred in the region between the magnetite lamellae, that is at the point where the grain edges exist in the non-bridged version. It can also be observed that the location of the second vortex seen in the non-bridged version is no longer a full vortex structure and that region looks far more homogeneous. The smallest lamellae again have a magnetisation in the opposite direction to that of the direct observations and are also homogenous. Although this situation with the thick bridging is unrealistic, as discussed in section 2.6 the exsolution process would not lend itself to producing structures as those seen in Figure

It is likely that there is also a shape dependency, which would also help to explain the consistency of the vortex centre's positioning even in the absence of the physical grain edges. This could be a consequence of some of the geometrical features still evident in the entirely bridged structure, particularly the sharp corners between the neighbouring lamellae, as this can be seen particularly clearly between lamellae five and six and lamellae six and seven.

5.5 Conclusion

Taking into account all the models it can be observed that changing the physical bridging between the neighbouring lamellae does not change the position of the vortices on the system in relation to the grain boundaries. However, by changing the thickness/topographies of the magnetite bridges, it is possible to control the grain edges at which the vortex states nucleate and also the number of vortex states seen within the system. This is identical to the results shown in Chapter 4, where alteration of the lamellae depth and lamellae separation again only affect the grain edges at which the vortex states nucleate.

These models show that, in the absence of any inaccuracies with the direct observations, there is likely to be some interaction existing between the magnetite lamellae other than that which can currently be accounted for using the single phase micromagnetic code. This result leads to an examination of this system using the multiphase micromagnetic code. This allows the regions between the lamellae to exhibit magnetic properties distinct to that of the surrounding regions. It cannot, however, be discounted that the discrepancies observed between direct observations and model results are not a consequence of the micromagnetic code but with the off-axis electron holography results.

Chapter 6

Exchange Bridging

6.1 Introduction

This chapter explores some systems, both theoretical and experimental, using the multiphase model described in Chapter 3. In the case of the irregular exsolution texture, examined in Chapters 4 and 5 the multiphase model gives one the ability to add a different level of interaction within the ulvöspinel phase of the system which is omitted within all the previous models. In particular the exchange energy has been altered within the ulvöspinel phase and the effects examined.

In addition to the irregular exsolution structure a variety of models, using simple geometries, have been run involving two magnetic phases in contact with each other. The systems modelled in this chapter are magnetite-maghemite and magnetite-titanomagnetite where the titanomagnetite phase is assumed to be that of TM60. This titanomagnetite has a composition of 60% of ulvöspinel in the magnetite and ulvöspinel solid solution. Due to the lack of information regarding the exchange constant (A_{ex}) of both maghemite and TM60 section 6.2 discusses the method by which A_{ex} was assigned.

6.2 Exchange Assumptions

The exchange constant is unknown for TM60 and maghemite, and therefore estimations of this value have had to be made when trying to simulate multiphase structures containing them. For these estimations the critical domain size of both maghemtite and titanomagnetite was used. The critical single domain (SD) size gives the maximum dimensions at which one would expect to observe a SD structure in a material and therefore indicates the boundary between SD and pseudo-single domain (PSD) behaviour in the material. It is, however, difficult to ascertain the exact point at which this transition happens, particularly as grain shape will play a part in determining when this transition occurs with elongate grains typically sustaining SD structures to larger dimensions than equidimensional grains [Dunlop and Ozdemir (1997)].

The SD to PSD transitions used within this chapter for both maghemite and TM60 are based on theoretical estimates for the SD critical domain size at room temperature from the work of Morrish and Yu [Morrish and Yu (1955)] and Butler and Banerjee [Butler and Banerjee (1975)] respectively. Also included are the experimental estimates by Soffel for TM60 [Soffel (1971)]. Using all these results the critical domain size in maghemite is assumed to be $0.06\mu m$ and $0.2\mu m$ for TM60, where the value for TM60 is the average when considering both the theoretical and experimental results mentioned previously. The values for the first order magnetocrystalline anisotropy (K_1) and the saturation magnetisation (M_s) are known.

To constrain the exchange value for TM60 a range of cubes of dimensions 0.18 μm, 0.2 μm and 0.22 μm were modelled a number of times with various values of A_{ex}, the values for the other constants being kept consistent. The values of Aex used are all multiples of magnetite as the value of magnetite was used as a starting point to ascertain a value of A_{ex} in the TM60. Similarly, for maghemite, a set of cubes of dimensions 0.05 μm, 0.06 μm and 0.07 μm were modelled as this spans the theoretical critical SD size for this material. For both cases the value

of A_{ex}, giving the critical SD transition at approximately the correct dimensions, was found to be $0.4 \times A_{ex}$ of magnetite.

The results for these models can be seen in Figure 6.1 and Figure 6.2. In both cases we observe a shift from a flowered magnetic structure to a vortex structure at the critical SD size. A flowered magnetic structure is essentially a SD magnetic structure where the magnetic structure is not completely homogeneous but instead has some directional change of the magnetisation at the edges of the system. In the case of the maghemite system shown in Figure 6.1 there is also evident a relocation of the centre of the vortex system from the corner of the cube in Figure 6.1 b) to the cube face in Figure 6.1 c) as the dimensions are increased. This is the first time that an estimation of these values has been undertaken in this fashion.

The values for the saturation magnetisation M_s and magnetocrystalline anisotropy constant K_1 for maghemite and TM60 are displayed in the tables below (Tables 6.1 and 6.2 respectively) and are from Dunlop and Özdemir [Dunlop and Ozdemir (1997)]. These values are used for all the subsequent models within this chapter that use these materials.

The modelled hysteresis plots for the SD and PSD cases used to constrain the systems are shown in Figure 6.3 for maghemite and Figure 6.4 for TM60 respectively. It can be observed in Figure 6.3 image a) that the maghemite cube with dimensions of 0.05 μm has a coercivity of 9 mT and in Figure 6.3 b) that the larger $0.07\mu m$ cube has a coercivity of 4 mT. For the TM60 system a coercivity of 10 mT for the $0.18\mu m$ cube is observed in Figure 6.4 image a) and a coercivity of 5 mT for the cube with dimensions of $0.22\mu m$ is shown in Figure 6.4 image b). As expected, for both maghemite and TM60 a decrease in the coercivity is observed with an increased grain size.

Table 6.1: Values used for Maghemite [Dunlop and Ozdemir (1997)]

Constant	Value
Anisotropy (K_1)	$-4.65 \times 10^3 J/m^3$
Exchange (A_{ex})	$5.36 \times 10^{-12} J/m$
Saturation magnetisation (M_s)	380 kA/m

Table 6.2: Values used for Titanomagnetite [Dunlop and Ozdemir (1997)]

Constant	Value
Anisotropy (K_1)	$2.02 \times 10^3 J/m^3$
Exchange (A_{ex})	$5.36 \times 10^{-12} J/m$
Saturation magnetisation (M_s)	125 kA/m

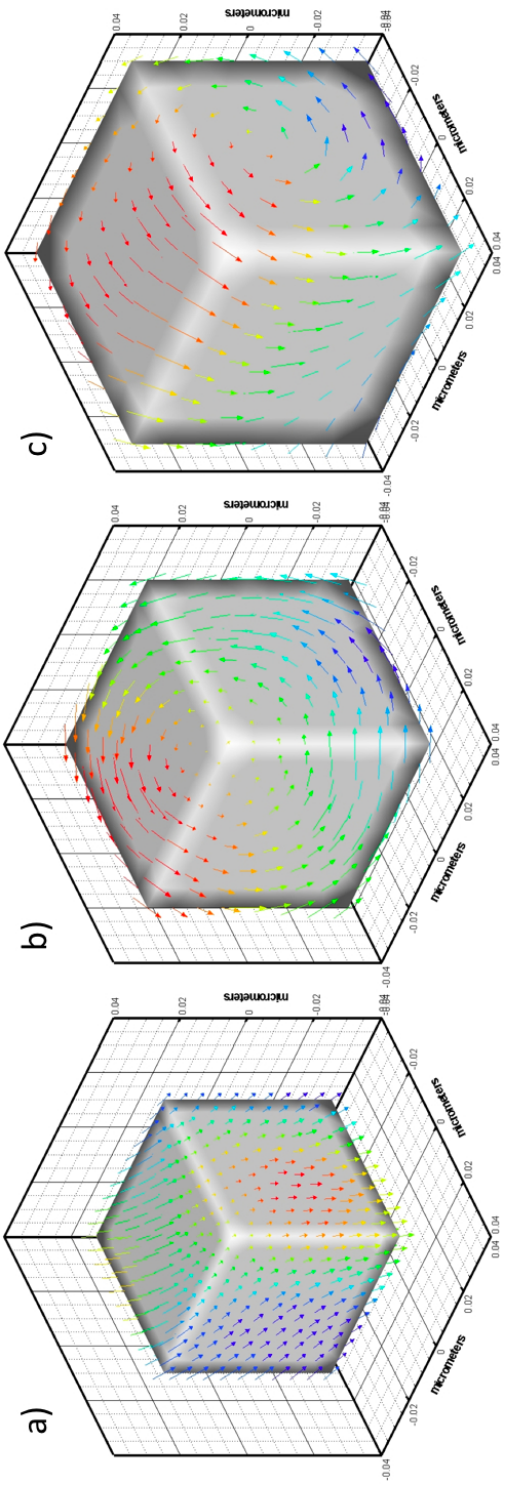

Figure 6.1: Models of cubes with dimensions ranging through the critical SD dimension for maghemite where the dimensions are $0.05\mu m$ in image a), $0.06\mu m$ in image b) and $0.07\mu m$ in image c). From image a) to c) a progression from SD to PSD magnetic structure can be observed

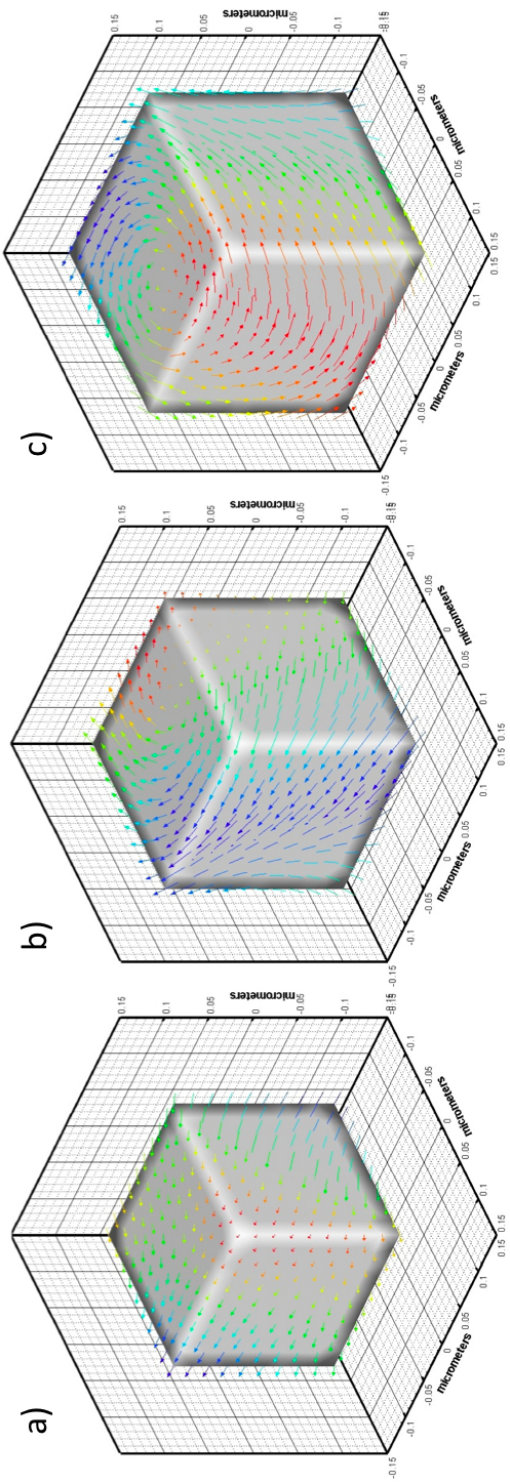

Figure 6.2: Models of cubes with dimensions ranging through the critical SD dimension for titanomagnetite (TM60) where the dimensions are $0.18\mu m$ in image a), $0.2\mu m$ in image b) and $0.22\mu m$ in image c). As with Figure 6.1 a progression from SD to PSD structure can be observed.

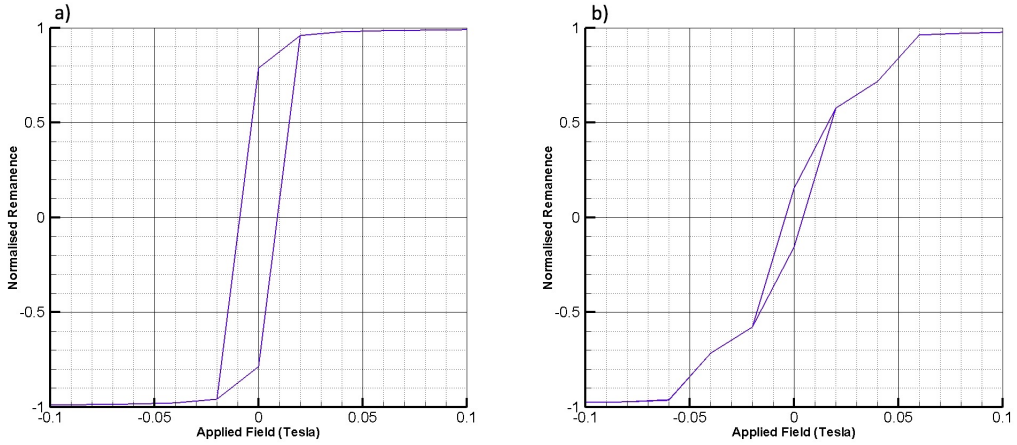

Figure 6.3: Hysteresis for maghemite where the dimensions are $0.05\mu m$ and $0.07\mu m$ from left to right.

6.3 Magnetite-Maghemite

The magnetite-maghemite system is important due to the oxidation process where maghemite is the fully oxidised version of the magnetite structure. Depending on the conditions present during the oxidation process maghemite will be produced as an intermediate stage before converting to haematite as seen in the list below [Lepp (1957)]. The structure of maghemite is identical to that of magnetite being cubic with an easy axis in the [111] direction. However, maghemite is not stable and will only occur as an intermediate phase and at high temperatures maghemite will convert to haematite. This system is of interest geologically as it is prevalent within red beds, these beds are sedimentary rocks that have been deposited in hot climates under oxidising conditions. These beds get their characteristic red colour from the iron oxide within their composition. Modelling of these systems can therefore help to test the fidelity of palaeomagentic samples from such areas [Petrovský et al. (1996)].

1) $4Fe_3O_4 + O_2 \rightarrow 6\gamma - Fe_2O_3$ **From 200°C to 375°-400°C**

2) $\gamma - Fe_2O_3 \rightarrow \alpha - Fe_2O_3$ **From 375°C to 525°-550°C**

3) $4Fe_3O_4 + O_2 \rightarrow 6\alpha - Fe_2O_3$ **From 550°-575°C**

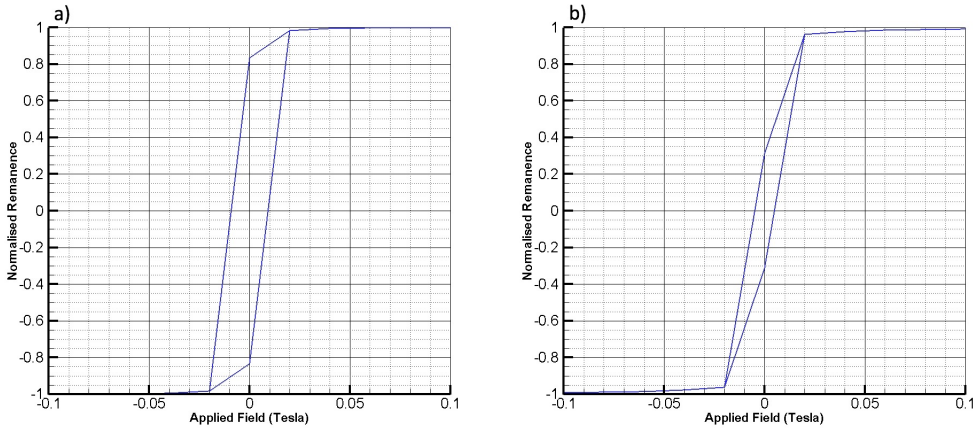

Figure 6.4: Hysteresis for TM60 where the dimensions are $0.18\mu m$ and $0.22\mu m$ from left to right.

In the following examples a volume with dimensions as seen in Figure 6.5 was generated where the magnetic phases of the cuboid are arranged in two different ways seen in Figure 6.5 image a) and image b). One example, Figure 6.5 image a), has the system bisected parallel to the xy-plane and the other, Figure 6.5 image b), bisected parallel to the yz-plane. Figure 6.5 image c) shows the result where the full structure is magnetite and Figure 6.5 d) where the full structure is maghemite.The values used in these models are displayed in Table 6.1.In Figure 6.5 we have a system where the magnetite phase is more homogeneous than the maghemite phase.

Figure 6.6 uses the geometry shown Figure 6.5 image a). In Figure 6.6 images c) and d) the outer edge of each material is highlighted to make the differences in phases more clear, although the difference between images is extremely subtle. This result indicates that the magnetite phase is more homogeneous than the maghemite phase. This result is expected as the critical domain size is larger for magnetite. This different behaviour has previously been seen in the examples where the full geometry takes the values of only one of the phases such as in Figure 6.5, images c) and d).

Figure 6.7 uses the geometry shown in Figure 6.5 b) and has the same results as observed in Figure 6.6 where the magnetite phase is more homogeneous than the maghemite phase. Again this is shown in Figure 6.7 images c) and d) where the magnetite phase is highlighted in image c) and is almost uniformly green as oppose to that of the maghemite phase in image d). All the results in these examples are in good agreement with what would be expected.

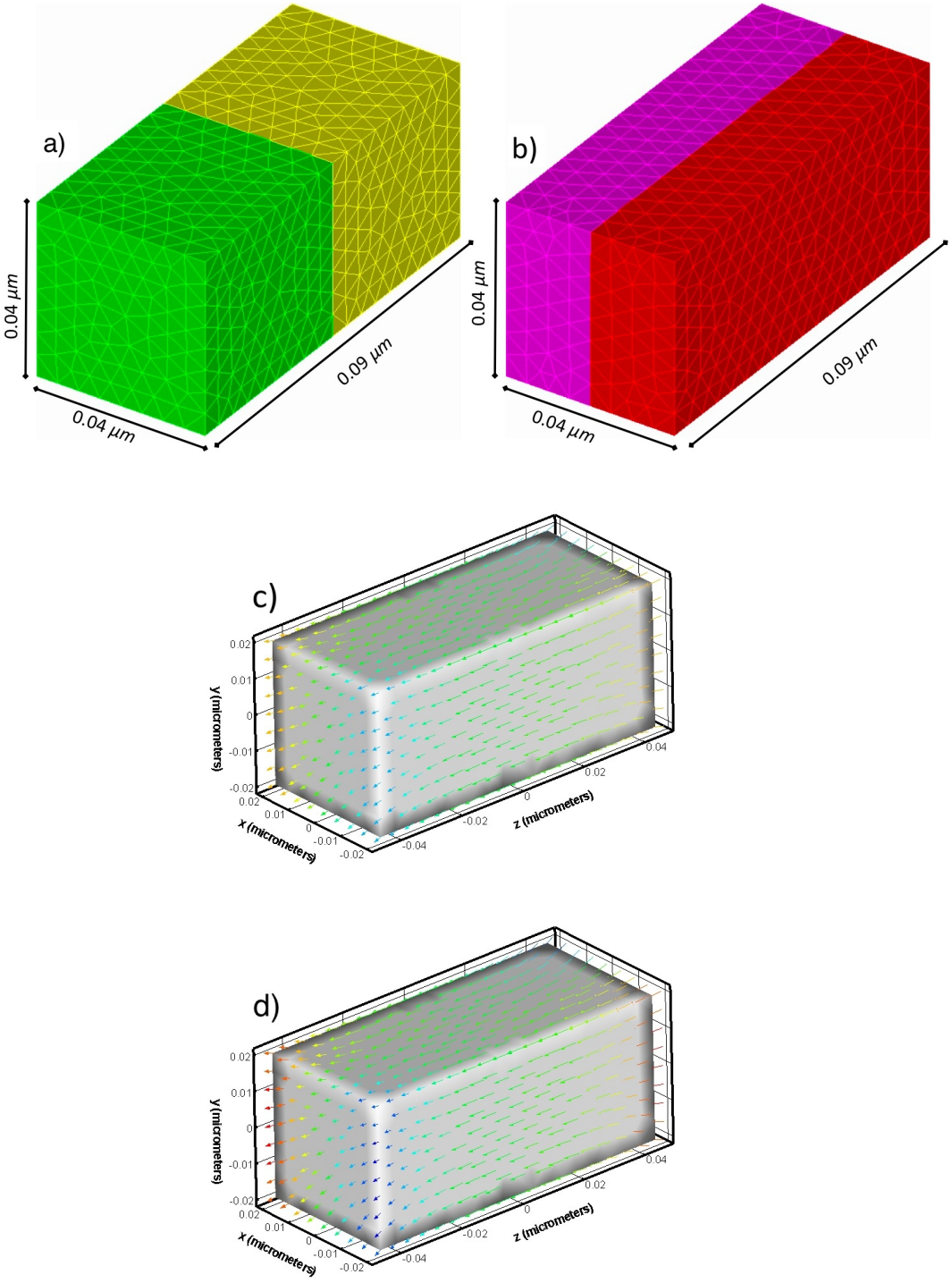

Figure 6.5: Images a) and b) show the two multiphase geometries used for the magnetite-maghemite system. The different colours of the blocks indicate how the geometry is split into the two different magnetic phases. Images c) and d) show the full structure as only magnetite and maghemtite respectively. It can be seen that image c) the full magnetite system is more homogeneous than image d) the full maghemite system. This can be discerned by the less intense darker red and red vectors in image d) showing more flowering.

Figure 6.6: Image a) displays the geometry used and b) the overall magnetic structure observed in this model. Images c) and d) highlight the structure of the magnetite and and maghemite phases respectively by drawing attention to the differences in the magnetic structures in the two phases. The magnetite phase in image c) can be seen to be more homogenous than the maghemite highlighted in image d) as the vectors at the edges have a darker red ad blue than those in image c). The difference is however very subtle.

Figure 6.7: Figure showing a) the geometry used and b) the overall magnetic structure. Images c) and d) highlight the structure of the magnetite and and maghemite phases respectively. In this example the magnetite phase highlighted in image c) is again more homogeneous than the maghemite phase highlighted in image d), this example is more obvious than that in Figure 6.6.

6.4 Magnetite-Maghemite oxidation

The next set of figures examine a more complex multiphase magnetic structure which was generated to examine the oxidation process more closely. The physical system is assumed to have an initial state of an octahedron of magnetite. It is assumed that this magnetite octahedron undergoes oxidation resulting in the exterior surface converting to maghemite first with the oxidation progressing from the outside in and eventually the entire structure being composed of maghemite. The end states of this system of a full magnetite and a full maghemite geometry have been modelled. In addition points at which the structure is multiphase, therefore consisting of both magnetite and maghemite, are simulated. The geometry of this system is generated by first producing an octahedron of dimensions of 170nm along its long edges as seen in Figure 6.8 a). In addition the structure is split into multiple layers as seen in Figure 6.8 b) where the material parameters of the the layers can be controlled.

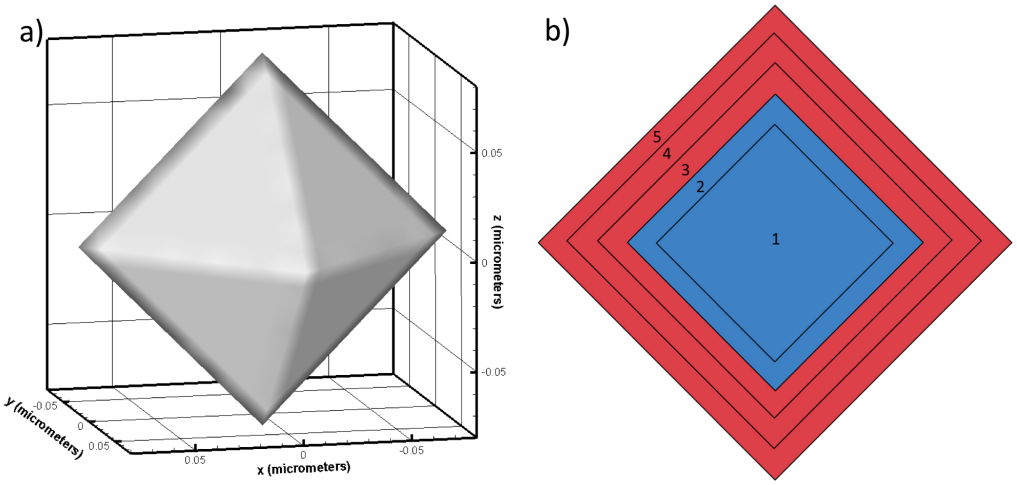

Figure 6.8: Figure showing the geometry used for the oxidation system. Image b) shows a sketch of the different layers, where one or more of these layers can be represented by maghemite or magnetite depending on the stage within the oxidation process.

Models were run with varied structures: where the full structure was maghemite, the full structure was magnetite, and also using intermediate struc-

tures with varying percentages of maghemite. This percentage of maghemite was controlled by selecting the appropriate number of shells and assigning them maghemite values. The model results are shown in the following figures, where both the results of the multiphase system have been shown and also the results from the magnetite portion only in each of the multiphase systems (Figures 6.9and 6.10 respectively).

The magnetite plots in Figure 6.9 show a progression from SD to a PSD structure as the volume is increased, where the vortex first nucleates at the vertex edge in image d) and at the centre of the face in image e). Between models e) and f) a change is observed in the direction of the vortex structures. Examining the multiphase results in Figure 6.10 it is observed that the overall magnetic structure of the full maghemite system shown in image a) is identical to the magnetic structure observed in Figure 6.9 image e) for the magnetite core where only one shell is absent. As two shells of maghemite are added to the magnetite octahedron, (Figure 6.10 images b) and c) respectively), the overall structure remains identical to the full maghemite case. However, as the number of maghemite layers are increased, a change is seen in the overall magnetic structure to become that of the structure for the full magnetite system seen in Figure 6.9, image f).

The associated hysteresis plots of the system are shown in Figure 6.11. As shown in Figure 6.11 the coercivity of the intermediate models where the system contains both the magnetite and maghemite phases varies depending on the percentage of maghemite in the system. The coercivity of maghemite found in this study is lower than that of the magnetite; as the volume of the maghemite is increased in the system the overall coercivity of the system decreases.

In Figure 6.12 the results from this study have been plotted with some experimental observations [Dunlop (1986), Levi and Merrill (1978), Heider et al. (1987)]. The theoretical values for the system are all extremely high in comparison with the experimental values. The magnetite with maghemite results are the values for the multiphase system where they have been plotted with respect to the dimensions of the resultant magnetite core in each case. The magnetite results

are the results for the magnetite cores as seen in Figure 6.9. It can be observed that the coercivity of the system is reduced by adding a skin of maghemite in all cases. This result indicates that partially oxidised system like these modelled systems may be less reliable within palaeomagnetic studies.

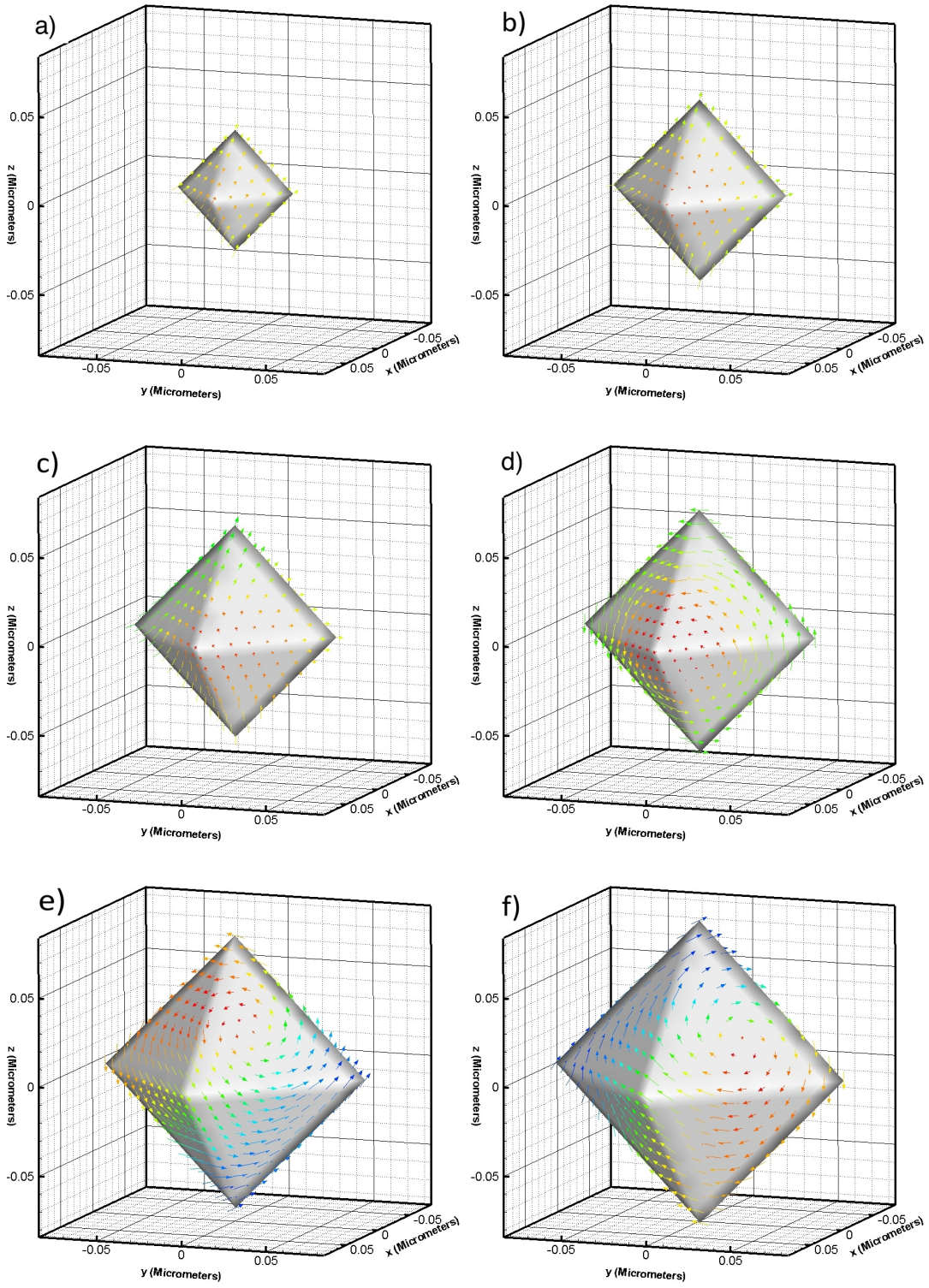

Figure 6.9: Set of images showing the models for the magnetite core in each of the multiphase examples up to and including image e). Image f) assumes the entire structure is magnetite.

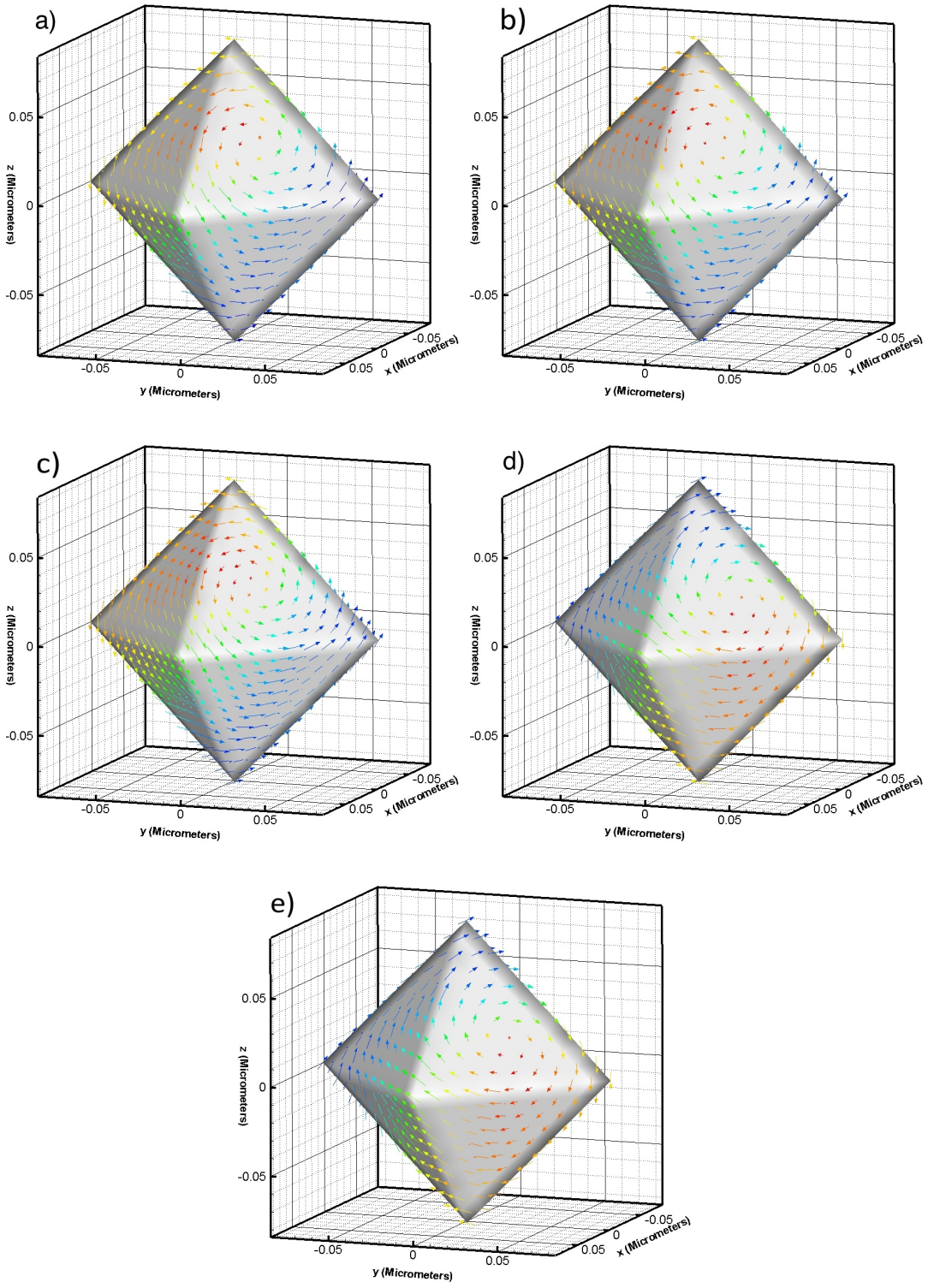

Figure 6.10: Set of images showing the models for the multiphase systems. Image a) shows the results where the entire system is assumed to be maghemite and the following models are where the maghemite values are applied to 1,2,3 and then 4 layers counting from the outside in.

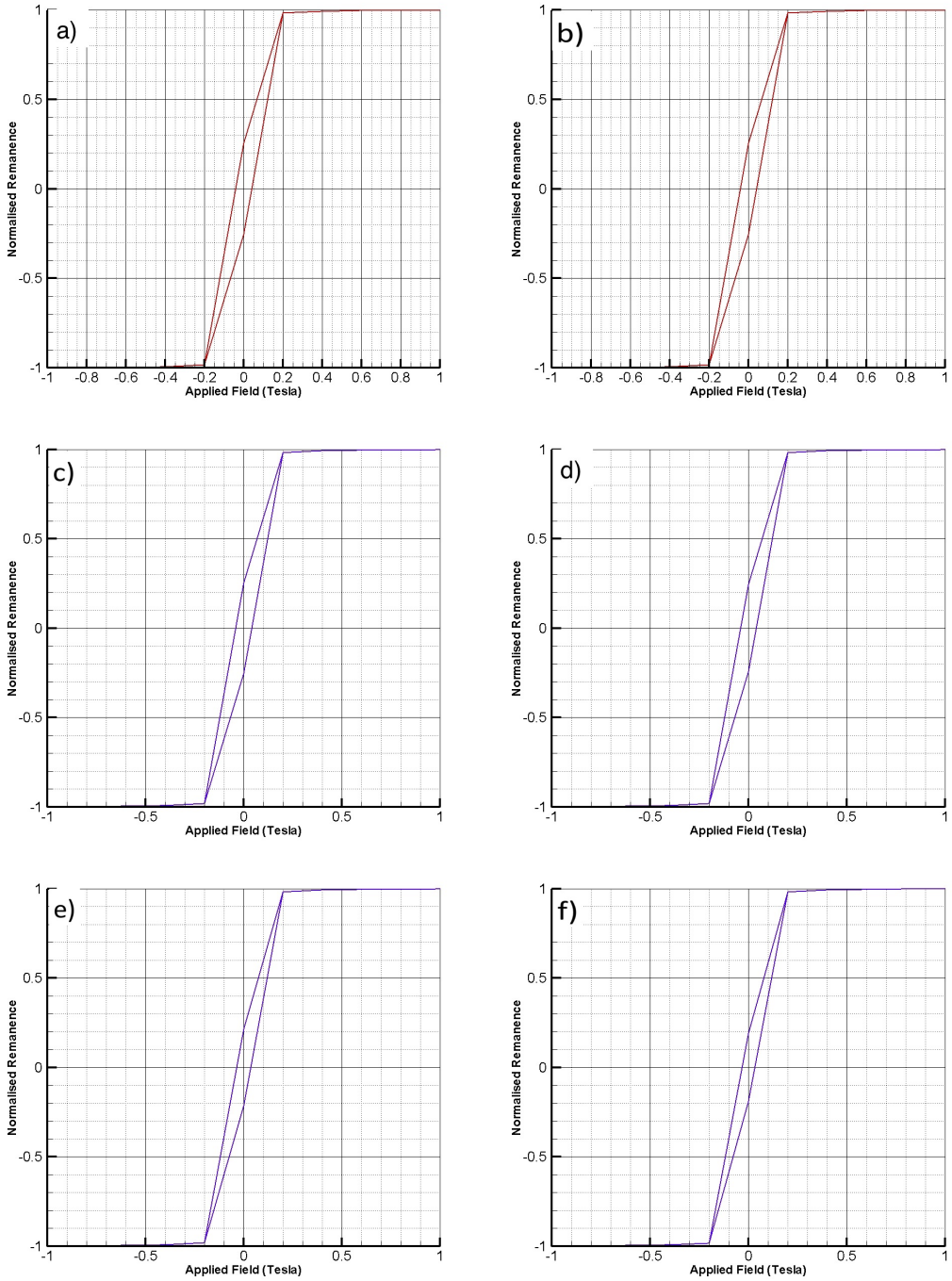

Figure 6.11: Modelled hysteresis for magnetite with maghemtite skin where images a) and b) show the results for the full magnetite and maghemite system respectively. The images c) to e) correspond to the results for 1,2,3 and 4 layers. The coercivity is reduced from images c) to e) as the proportion of maghemite is increases.

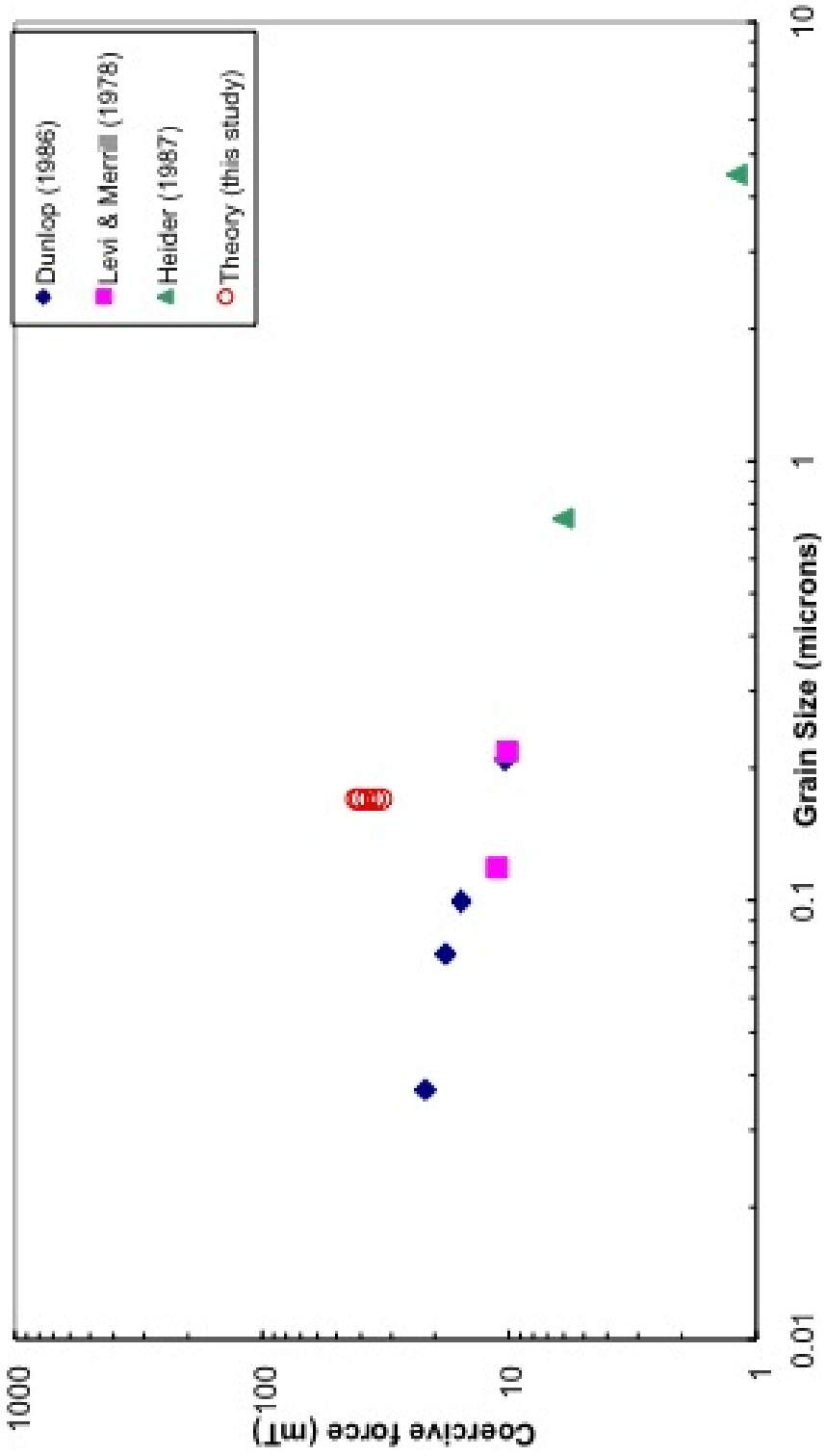

Figure 6.12: Log plot of the values from this study plotted with experimental results from Dunlop (1986), Levi and Merrill (1978) and Heider et al. (1987). The red circles indicate the magnetite maghemite system and show a decrease in coercivity as the proportion of maghemite in the system is increased.

6.5 Magnetite -Titanomagnetite

This section examines the models representing magnetite with an intermediate member of the titanomagnetite series, TM60. Figure 6.13 shows an example of two SD magnetic phases on contact and Figure 6.14 is an example where both phases have more complex magnetic structures. The titanomagnetite TM60 was used, as K_1 and M_s are well constrained for this material.

The material constants used for the subsequent models can be found in Table 6.2. The titanomagnetites share a common structure with magnetite, therefore no revisions of the magnetocrystalline anisotropy form is required. Instead only the constants of the system are altered and the easy axis is once again along the [111] direction. As mentioned in section 2.7 there is a great degree of flexibility between the titanomagnetite phases, so a magnetite titanomagnetite solid solution would not be uncommon [Bleil (1976)], a good example of this being mid-ocean ridge basalts where titanomagnetites are one of the primary magnetic carriers [Wang and Van der Voo (2004), Krása and Matzka (2007)].

Direct imaging of titanomagnetite-magnetite solid solutions often shows textures associated with exsolution, therefore lamellae similar to those seen in Figure 5.1 or more blocky lamellae [Evans and Wayman (1974)]. However, in the following examples far simpler geometries have been used.

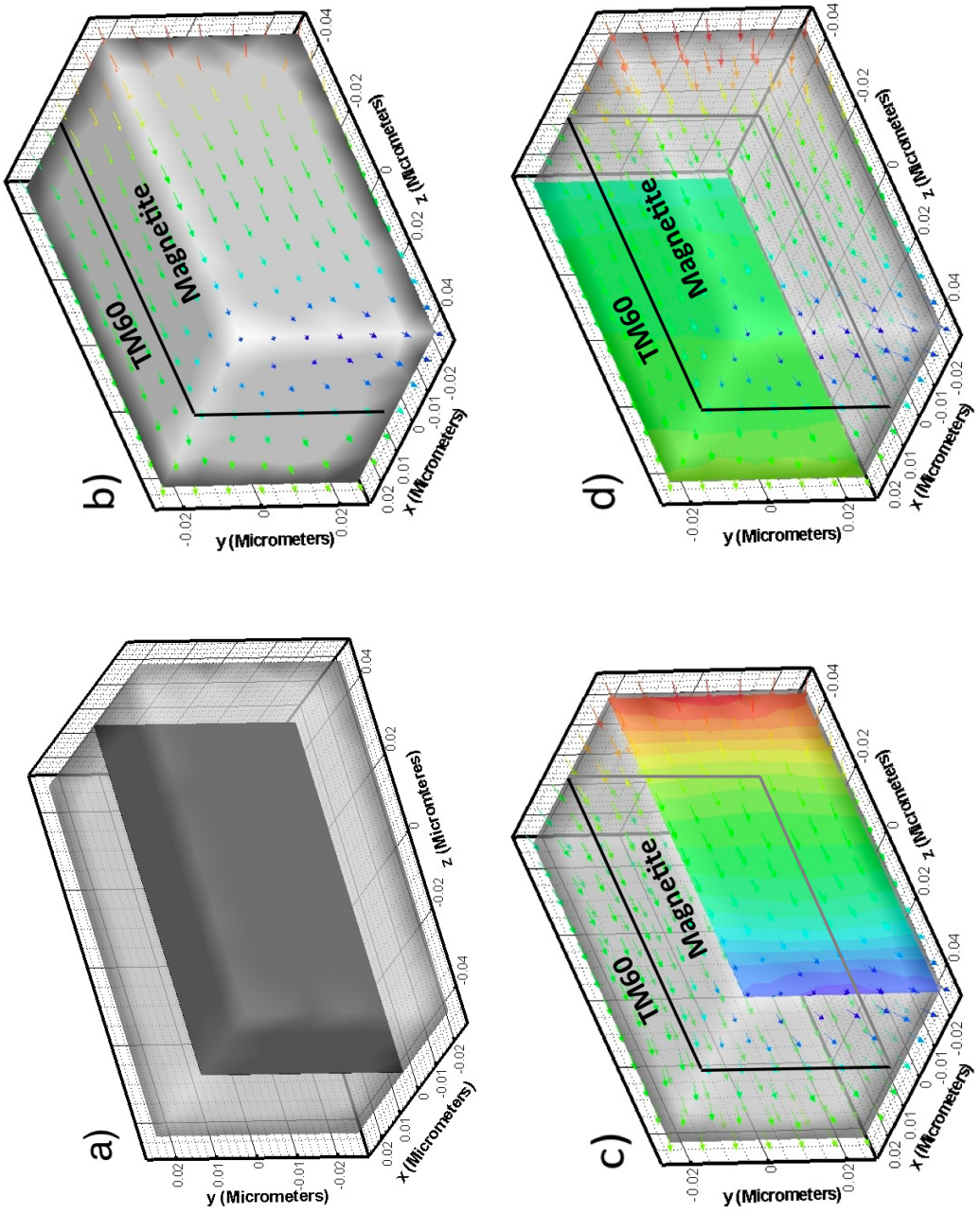

Figure 6.13: Figure showing a) the geometry used and b) the overall magnetic structure. Images c) and d) highlight the structure of the magnetite and TM60 phases respectively. In this example the TM60 phase highlighted in image d) is far more homogeneous than the magnetite phase seen in image c).

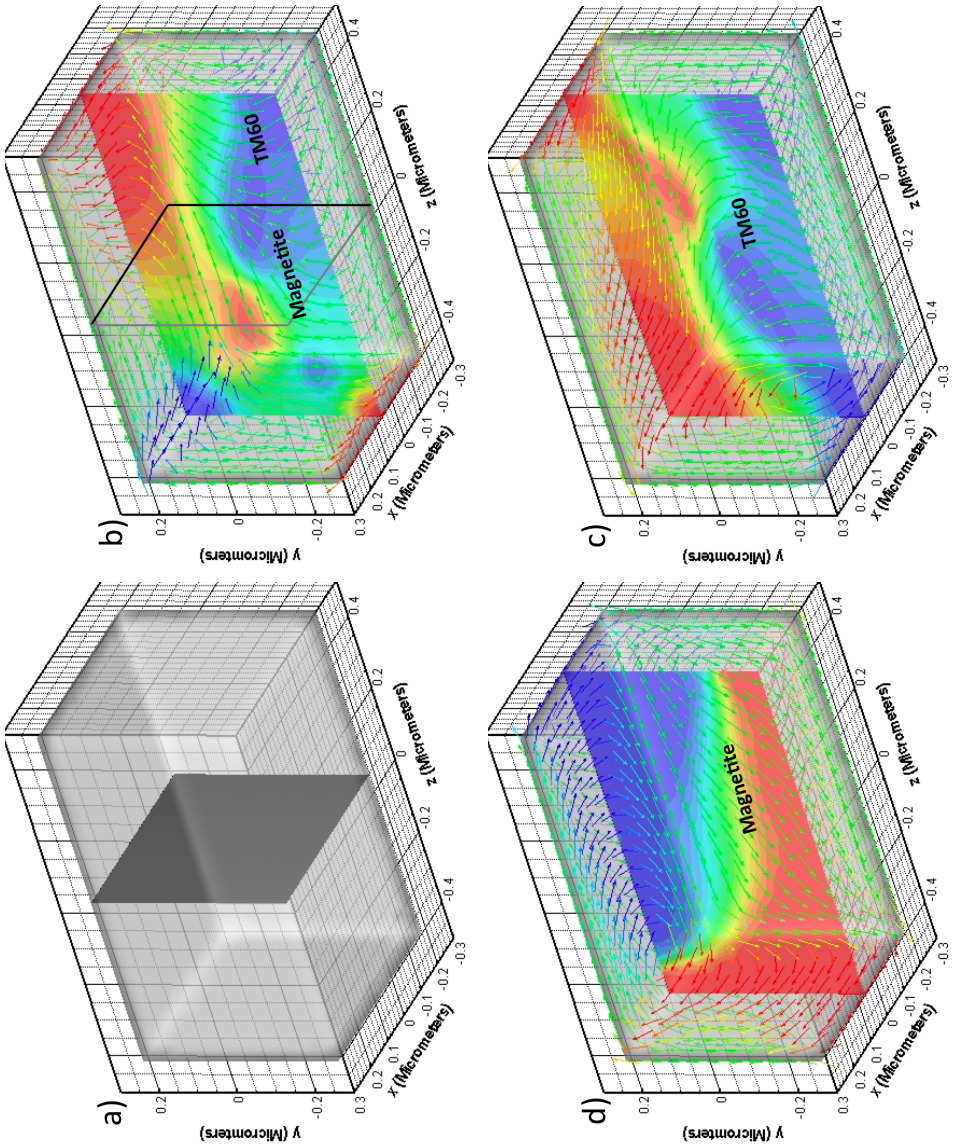

Figure 6.14: Figure showing a) the geometry used and b) the overall multiphase structure. Images c) and d) highlight the structure of the magnetite and TM60 phases respectively. In this case the highlighted portion of the magnetite phase in image b) is different to the structure seen in the overall magnetite structure seen in image c) the TM60 portion of the multiphase structure in in image b) resembles the structure seen in image d)

Figure 6.13, where the geometry is split as seen in image a), shows the results where a SD structure would be expected for both phases. The structure observed in Figure 6.13 b) is similar to the example shown in Figure 6.7 b), where in this case the TM60 phase is more homogeneous than the magnetite phase. The TM60 phase has little to no flowering at the edges as seen in Figure 6.13 image d), which would be expected as the critical domain size of TM60 is several orders of magnitude larger than that of magnetite.

Figure 6.14 shows a far larger structure which, expectedly, has a more complex structure for both the magnetite and TM60 phase highlighted in images c) and d) respectively. In the full magnetite model in Figure 6.14 image c) there can be observed a magnetic structure within both the xy plane and the zx plane. On the right hand face of Figure 6.14 image c), showing the full magnetite system, there is a vortex structure centred within the xy plane and on the right hand side a vortex structure within the xz plane. The full TM60 model in Figure 6.14 image d) has a continuous vortex structure with its centre within the xy plane. The multiphase structure in Figure 6.14 image b) has a clear structure change from one material to the other, with the TM60 region showing a similar structure to that seen in the full TM60 model. The magnetite phase of the system is quite different from the full magnetite model, although magnetic structures are still observed within the xz plane.

6.6 Application of multiphase model to irregular structures

The multiphase geometry used for this structure, shown in Figure 6.15, is identical to the previous geometry used in Chapter 5, Figure 5.14, where a full magnetite structure was modelled. The only difference to this structure was the addition of node groupings to allow the identification of different material regions. Importantly, due to the small separation distances between the individual lamellae, the

nodes were selected as seen in Figure 6.15. In this case the boundary nodes were assumed to have exclusively material two value as the lamellae separation was only one element width. As the value of the exchange for an element is constant, and constructed by the values of the individual nodes, to produce the desired effect a larger/lower value would have to be used to compensate for the averaging effect.

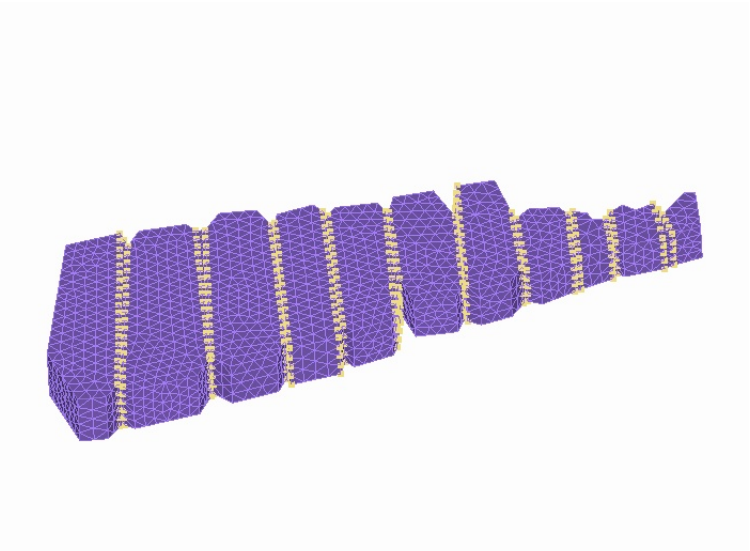

Figure 6.15: The yellow markers indicate the nodes which take the material two values within the system. These markers follow the edges of the lamellae in the system.

There is no information regarding the material constants for ulvöspinel, and therefore this section has been undertaken using a purely theoretical approach. Using sections 6.3 and 6.4 as a starting point for estimating the value of the parameters, the boundary nodes were altered as a percentage of the values of magnetite.

The following presents a selection of models where only the value of A_{ex} has been altered at the grain boundaries and the values for m_s and K_1 remain constant. Table 6.3 shows the A_{ex}value used for each model, the values of M_s and K_1 being identical to those seen in Table 4.1. There are two distinct groups of results. The first set are the results where A_{ex} has been altered significantly,

that is by an order of magnitude. The second set show the results where the value has been altered less dramatically, in this case running from 0.2× the A_{ex} of magnetite up to 1.8× the A_{ex} of magnetite.

The second set of figures, Figures 6.27 to 6.30, are the results of varying not only the exchange but all the other constants on the boundary nodeset. Once again these value are altered as a factor of the values of magnetite. The models have values equal to 0.8, 1.2, 1.4 and 1.6 times that of magnetite respectively. As before, all of these results are displayed with a smaller image of the non-bridged model for ease of comparison.

Table 6.3: Values used for the irregular multiphase structures

Figure	Anisotropy (K_1)	Exchange (A_{ex})	Saturation magnetisation (M_s)
Large exchange alteration			
Figure 6.16	$-1.24 \times 10^4 J/m^3$	$1.34 \times 10^{-09} J/m$	480 kA/m
Figure 6.17	$-1.24 \times 10^4 J/m^3$	$1.34 \times 10^{-10} J/m$	480 kA/m
Figure 6.18	$-1.24 \times 10^4 J/m^3$	$1.34 \times 10^{-12} J/m$	480 kA/m
Exchange alteration only			
Figure 6.20	$-1.24 \times 10^4 J/m^3$	$2.68 \times 10^{-12} J/m$	480 kA/m
Figure 6.23	$-1.24 \times 10^4 J/m^3$	$6.7 \times 10^{-12} J/m$	480 kA/m
Figure 6.24	$-1.24 \times 10^4 J/m^3$	$8.04 \times 10^{-12} J/m$	480 kA/m
Figure 6.25	$-1.24 \times 10^4 J/m^3$	$1.07 \times 10^{-11} J/m$	480 kA/m
Full constant alteration			
Figure 6.27	$-9.92 \times 10^3 J/m^3$	$1.07 \times 10^{-11} J/m$	384 kA/m
Figure 6.28	$-1.94 \times 10^4 J/m^3$	$1.61 \times 10^{-11} J/m$	576 kA/m
Figure 6.29	$-1.74 \times 10^4 J/m^3$	$1.88 \times 10^{-11} J/m$	672 kA/m
Figure 6.30	$-1.98 \times 10^4 J/m^3$	$2.14 \times 10^{-11} J/m$	768 kA/m

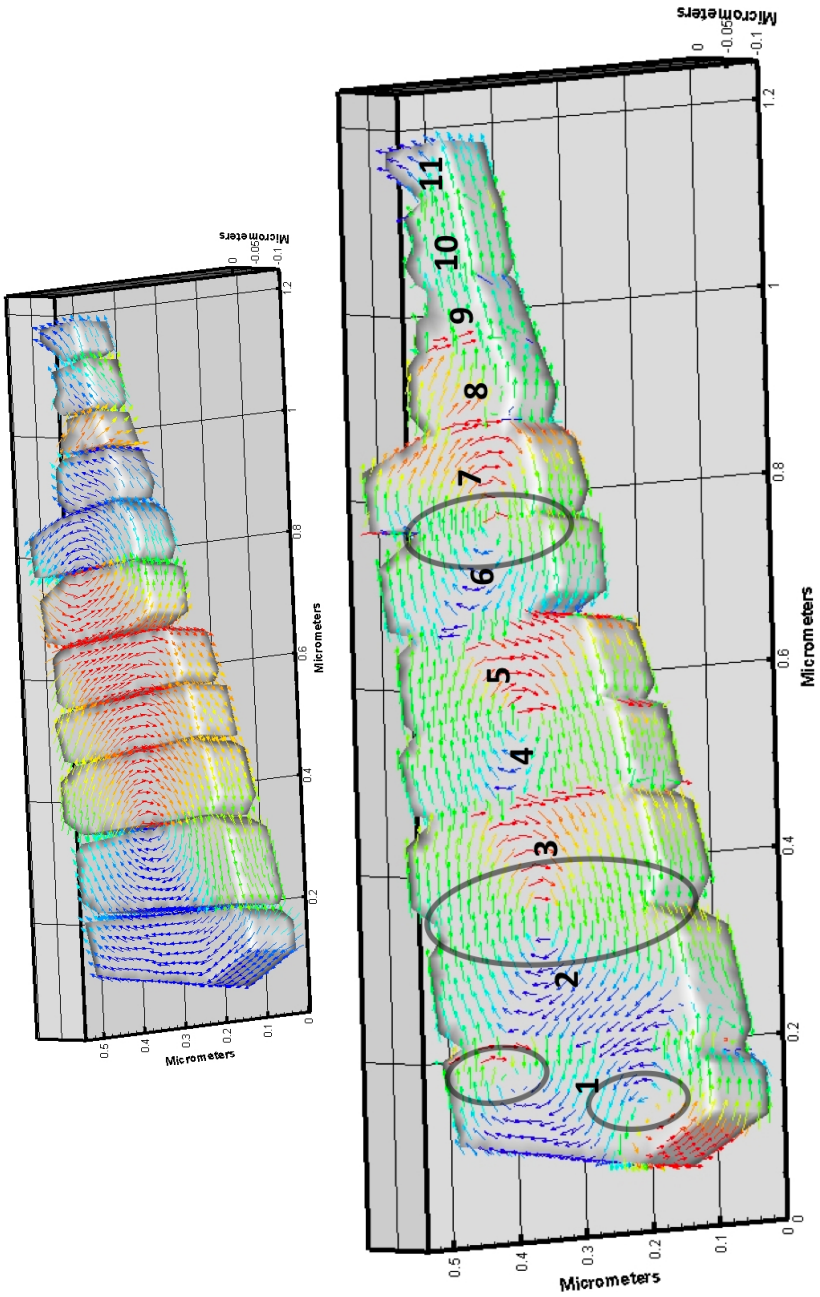

Figure 6.16: The top image is that of the non-bridged system. The bottom image shows the magnetic structure observed where the boundary nodes have been given an A_{ex} value 100× that of magnetite. Although a vortex is still evident between lamellae 6 and 7, it is in the opposite direction to that seen in the non-bridged model. Lamellae 1 to 5 contain many more vortex/partial vortex structures than seen in the non-bridged model. In particular lamella 1 contains two fully formed vortices within the body of the lamella.

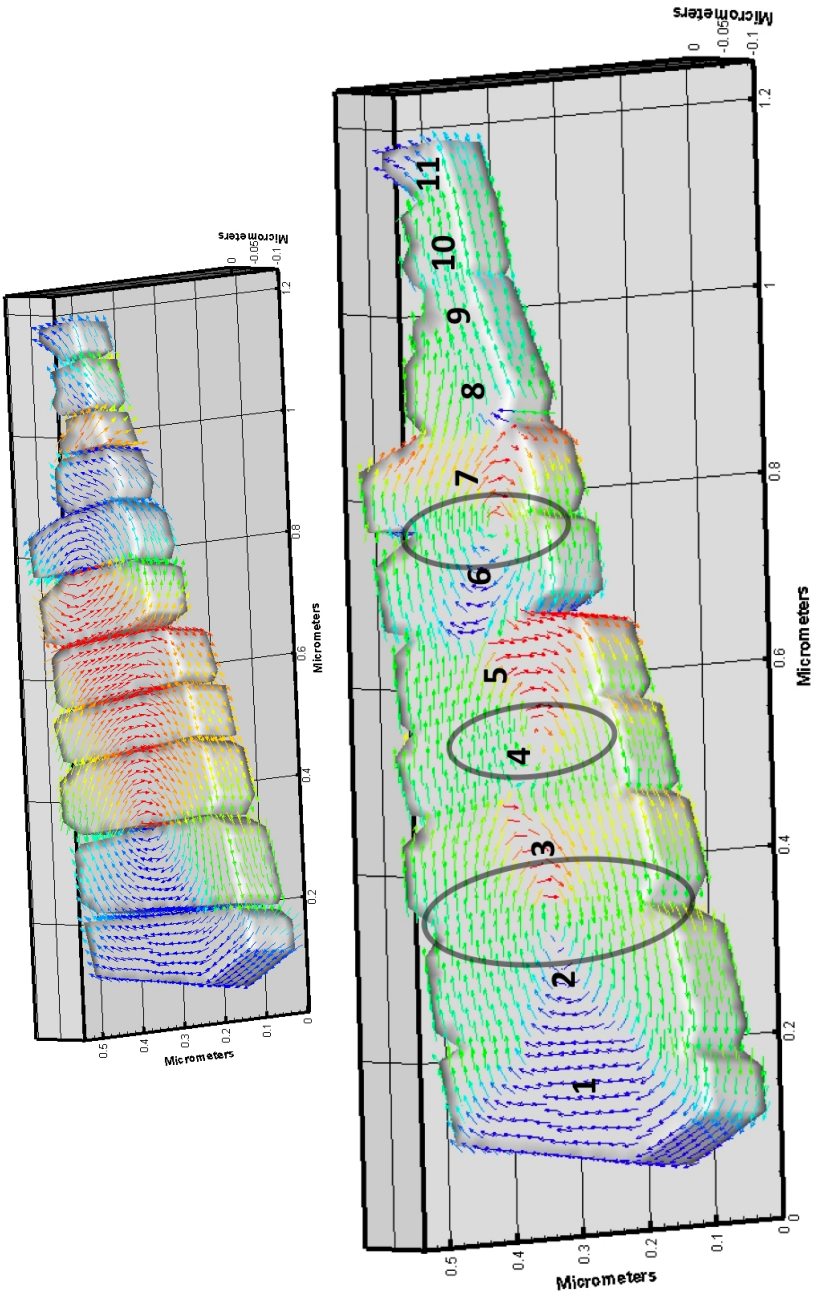

Figure 6.17: The top image is that of the non-bridged system. The bottom image shows the magnetic structure observed where the boundary nodes have been given an A_{ex} value 10× that of magnetite. A vortex is still evident between lamellae 6 and 7. However, it is in the opposite direction to that seen in the non-bridged model. This model is similar to the non-bridged model through lamellae 1 to 3. There appears to be a partial vortex forming at the edge between lamellae 4 and 5, unlike the full vortex structure seen in Figure 6.16

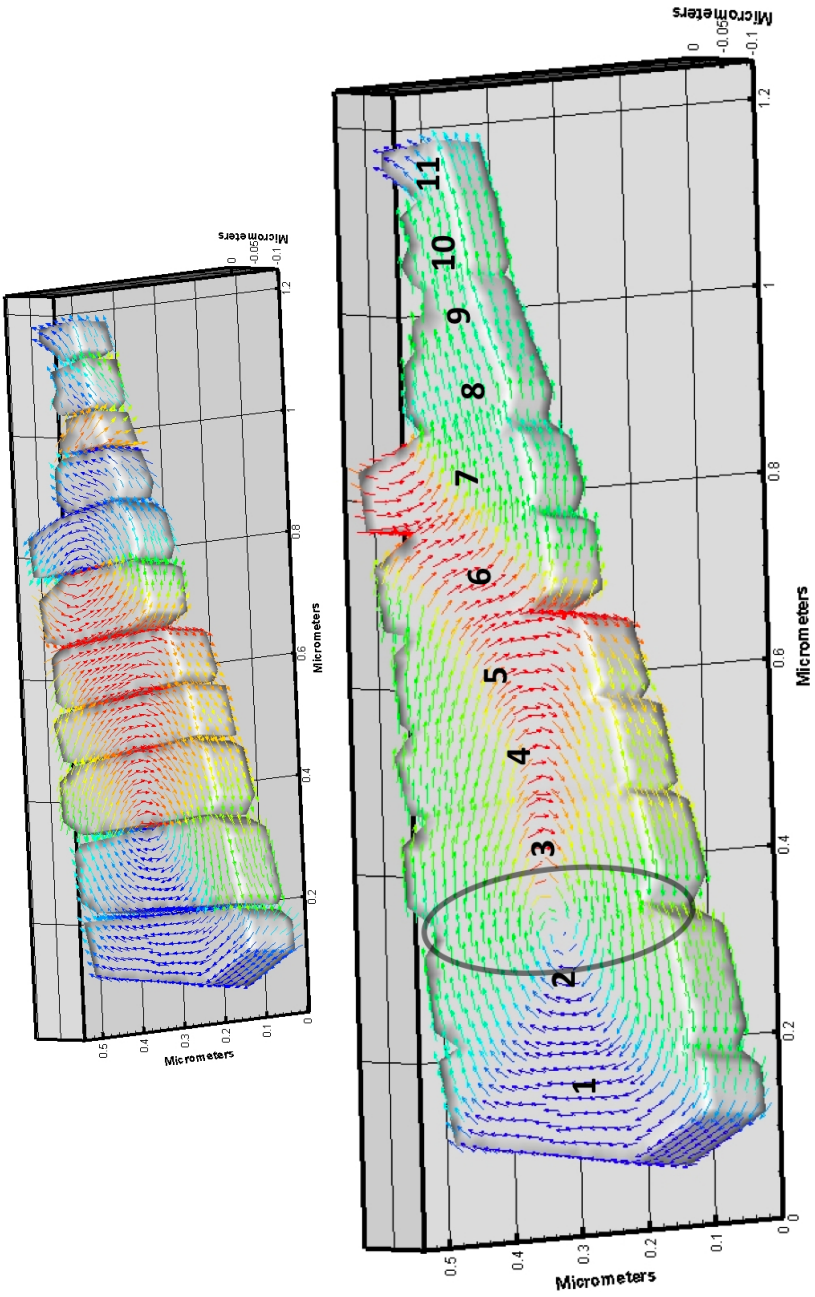

Figure 6.18: The top image is that of the non-bridged system. The bottom image shows the magnetic structure observed where the boundary nodes have been given an A_{ex} value $0.1\times$ that of magnetite. Lamellae 1 to 5 are very similar to their counterparts within the non-bridged model. However, the vortex structure between lamellae 6 and 7 in the non-bridged model is absent. The overall structure of this model is very similar to the full magnetite model in Figure 5.14 in Chapter 5, where the vortex between lamellae 6 and 7 is also missing.

This first set of models where only the value of the exchange has been altered significantly yields some interesting results. In the case of Figure 6.18 where the exchange value is $1.34 \times 10^{-12} J/m$ a result is obtained not dissimilar to the non-bridged result, particularly in lamellae one to four. Within the first four lamellae the vortex structure is still evident between lamellae two and three, but this vortex structure is different from that in the non-bridged case, having here a more circular structure as opposed to the slightly elliptical structure observed in the non-bridged model which more closely follows the lamellae edges.

Furthermore it can be seen that the magnetic structure within lamellae three to six is far more homogeneous than that of the non-bridged model, with a greater component of the magnetisation running perpendicular to the long axes of the individual lamellae. Finally it is evident that the second vortex structure is entirely absent and the smaller blockier lamellae are very much more homogeneous. This result is similar to the structures observed within Figure 5.14 showing an entirely magnetite structure.

Figures 6.16 and 6.17 both have the vortex structure between lamellae two and three and also between lamellae six and seven. However, both have additional features not seen in either Figure 6.18 or Figure 5.14. In the case of Figure 6.17 a third partially formed vortex structure is observed between lamellae four and five and, similarly, the vortex structure between lamellae two and three is not as distinct as that seen in Figure 6.18. This additional vortex structure is again positioned close to the lamellae edge.

Figure 6.16 is of particular interest, as in this model the partially formed vortex observed in Figure 6.17 between lamellae four and five is now fully formed and, again, situated at the lamellae edge. However, there are two vortex structures contained within the body of lamella one. This is the first example observed within this study of the nucleation of vortex states away from the lamellae edges, but it is also important to note that within this model there is far more magnetic structure observed within the z-plane. Figure 6.19 highlights this finding, allowing comparison of both the non-bridged model and Figure 6.16. The colouring of

Figure 6.19 highlights any magnetic structure in the z-plane, with red denoting a magnetisation direction into the page and blue out of the page. In the original model the out of plane components are confined to the vortex centres and the sharp corners of the lamellae only.

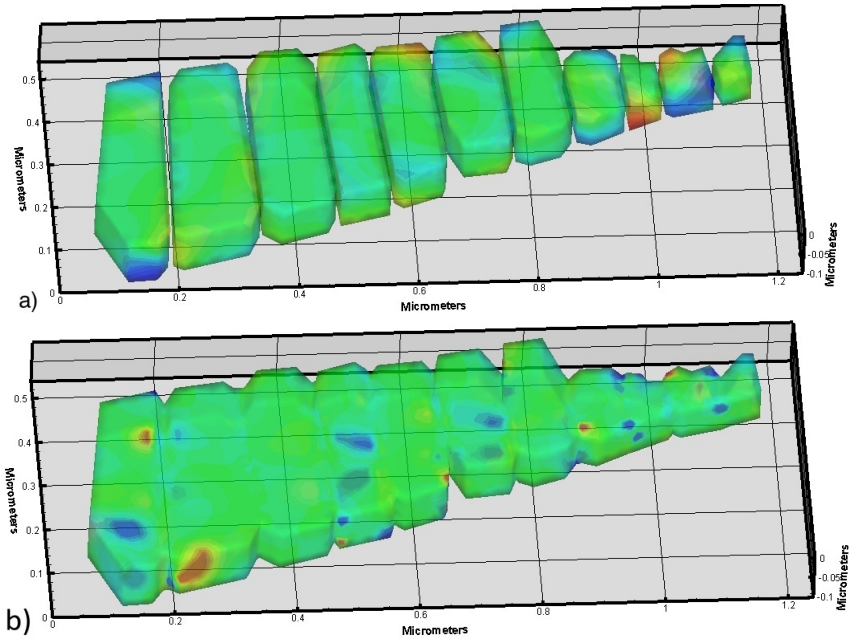

Figure 6.19: Figure showing the magnetic structure in the z-direction of the non-bridged model and multiphase model with altered exchange. Image a) shows the non-bridged and image b) the result for Figure 6.16.

When examining the direct observations one can only observe the in-plane magnetic structure of the system, however, using these lamellae depths one would not expect to see much magnetic structure within the z-plane of the system, with the exceptions of the vortex centres.

The following models correspond to the exchange value only being altered, the results corresponding to 0.2, 0.3, 0.4, 0.5, 0.6 and 0.8 A_{ex} times that of magnetite respectively.

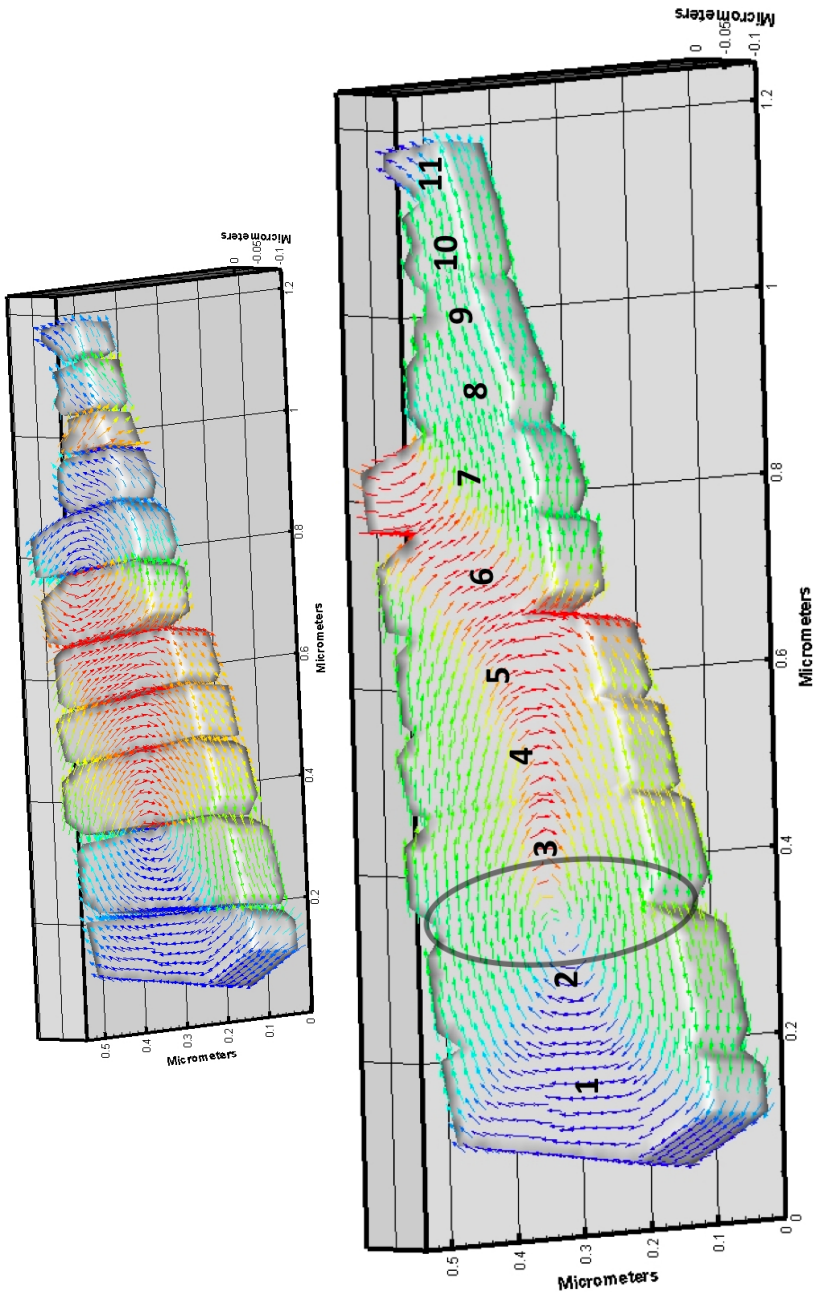

Figure 6.20: The top image is that of the non-bridged system. The bottom image shows the magnetic structure observed where the boundary nodes have been given an A_{ex} value 0.2× that of magnetite. Lamellae 1 to 5 are very similar to their counterparts within the non-bridged model. However, the vortex structure between lamellae 6 and 7 in the non-bridged model is absent. The structure in this system is almost identical to that observed in Figure 6.18.

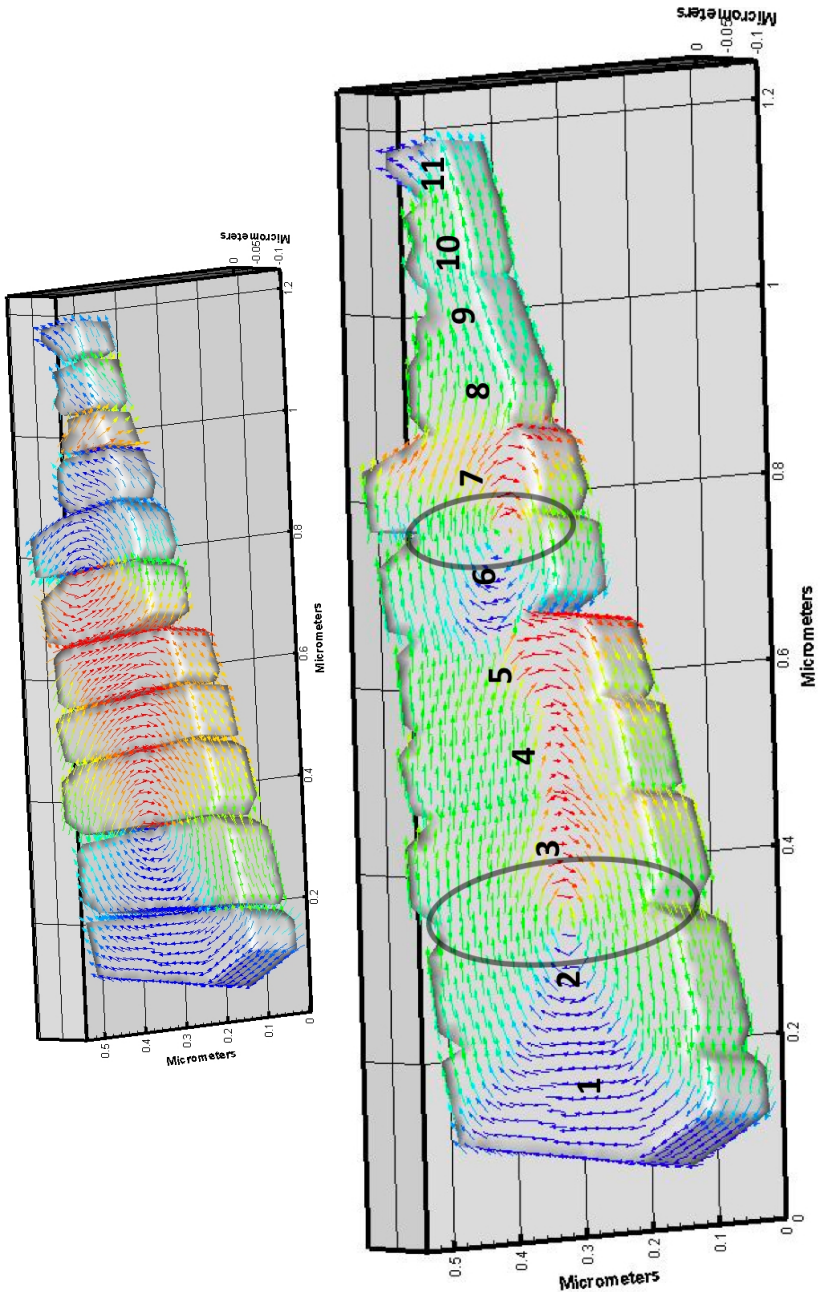

Figure 6.21: The top image is that of the non-bridged system. The bottom image shows the magnetic structure observed where the boundary nodes have been given an A_{ex} value 0.3× that of magnetite. Lamellae 1 to 5 are very similar to their counterparts within the non-bridged model. However, the vortex structure between lamellae 6 and 7 in the multiphase model is in the opposite direction to that of the non-bridged model.

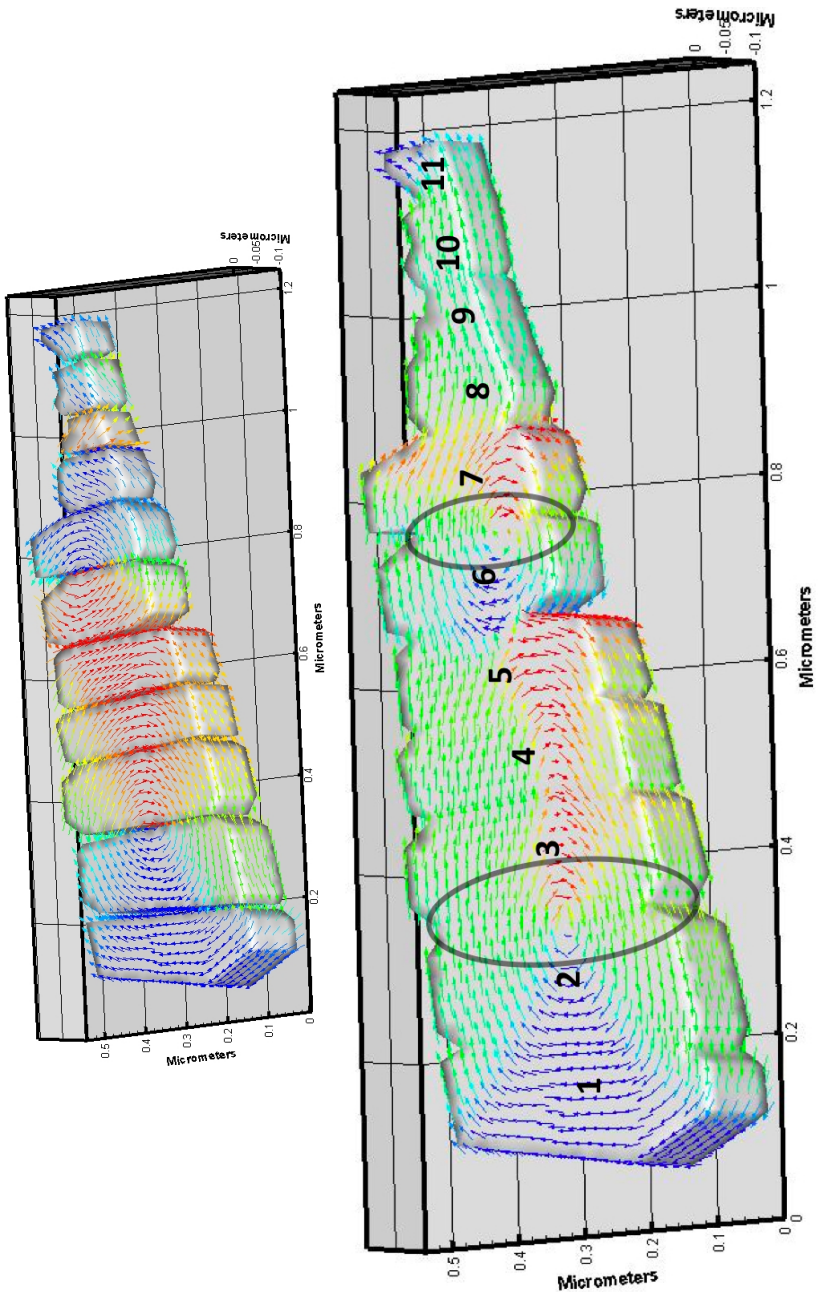

Figure 6.22: The top image is that of the non-bridged system. The bottom image shows the magnetic structure observed where the boundary nodes have been given an A_{ex} value 0.4× that of magnetite. Lamellae 1 to 5 are very similar to their counterparts within the non-bridged model. However, the vortex structure between lamellae 6 and 7 in the multiphase model is in the opposite direction to that of the non-bridged model. This structure is almost identical to that observed in Figure 6.21.

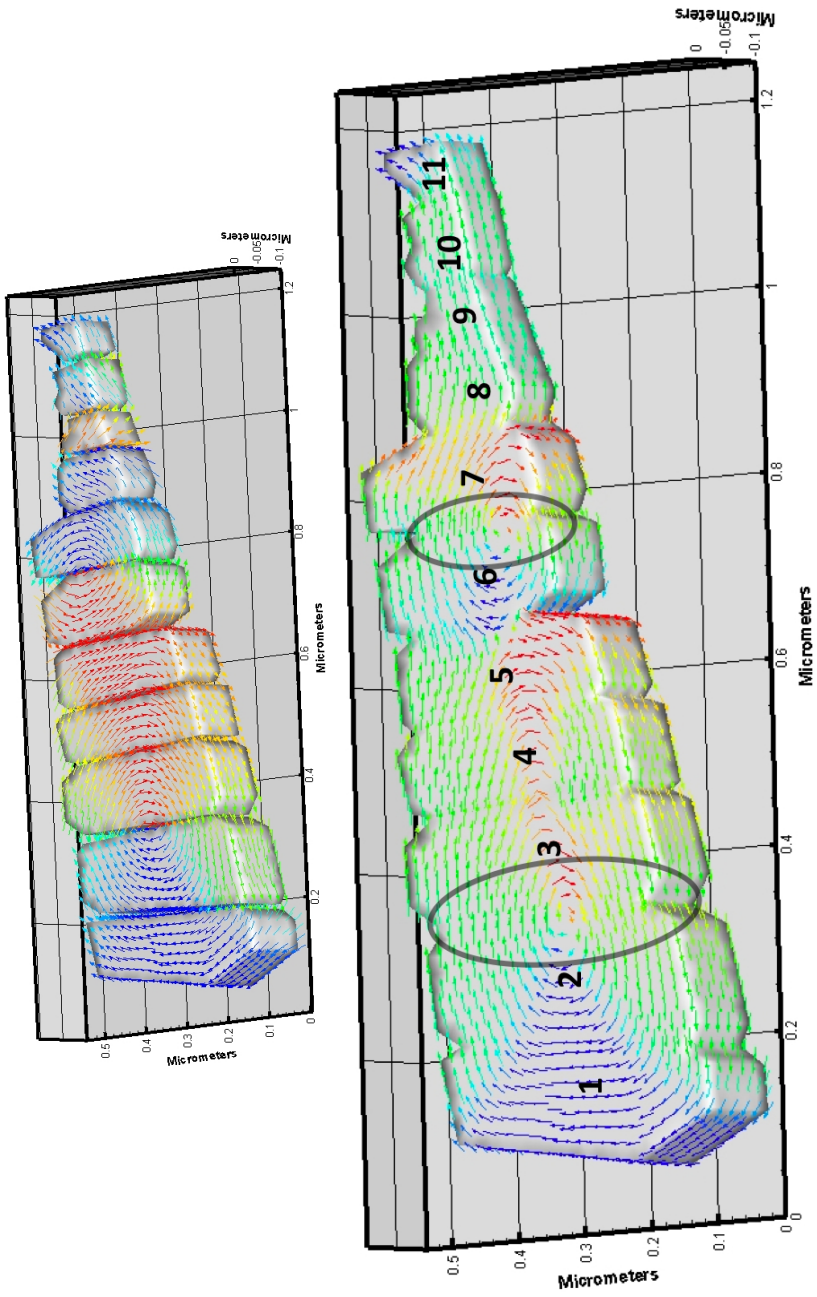

Figure 6.23: The top image is that of the non-bridged system. The bottom image shows the magnetic structure observed where the boundary nodes have been given an A_{ex} value 0.5× that of magnetite. Lamellae 1 to 5 are very similar to their counterparts within the non-bridged model. However, the vortex structure between lamellae 6 and 7 in the multiphase model is in the opposite direction to that of the non-bridged model. This structure is nearly identical to that observed in Figure 6.21.

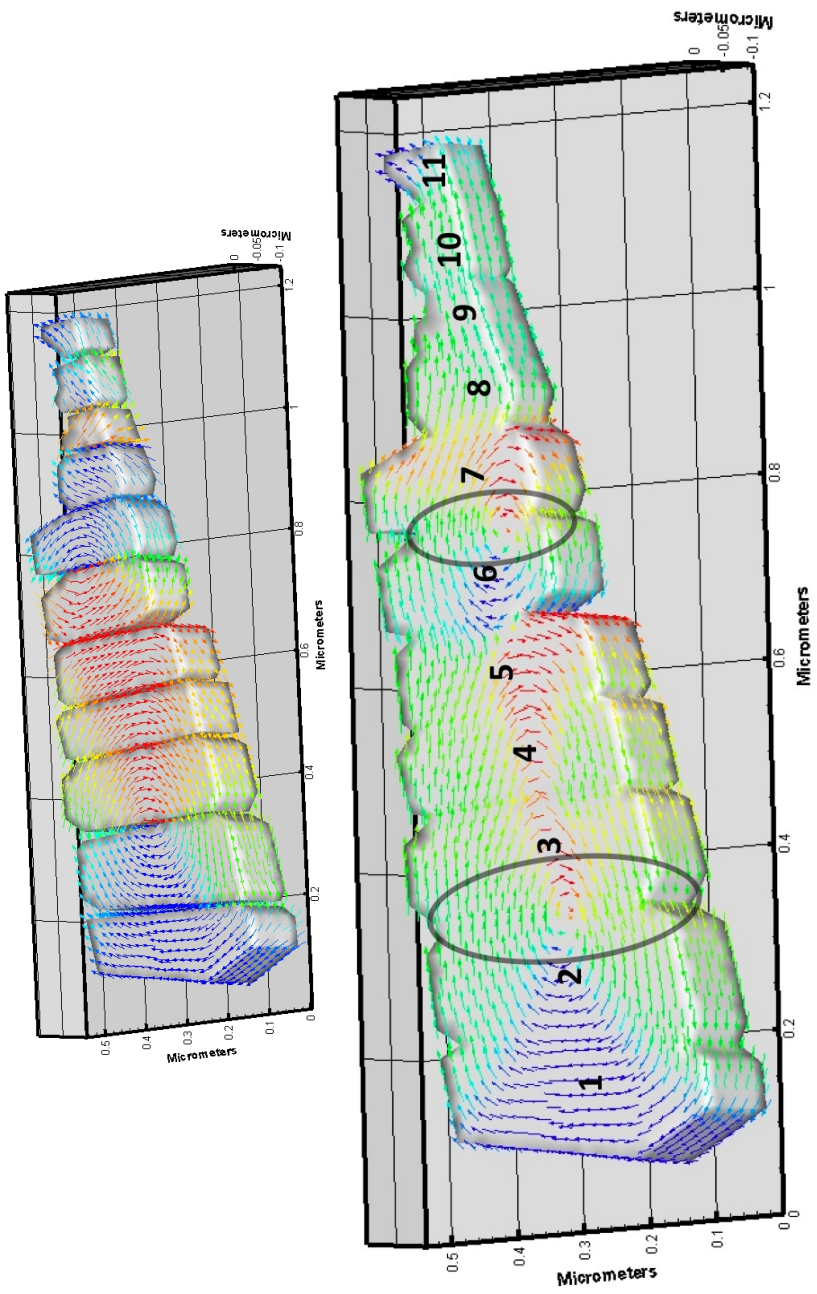

Figure 6.24: The top image is that of the non-bridged system. The bottom image shows the the magnetic structure observed where the boundary nodes have been given an A_{ex} value 0.6× that of magnetite. Lamellae 1 to 5 are very similar to their counterparts within the non-bridged model. However, the vortex structure between lamellae 6 and 7 in the multiphase model is in the opposite direction to that of the non-bridged model. This structure is almost identical to that observed in Figure 6.21.

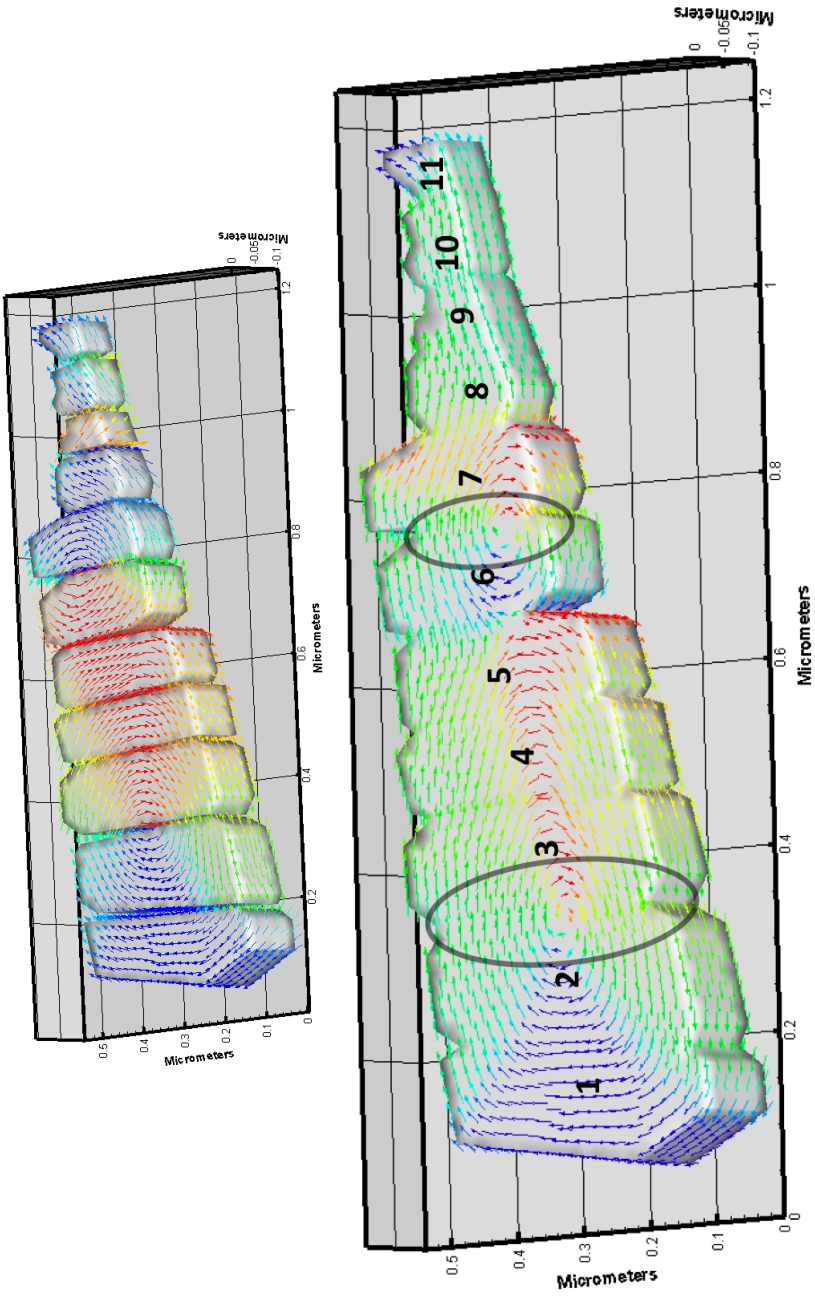

Figure 6.25: The top image is that of the non-bridged system. The bottom image shows the the magnetic structure observed where the boundary nodes have been given an A_{ex} value 0.8× that of magnetite. Lamellae 1 to 5 are very similar to their counterparts within the non-bridged model. However, the vortex structure between lamellae 6 and 7 in the multiphase model is in the opposite direction to that of the non-bridged model. This structure is nearly identical to that observed in Figures 6.21, 6.22 and 6.24.

Figure 6.20 has a very high degree of similarity to the result seen in Figure 6.18, which is to be expected as the values used for the exchange are very similar. As the value of the exchange is gradually increased through the other models (Figure 6.23 to Figure 6.25) there can be seen the emergence of the vortex structure between lamellae five and six which is absent in Figure 6.20. Interestingly Figure 6.25, although being very similar to the full magnetite case in Figure 5.14, has the vortex between lamellae five and six present whereas this is absent in Figure 5.14.

An additional result from these structures is that, when compared with the direct observation (Figure 6.26), it is evident that the vortex apparent between lamellae five and six in the models is consistently in the opposite direction to that in the direct observations. In the direct observations the magnetic structure in that area has an anti-clockwise direction whereas in the models the vortex is in a clockwise direction, this being indeed the case for all the models where this vortex exists. However, all these structures are in better agreement with the direct observations within lamellae three, four and five where the magnetic structure does not follow the length of the lamellae as rigidly as is seen in the non-bridged and physically bridged models.

Figure 6.26: Direct observation of the system. Note in particular the vortex within lamella number 6.

The following images all result from altering all the system constants of the nodeset by the same factor as opposed to merely altering the exchange value.

The results show firstly the effect of decreasing the magnetic constants and then subsequently the effect of increasing all the constants uniformly.

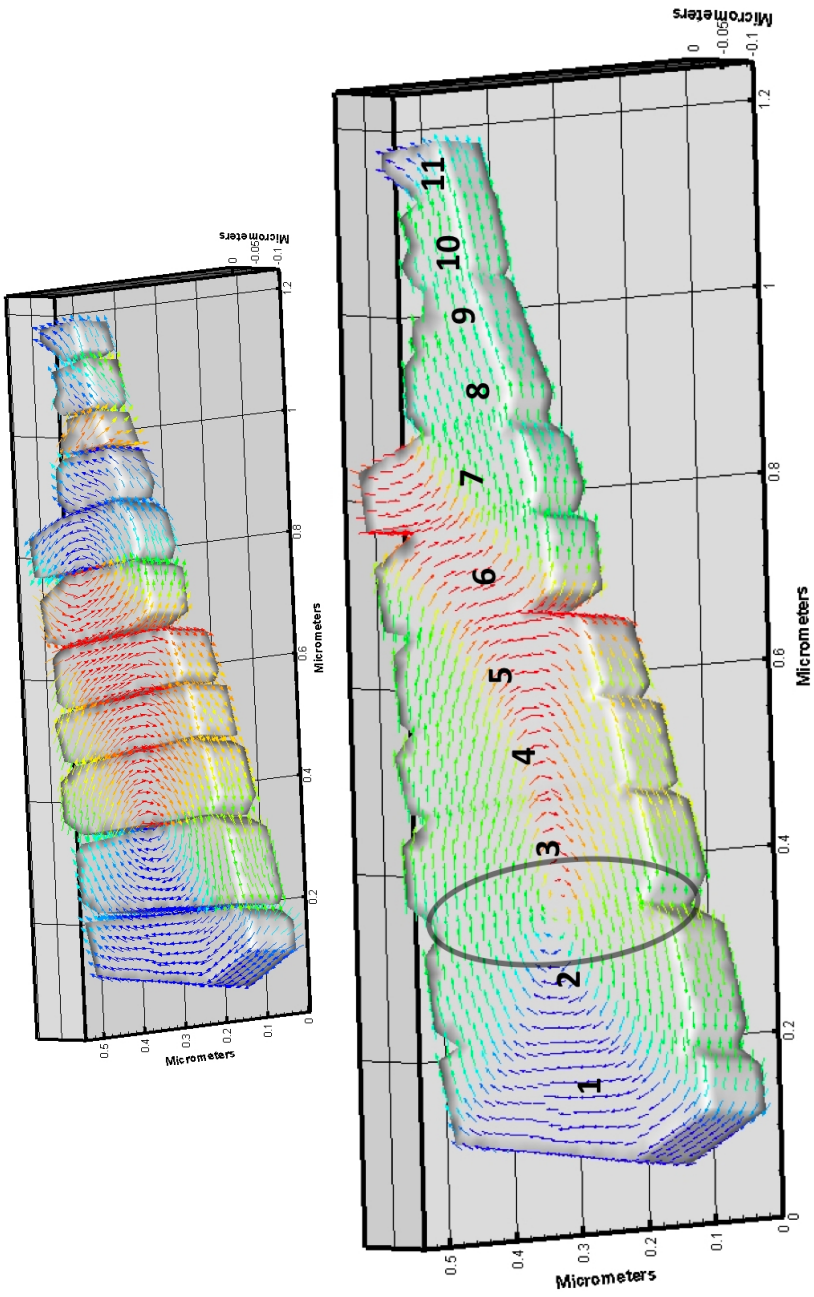

Figure 6.27: The top image is that of the non-bridged system. The bottom image shows the the magnetic structure observed where the boundary nodes have been given material constants that are 0.8× that of magnetite. Lamellae 1 to 5 are very similar to their counterparts within the non-bridged model. However, the vortex structure between lamellae 6 and 7 in the non-bridged model is absent unlike in Figure 6.25 where only the A_{ex} value is altered to 0.8× that of magnetite.

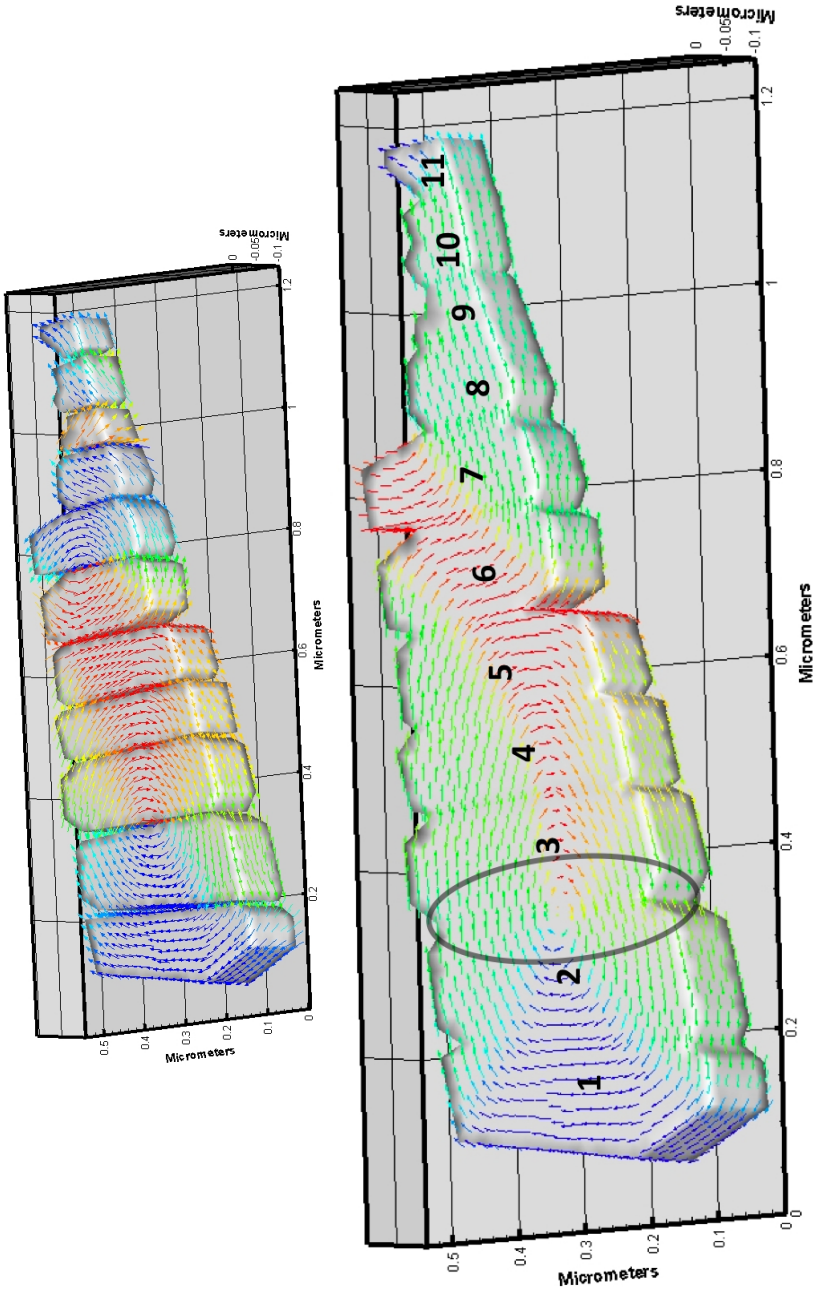

Figure 6.28: The top image is that of the non-bridged system. The bottom image shows the the magnetic structure observed where the boundary nodes have been given material constants that are 1.2× that of magnetite. Lamellae 1 to 5 are very similar to their counterparts within the non-bridged model. However, the vortex structure between lamellae 6 and 7 in the non-bridged model is absent. This shows little change in comparison with the result shown in Figure 6.27 with constants set to 0.8× that of magnetite.

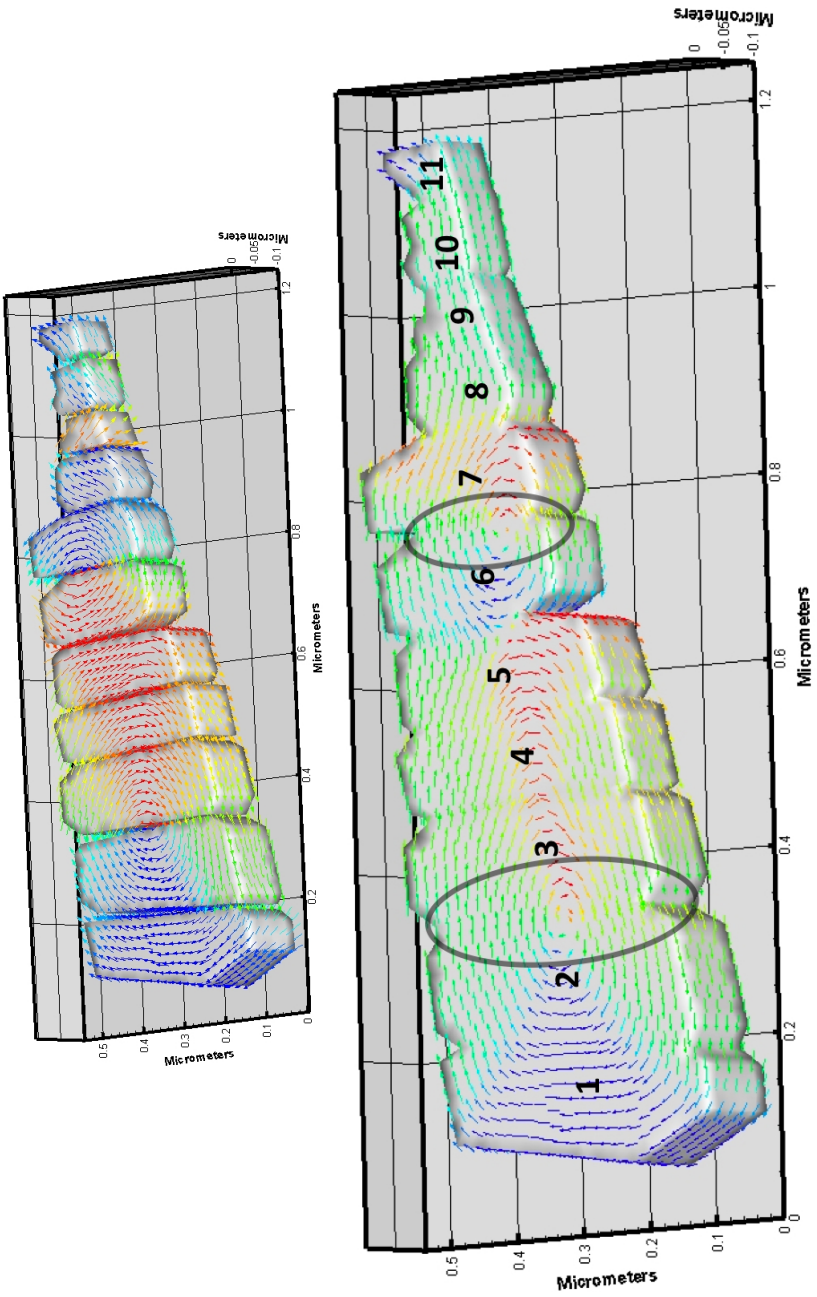

Figure 6.29: The top image is that of the non-bridged system. The bottom image shows the the magnetic structure observed where the boundary nodes have been given material constants that are 1.4× that of magnetite. Lamellae 1 to 5 are very similar to their counterparts within the non-bridged model. However, the vortex structure between lamellae 6 and 7 in the non-bridged model has reappeared, although, as with all the other multiphase structures containing this vortex, the direction is opposite to that seen in the non-bridged model.

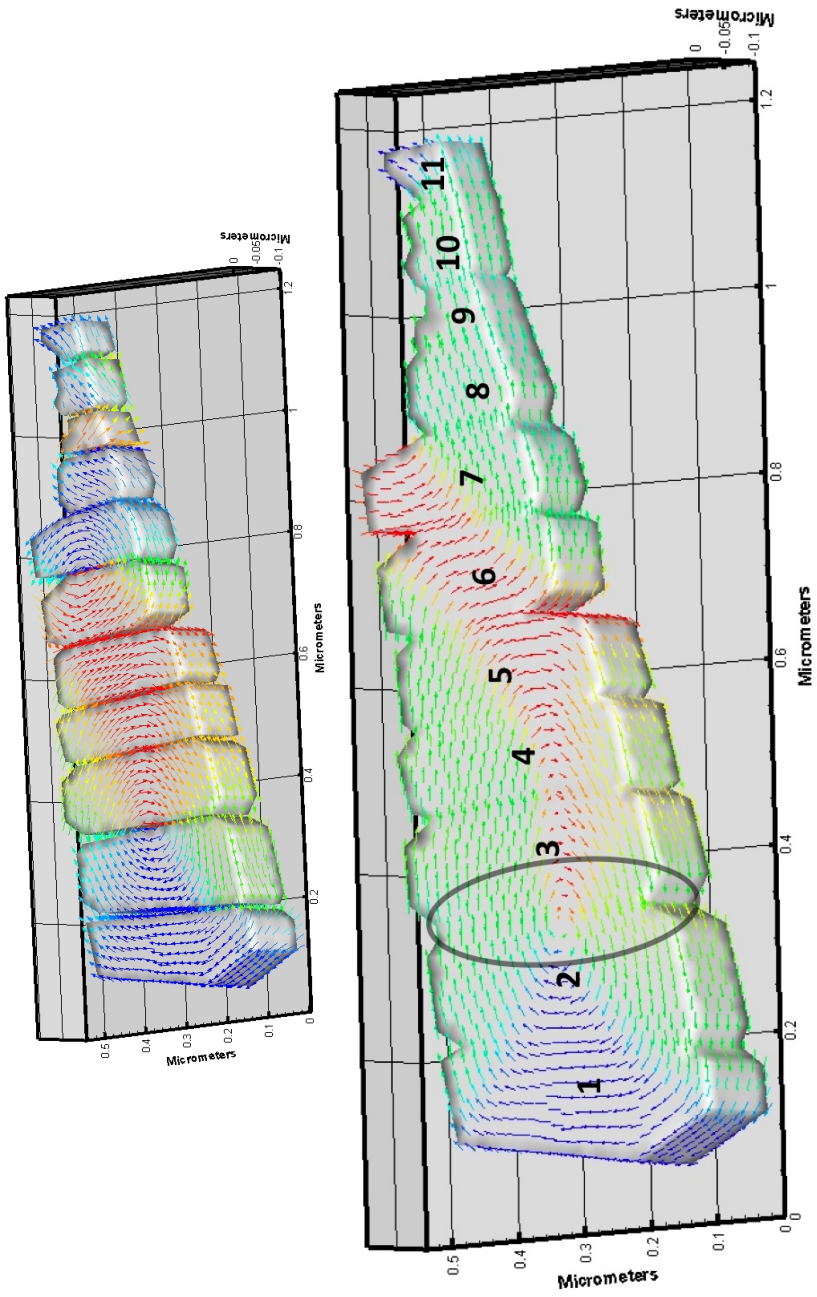

Figure 6.30: The top image is that of the non-bridged system. The bottom image shows the the magnetic structure observed where the boundary nodes have been given material constants that are 1.6× that of magnetite. Lamellae 1 to 5 are very similar to their counterparts within the non-bridged model, although, unlike Figure 6.29, the vortex between lamellae 6 and 7 is once more absent. This system is almost identical to those seen in Figures 6.27 and 6.28.

For those models where all the constants have been altered it was observed that, for the models where the constants take the values of 0.2, 0.4 and 0.6 times that of magnetite, no difference is seen in the magnetic structure and all were identical to the structure shown in Figure 6.27. The overall structure for those models with reduced constants is identical to the results where only the exchange value has been reduced to 0.2 times that of magnetite.

The results where the magnetic constants have been increased show some differences depending on the values used. The result where the magnetic constants are 1.2 times that of magnetite (Figure 6.28) shows an identical structure to the case where the constants are 0.8 times that of magnetite. However, as the constants are increased to 1.4 times that of magnetite (Figure 6.29) we see the emergence of a vortex state between lamellae five and six, this vortex being, as before, in the opposite direction to the direct observations. When the magnetic constants are increased further this vortex structure disappears and once again a structure like that of Figure 6.27 is observed.

6.7 Conclusion

In the multiphase systems including maghemite and TM60 it is important to note that magnetostriction has not been accounted for and, unlike the magnetostriction within magnetite, cannot be considered negligible. In all the multiphase structures a difference is seen between the two phases modelled. In the case of the oxidation system a reduction in the coercivity of the system is observed when the magnetite structure has a skin of varying depth of maghemite applied to it.

In all those models of the irregular structures where the exchange value is increased one would expect to observe an increase in homogeneity, as increasing the exchange increases the interaction required to align the individual spins within a magnetic structure. However, as the magnetite separation is so small (only one element length), it is difficult to see this effect within the areas between the lamellae.

Importantly in all the models of the irregular structure within this chapter vortex states are only ever observed at the boundaries of the lamellae. The one exception to this case is Figure 6.17 where, in lamella one, two further vortex structures are evident.

Chapter 7

Discussion and Conclusions

7.1 Possible improvements to geometry constraint

There are a number of important areas where further study would be necessary in order to make this body of work more productive. Outlined below are some of the main areas that have become apparent.

With respect to Chapter 4, a more detailed construction of the topography of the system would greatly improve the ability to model complicated 3D structures. One method available for doing this is the process of electron tomography. Although electron tomography has been employed since the 1970s, it is only in the last ten years that it has been widely used [Midgley and Dunin-Borkowski (2009)]. This technique allows 3D structures to be generated at the mesoscale, making it ideal to reconstruct structures like those produced as a response to exsolution.

In response to the discussion in Chapter 5, regarding the possibility of a strong connection between the geometry and magnetic structure observed, a further simulation has been run. This new simulation uses a simplified version of the geometry used in Figure 5.14 which showed the full system assumed to be a continuous block of magnetite, this geometry removing some of the sharp angles between

neighbouring lamellae. The results of this simulation have been plotted over the same structure as shown in Figure 5.14 so that the lamellae boundaries are more clearly observed. It can be seen that the position of the large vortex structure seen between lamellae two and three remains consistent, appearing near the edge of the lamellae, but, on the other hand, the vortex between lamellae six and seven has changed position. The vortex which was originally positioned between lamellae six and seven now lies within the centre of lamella six. It is apparent that the topography of the system does affect the magnetic structures observed, and, as mentioned in the previous paragraph, electron tomography would have been of great use in this example as it would have allowed the geometry to be better constrained.

This geometry dependence may also help to explain the transient nature of the previously mentioned vortex state within the figures seen in section 6.7. Within these figures this area of the model is the most susceptible to changes in the material constants which may indicate a more delicate balance between magnetic and geometric processes within the system in this area.

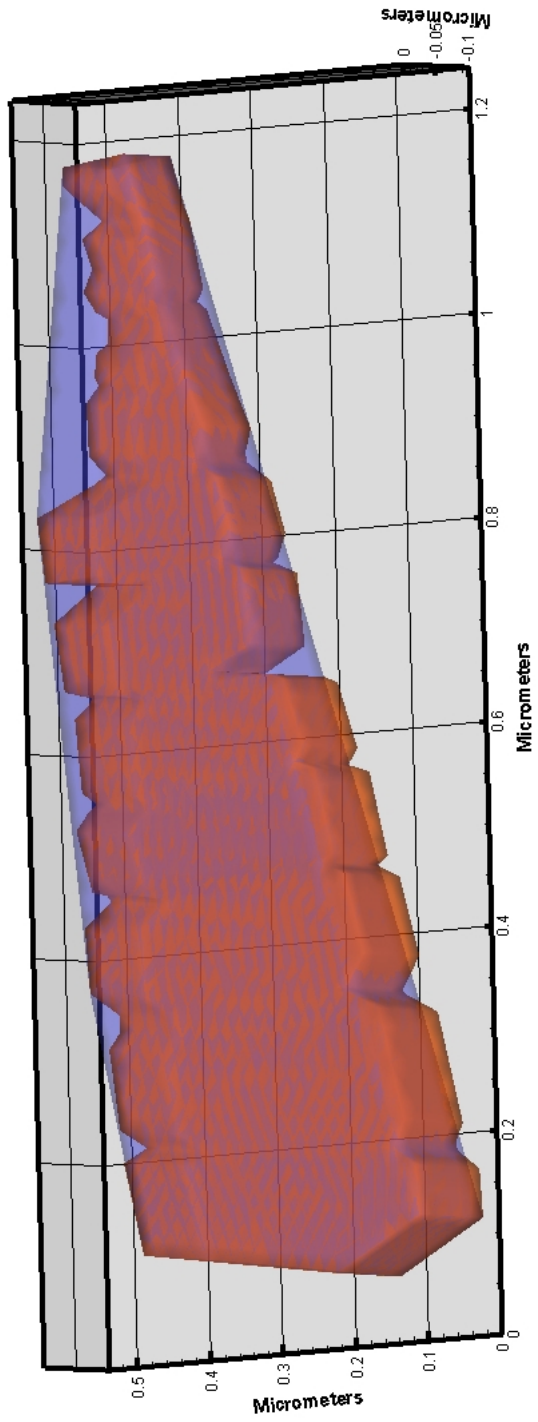

Figure 7.1: Image showing the simplified geometry used to examine the effect of the geometry on the magnetic structure. The red structure indicates the original structure used in Figure 5.14 and the blue structure the new simplified geometry which removes the sharp edges between individual lamellae.

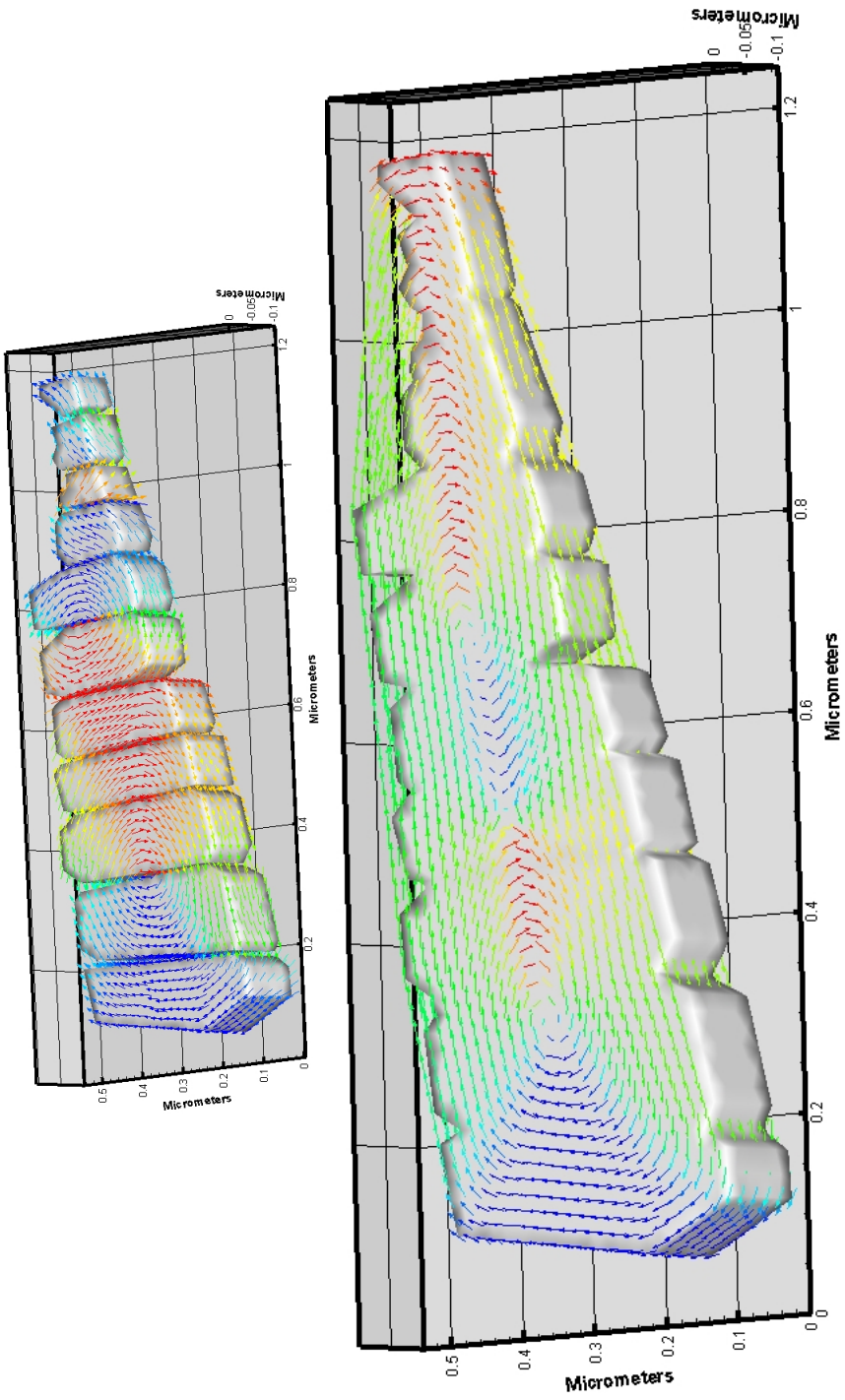

Figure 7.2: Model showing the magnetic structure observed where the geometry in Figure 7.1 is used. This structure overlays the structure seen in Figure 5.14 to allow the positions of the major structures to be compared directly. As can be seen in even in the absence of the sharp corners at the lamellae boundaries the vortex between lamellae 2 and 3 remains unchanged. However the vortex between lamellae 6 and 7 now exists in the body of lamellae 6.

7.2 Factors which have limited the results of this body of work

There are a number of considerations regarding the actual model used within the system:

→ It is important to note that this model does not account for magnetostriction within the system. Magnetostriction within a magnetic system is both a consequence of the chemical structure of the system and also the temperature and pressure of the system. The magnetostriction of magnetite has very little contribution to the overall energy of a small single domain (SD) magnetite system. However, this is not the case for hematite and other materials within this solid solutions.

→ It has been extremely difficult to properly constrain the model. This is due to our presently limited knowledge of magnetic constants. Magnetite is well parameterised as much experimental work has been done on this system. However, other minerals, such as hematite and the non-endmember titanomagnetites, have had far less work done to determine their magnetic properties. This poses a problem for modelling various materials and indeed several different experimental studies for hematite have had results that vary by orders of magnitude.

→ These models are still limited by available CPU power. Although the machines which were being used within this study are extremely powerful, there are still limits on the size of systems that we can successfully model. The full system seen in Figure 3.1 would exceed the memory quota of the machines used within this study.

→ Although the models used the values for magnetite, in most cases the actual system was a titanomagnetite with low Ti content, approximately TM20.

This is because natural and experimentally produced samples are unlikely to be pure endmembers of the solid solutions.

To conclude, the single most important area of improvement would be to incorporate the effect of magnetostriction within the system. This is particularly complicated as it would also alter the magnetocrystalline anisotropy within the system. Although more challenging to do, this addition would constitute an extremely important step towards being able to fully model more complex systems, particularly those systems containing the titanomagnetites and titanohematites where both are affected by magnetostriction.

7.3 Conclusion

7.3.1 Modelling of irregular structures

The application of the micromagnetic model to irregular structures has been exceptionally successful.

→ The model in Figure 5.1, showing the original non-bridged modelled system, closely resembles the direct observations of the system seen in Figure 4.7. Many of the important features observed in the direct observations are also evident in the model; both vortex structures are clear and occupy similar positions to those in the direct observations. On the whole the magnetic structure in the model follows a similar pattern to that seen in the direct observations.

→ In the case of those models in Figures 4.5 and 4.6, where the irregular biogenic magnetite is modelled, the model results fit far better with established theory than the direct observations. Even when the surface of the geometry was altered to try to conform better to the structures seen in Schumann et al. the model results consistently displayed structures more complex than the single domain (SD) structures recorded by Schumann. Magnetite

structures with dimensions similar to those presented in this paper would be expected to be outwith the SD range and, therefore, more similar to those models displayed within this study.

→ Although the models and direct observations in Figures 5.1 and Figure 4.7 correlate well there were some discrepancies. Through those models produced in Chapter 5 it has become clear that all these discrepancies cannot be accounted for purely by geometrical means. This emphasises the need for such systems to be examined using a multiphase approach.

7.3.2 Multiphase modelling

The work discussed in Chapter 3 explores the method by which a multiphase code was produced, with Chapter 6 putting this code into practice for a variety of theoretical and experimental examples.

→ Even using the multiphase code the differences between Figures 5.1 and 4.7 could not be accounted for. However, altering the magnetic properties of the ulvöspinel phase did alter the overall structure for the system. In some areas this multiphase approach matched more closely the direct observations (see section 6.6).

→ This multiphase approach was also used to model a variety of systems containing two magnetic phases in contact. The materials chosen are all materials which are found abundantly within palaeomagnetic studies, and, therefore, are of great importance.

→ Of particular interest are the results from section 6.4 Figures 6.8 to 6.12 examining the effect of altered maghemite shells in simple mock up of he haematite-maghemite oxidation process. These results examine a common magnetic system, albeit using very simple geometries, and clearly emphasise the possibilities of using this model to approach various important magnetic systems in the future.

7.3.3 Closing Remarks

Although singlephase micromagnetic models are hugely useful, those systems which are of most interest within the geosciences are often highly complex systems with multiple magnetic phases in contact. As a consequence of this, multiphase models such as the one generated within this study, capable of modelling irregular structures, are necessary. Particularly in combination with the availability of improved imaging techniques, it is now possible to investigate magnetic systems more fully than ever before.

This model could be extremely useful in examining various processes, such as the oxidation system in Chapter 6, which directly impact and could therefore affect the fidelity of palaeomagnetic samples. The model is particularly useful when examining small SD system, common within palaeomagnetic samples, which are likely to be less effected by magnetostriction. The model will always be limited by our experimental knowledge of magnetic constants, particularly as real samples are unlikely to be pure end member compositions. In these cases approximations will have to be made.

As discussed previously, in section 7.2, this multiphase model is not a complete description of a magnetic system. It is, however, an invaluable starting point to allow the generation of fuller models which can only help to increase our knowledge of these systems which are of such fundamental importance within this field.

Bibliography

Banerjee, S. K. (1971). New grain size limits for palaeomagnetic stability in haematite. *Nature*, 232:15–16.

Barkhausen, H. (1919). Two phenomena, discovered with the help of the new amplifiers. *Phys. Z. Sowjetunion*, 20:401–403.

Bazylinski, D. A., Garratt-Reed, A. J., and Frankel, R. B. (1994). Electron microscopic studies of magnetosomes in magnetotactic bacteria. *Microscopy Research and Technique*, 27(5):389–401.

Blakemore, R. P. (1975). Magnetotactic bacteria. *Science*, 190:377–379.

Bleil, U. (1976). An experimental study of the titanomagnetite solid solution series. *Pure and Applied Geophysics*, 114(2):165–175.

Bødker, F., Hansen, M. F., Koch, C. B., Lefmann, K., and rup, S. (2000). Magnetic properties of hematite nanoparticles. *Physical Review B*, 61(10):6826. Copyright (C) 2011 The American Physical Society Please report any problems to prola@aps.org PRB.

Brown, P. N., Byrne, G. D., and Hindmarsh, A. C. (1989). Vode: a variable-coefficient ode solver. *SIAM J. Sci. Stat. Comput.*, 10(5):1038–1051.

Butler, R. F. and Banerjee, S. K. (1975). Theoretical single-domain size range in magnetite and titanomagnetite. *Journal of Geophysical Research*, 80:4049–4058.

Chevallier, R. and Mathieu, S. (1943). Propri/'et/'es magn/'etiques des poudres d'h/'ematite - influence des dimensions des grains. *Annales Phys.*, 18:258–288.

Cowburn, R. P. (2002). Magnetic nanodots for device applications. *Journal of Magnetism and Magnetic Materials*, 242-245(Part 1):505–511.

Davies, A. (1985). *The Finite Element Method. A First Approach*. Oxford University Press, Oxford.

Deer, Howie, and Zussman (1966). *An Introduction to the Rock Forming Minerals*. Pearson Prentice Hall, Essex, 2 edition.

Doriguetto, A. C., Fernandes, N. G., Persiano, A. I. C., Filho, E. N., Grenche, J. M., and Fabris, J. D. (2003). Characterization of a natural magnetite. *Physics and Chemistry of Minerals*, 30(5):249–255. 10.1007/s00269-003-0310-x.

Dunlop, D. J. (1986). Hysteresis properties of magnetite and their dependence on particle size: A test of pseudo-single-domain remanence models. *J. Geophys. Res.*, 91(B9):9569–9584.

Dunlop, D. J. and Ozdemir, O. (1997). *Rock Magnetism Fundamentals and Frontiers*, volume 3 of *Cambridge Studies in Magnetism*. Cambridge University Press, 2 edition.

Enkin, R. J. and Dunlop, D. J. (1987). A micromagnetic study of pseudo single-domain remanence in magnetite. *J. Geophys. Res.*, 92(B12):12726–12740.

Enkin, R. J. and Williams, W. (1994). Three-dimensional micromagnetic analysis of stability in fine magnetic grains. *J. Geophys. Res.*, 99(B1):611–618.

Evans, M. E. and Heller, F. (2003). *Environmental Magnetism*, volume 86 of *International Geophysics Series*. Academic Press, 1 edition.

Evans, M. E., Krása, D., Williams, W., and Winklhofer, M. (2006). Magnetostatic interactions in a natural magnetite-ulv'ospinel system. *J. Geophys. Res.*, 111(B12S16).

Evans, M. E. and Wayman, M. L. (1970). An investigation of small magnetic particles by means of electron microscopy. *Earth and Planetary Science Letters*, 9(4):365–370.

Evans, M. E. and Wayman, M. L. (1974). An investigation of the role of ultra-fine titanomagnetite intergrowths in palaeomagnetism. *Geophysical Journal of the Royal Astronomical Society*, 36(1):1–10.

Feinberg, J., Scott, G., Renne, P., and Wenk, H. (2005). Exsolved magnetite inclusions in silicates: Features determining their remance behaviour. *Geology*, (33):513–516.

Feinberg, J. M., Harrison, R. J., Kasama, T., Dunin-Borkowski, R. E., Scott, G. R., and Renne, P. R. (2006). Effects of internal mineral structures on the magnetic remanence of silicate-hosted titanomagnetite inclusions: An electron holography study. *J. Geophys. Res.*, 111(B12):B12S15.

Fidler, J. and Schrefl, T. (2000). Micromagnetic modelling - the current state of the art. *Journal of Physics D: Applied Physics*, 33(15):R135.

Fukunaga, K., Kuma, J., and Kanai, Y. (1999). Effect of strength of intergrain exchange interaction on magnetic properties of nanocomposite magnets. *Magnetics, IEEE Transactions on*, 35(5):3235–3240. 0018-9464.

Hamblin, W. K. and Christiansen, E. H. (1995). *Earth's Dynamic Systems*. Prentice Hall, 7 edition.

Harrison, R. J., Dunin-Borkowski, R. E., and Putnis, A. (2002). Direct imaging of nanoscale magnetic interactions in minerals. *PNAS*, 99(26):16556–16561.

Harrison, R. J. and Putnis, A. (1998). The magnetic properties and crystal chemistry of oxide spinel solid solutions. *Surveys in Geophysics*, 19(6):461–520. 10.1023/A:1006535023784.

Heider, F., Dunlop, D. J., and Sugiura, N. (1987). Magnetic properties of hydrothermally recrystallized magnetite crystals. *Science*, 236(4806):1287–1290. 10.1126/science.236.4806.1287.

Heider, F. and Williams, W. (1988). Note on temperature dependence of exchange constant in magnetite. *Geophys. Res. Lett.*, 15.

Hubert, A. and Schafer, R. (1998). *Magnetic Domains The Analysis of Magnetic Microstructures*. Springer.

Hunt, C. P., Moskowitz, B. M., and Banerjee, S. K. (1995). Magnetic properties of rocks and minerals. *American Geophysical Reviews*.

John, W. C. (1965). Phase separation by spinodal decomposition in isotropic systems. *The Journal of Chemical Physics*, 42(1):93–99.

Kirschvink, J. L., Douglas, S. J., and MacFadden, B. J. (1985). *Magnetite Biomineralization and Magnetoreception in Organisms*. Topics in Geobiology. Plenum Press.

Kittel, C. (1949a). On the gyromagnetic ratio and spectroscopic splitting factor of ferromagnetic substances. *Physical Review*, 76(6):743. Copyright (C) 2007 The American Physical Society Please report any problems to prola@aps.org PR.

Kittel, C. (1949b). Physical theory of ferromagnetic domains. *Reviews of Modern Physics*, 21(4):541. Copyright (C) 2007 The American Physical Society Please report any problems to prola@aps.org RMP.

Kittel, C. and Abrahams, E. (1953). Relaxation process in ferromagnetism. *Reviews of Modern Physics*, 25(1):233. Copyright (C) 2007 The American Physical Society Please report any problems to prola@aps.org RMP.

Krása, D. and Matzka, J. (2007). Inversion of titanomaghemite in oceanic basalt during heating. *Physics of The Earth and Planetary Interiors*, 160(2):169–179.

Landau, L. D. and Lifshitz, E. M. (1935). Collected papers of l.d. landau. *Phys. Z. Sowjetunion*, 8(153):101.

Lepp, H. (1957). Stages in the oxidation of magnetite. *American Mineralogist*, 42:679–683.

Levi, S. and Merrill, R. (1978). Properties of single-domains, pseudo-single-domain and multi-domain magnetite. *J. Geophys. Res.*, 83:309–323.

Li, C. W., Chin, J. S., and Huang, S. H. (1989). Growth of chiton teeth evidenced from magnetic measurements and microstructure characerisation. *IEEE Transactions on Magnetics*, 25(5):3818–3820.

Lowenstam, H. A. (1962). Magnetite in dentical capping in recent chitons (polyplacophora). *Geological Society of America*, 73:435–438.

Maier, G. and Polizzotto, C. (1987). A galerkin approach to boundary element elastoplastic analysis. *Computer Methods in Applied Mechanics and Engineering*, 60(2):175–194.

Midgley, P. (2001). An introduction to off-axis electron holography. *Micron*, (32).

Midgley, P. and Dunin-Borkowski, R. (2009). Electron tomography and holography in materials science. *Nature Materials*, 8:271–280.

Morrish, A. H. and Yu, S. P. (1955). Dependence of the coercive force on the density of some iron oxide powder. *Journal of Applied Physics*, 26(8):1049–1055.

Myers, H. (2002). *Introductory Solid State Physics*. CRC Press, 2 edition.

Neel, L. (1949). Theorie du trainage magnetique des ferromagnetiques en grains fins avec applications aux terres cuites. *Annales de Geophysique*, 5(2):99 –135.

Neel, L. (1955). Some theoretical aspects of rock magnetism. *Advances in Physics*, 4:191–241.

Özdemir, O., Dunlop, D. J., and Berqu/'u, T. S. (2008). Morin transition in hematite: Size dependence and thermal hysteresis. *Geochem. Geophys. Geosyst.*, 9(10):Q10Z01.

Petersen, N., von Dobeneck, T., and Vali, H. (1986). Fossil bacterial magnetite in deep-sea sediments from the south atlantic ocean. *Nature*, 320(6063):611–615. 10.1038/320611a0.

Petrovský, E., Kropáček, V., Dekkers, M. J., deBoer, C., Hoffmann, V., and Ambatiello, A. (1996). Transformation of hematite to maghemite as observed by changes in magnetic parameters: Effects of mechanical activation? *Geophys. Res. Lett.*, 23.

Price, G. D. (1980). Exsolution microstructures in titanomagnetites and their magnetic significance. *Physics of The Earth and Planetary Interiors*, 23(1):2–12.

Ramesh, R., Thomas, G., and Ma, B. M. (1988). Magnetization reversal in nucleation controlled magnets. ii. effect of grain size and size distribution on intrinsic coercivity of fe-nd-b magnets. *Journal of Applied Physics*, 64(11):6416–6423.

Scholz, W. (2003). *Scalable Parallel Micromagnetic Solvers for Magnetic Nanostructures*. PhD thesis.

Schumann, D., Raub, T. D., Kopp, R. E., Guerquin-Kern, J.-L., Wu, T.-D., Rouiller, I., Smirnov, A. V., Sears, S. K., Lcken, U., Tikoo, S. M., Hesse, R., Kirschvink, J. L., and Vali, H. (2008). Gigantism in unique biogenic magnetite at the paleoceneeocene thermal maximum. *Proceedings of the National Academy of Sciences*, 105(46):17648–17653.

Smith, P. P. K. (1980). Spinodal decomposition in a titanomagnetite. *American Mineralogist*, 65:1038–1043.

Soffel, H. (1971). The single-domain-multidomain transition in natural intermediate titanomagnetites. *Zeitschrift fuer Geophysik*, 37:451–470.

Szmaja, W. and Balcerski, J. (2002). Domain investigation by the conventional bitter pattern technique with digital image processing. *Czechoslovak Journal of Physics*, 52(2):223–226–226.

Thomson, L. C., Enkin, R. J., and Williams, W. (1994). Simulated annealing of three-dimensional micromagnetic structures and simulated thermoremanent magnetization. *J. Geophys. Res.*, 99(B1):603–609.

Tonomura, A., Matsuda, T., Endo, J., Arii, T., and Mihama, K. (1986). Holographic interference electron microscopy for determining specimen magnetic structure and thickness distribution. *Physical Review B*, 34(5):3397. Copyright (C) 2008 The American Physical Society Please report any problems to prola@aps.org PRB.

Wang, D. and Van der Voo, R. (2004). The hysteresis properties of multidomain magnetite and titanomagnetite/titanohematite in mid-ocean ridge basalts. *Planetry Science Letters*, 220:175–184.

Williams, W. and Dunlop, D. J. (1989). Three-dimensional micromagnetic modelling of ferromagnetic domain structure. *Nature*, 337(6208):634–637. 10.1038/337634a0 10.1038/337634a0.

Williams, W., Evans, M. E., and Krsa, D. (2010). Micromagnetics of paleomagnetically significant mineral grains with complex morphology. *Geochem. Geophys. Geosyst.*, 11(2):Q02Z14.

Young, H. and Freedman, R. (1996). *University Physics*. Addison Wesley, 10 edition.

Zienkiewicz, O. and Taylor, R. (2000). *The finite element method*, volume 1. Butterworth-Heinemann, Oxford, 5 edition.

Appendix A

Shape functions

This appendix examines the shape functions for the triangular and tetrahedral elements within the system. Initially, the task is to examine a one dimensional case where we have an arbitrary point P existing somewhere on a line. The aim of this exercise is to be able to define the position of P relative to the end points of the line, or nodes, of this one dimensional element. Two vectors, L_1 and L_2, can be defined which can be described as the local coordinates of this system. These coordinates can define the position of P relative to each node. This process can also be applied at a two dimensional level. To do this we must first consider a two dimensional finite element like that seen in Figure A.1.

To express the position of point P relative to the vertex positions of the element, we use a set of local coordinates L_1, L_2 and L_3 where these local coordinates can be defined as follows:

$$L_1 = \frac{A_1}{A} \tag{A.1}$$

$$L_2 = \frac{A_2}{A} \tag{A.2}$$

$$L_3 = \frac{A_3}{A} \tag{A.3}$$

$$\therefore L_1 + L_2 + L_3 = \frac{A_1 + A_2 + A_3}{A} = 1 \tag{A.4}$$

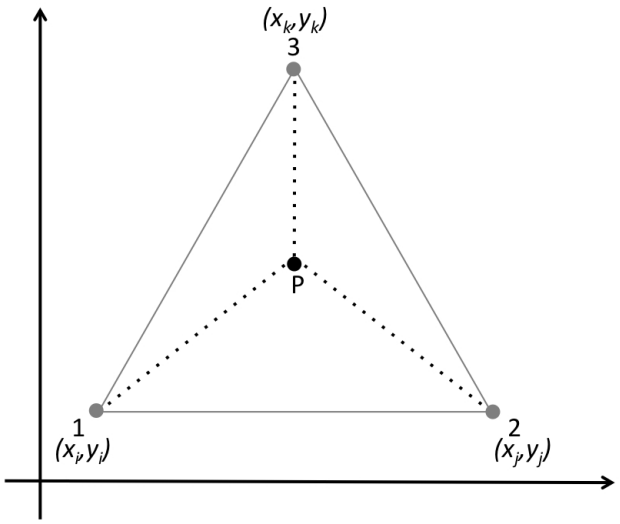

Figure A.1: Here we have triangular element 123 containing a point P, the dashed lines indicating the three areas P12, P23 and P13

In this example A is the area of the entire triangular element and A_i is the area of the triangular section constructed from points Pij, where i and j denote the node numbers where $i \neq j$. These local coordinates are both interpolatory and linearly dependent, that is, the individual vectors in a finite set of vectors can be written as a linear combination of the other vectors in the set. We can therefore state that the area of the element is simply the summation of A_1, A_2 and A_3. If we then express this area in terms of the global coordinate system, not using the local coordinates, but the cartesian system within which this element exists, we obtain the following expression:

$$A = A_1 + A_2 + A_3 \text{ where } A = 0.5 \begin{bmatrix} 1 & x_i & y_i \\ 1 & x_j & y_j \\ 1 & x_k & y_k \end{bmatrix} \tag{A.5}$$

We assume that the function ϕ^e is linear throughout this element, therefore it holds that

$$\phi^e(x, y) = a_0 + a_1 x + a_2 y \tag{A.6}$$

We will express the function in terms of the nodal coordinates of the element which can be constructed from cross referencing the element array with the corresponding element coordinates. The nodal values ϕ_i, ϕ_j, ϕ_k are therefore used in conjunction with the basis vectors L_1, L_2, L_3 where the coordinates x, y can be expressed in terms of these vectors.

$$\begin{aligned} x &= L_1 x_i + L_2 x_j + L_3 x_k \\ y &= L_1 y_i + L_2 y_j + L_3 y_k \end{aligned} \tag{A.7}$$

This can be solved by using the condition $L_1 + L_2 + L_3 = 1$ from equation A.4, allowing us to express our local coordinates as follows:

$$\begin{aligned} L_1 &= (a_i + b_i x + c_i y)\tfrac{1}{2}A \\ L_2 &= (a_j + b_j x + c_j y)\tfrac{1}{2}A \\ L_3 &= (a_k + b_k x + c_k y)\tfrac{1}{2}A \\ \implies & [(a_i + b_i x + c_i y) + (a_j + b_j x + c_j y) + (a_k + b_k x + c_k y)]\tfrac{1}{2} = 1 \end{aligned} \tag{A.8}$$

This can be expressed in a generalised form (equation A.9).

$$L_n = (a_n + b_n x + c_n y)\frac{1}{2} \tag{A.9}$$

The functional can therefore be represented using the shape matrix such that

$$\begin{aligned} \phi^e &= N^e \delta^e \\ \phi^e &= [L_1 L_2 L_3] \cdot \begin{bmatrix} \phi_1 \\ \phi_2 \\ \phi_3 \end{bmatrix} \end{aligned} \tag{A.10}$$

$$\therefore \text{ stiffness matrix } k_{ij} = \iint_A \left(\frac{\partial L_1}{\partial x} \cdot \frac{\partial L_2}{\partial x} + \frac{\partial L_1}{\partial y} \cdot \frac{\partial L_2}{\partial y} \right) dxdy \quad \text{(A.11)}$$

$$= \iint_A \left(\frac{b_i b_j}{4A^2} + \frac{c_i c_j}{4A^2} \right) dxdy \quad \text{(A.12)}$$

$$= \frac{1}{4} A(b_i b_j + c_i c_j) \quad \text{(A.13)}$$

Furthermore this methodology can be applied to a three dimensional system in a similar manner if we take a tetrahedral element as shown in figure B.2.

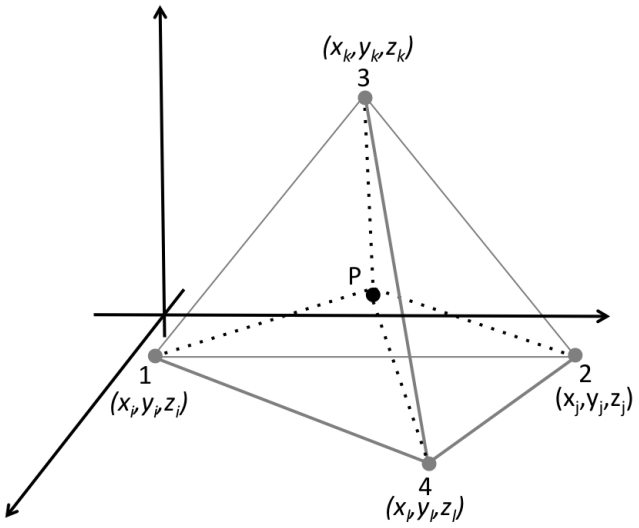

Figure A.2: Here we have tetrahedral element 1234 containing a point P. The dotted lines plot out the different volumes contained in the system; P134, P234, P123 and P124.

In this case the expression in equation A.4 still holds although there is a dimensional change, so instead of areas the tetrahedral is now split into four different volumes as seen in figure B.2 using point P as one of the vertices. As equation A.4 still hold we can, in similar fashion, obtain an expression for the generalised form (equation A.14) where V is the overall volume of the element.

$$L_i = (a_i + b_i x + c_i y + d_i z)/6V \quad \text{(A.14)}$$

The values a_i, b_i, c_i and d_i can be expressed as seen in equation A.15 where

the node coordinates of the tetrahedral are defined as (x_i, y_i, z_i), (x_j, y_j, z_j) , (x_k, y_k, z_k) and (x_l, y_l, z_l)

$$a_i = \begin{vmatrix} x_j & y_j & z_j \\ x_k & y_k & z_k \\ x_l & y_l & z_l \end{vmatrix} \quad b_i = -\begin{vmatrix} 1 & y_j & z_j \\ 1 & y_k & z_k \\ 1 & y_l & z_l \end{vmatrix} \quad c_i = -\begin{vmatrix} x_j & 1 & z_j \\ x_k & 1 & z_k \\ x_l & 1 & z_l \end{vmatrix} \quad d_i = -\begin{vmatrix} x_j & y_j & 1 \\ x_k & y_k & 1 \\ x_l & y_l & 1 \end{vmatrix} \tag{A.15}$$

Again, as in the two dimensional case, we can also define the stiffness matrix of the system for a tetrahedral element (equation A.16) using the definition of the N_e as seen previously in equation A.10 where on this occasion we have a triple integral over the volume element volume V.

$$k_{ij}^e = \iiint_V \left(\frac{\partial N_i^e}{\partial x} \cdot \frac{\partial N_j^e}{\partial x} + \frac{\partial N_i^e}{\partial y} \cdot \frac{\partial N_j^e}{\partial y} + \frac{\partial N_i^e}{\partial z} \cdot \frac{\partial N_j^e}{\partial z} + \right) dx\, dy\, dz \tag{A.16}$$

This method of defining a point within a simplex, of any dimension, gives rise to a generalised barycentric coordinate system to define the point.

Appendix B

Constants File

B.1 Introduction

This appendix contains examples of constants files used within this project. These files contain all the necessary information required for the micromagnetic model, including both material information and also inputs for the library functions. An example of an input used for both the single and multiphase micromagnetic model is displayed in this appendix.

B.2 Single phase constants file

All input files are named $<$ *stem* $>$.consts and correspond with the geometry file, $<$ *stem* $>$.pat or $<$ *stem* $>$.mesh depending on the file format used. The red box in Figure B.1 contains all the information used to supply the magnetic information for the model. The first input line supplies the material properties $A_e x$, M_s and K_1. Also supplied in this first input line are the values used for the time step within the solver (DeltaT), the length scale (ls) and the constant μ_0 (mu).

Within this study the eighth input line regarding the choice of the solving method is always set to c̈ombined:̈ This indicates that both the energy minimi-

sation and dvode(LLG) solver are used. the alternative options are euler and heuner solvers which are never used within this study.

The DVODE parameters on input line 9 are explained in the comments on pages 153 to 155. These parameters remained consistent throughout this study and take the values shown in this example constants file.

```
# A      Ms    K1    DeltaT  ls   mu
1.34d-11 4.8d5 -1.24d4 8.d-4 1.0d6 1.d-7
# initial time
0.0d0
# gilbert damping constant
1.0d0
# uniaxial easy axis
0.d0 1.0 0.0
# externally applied field start finish reduction step (T or Oe)
0.0d-3 0.0d-3 5.0d-3
# externally applied field direction
1.0d0 0.0 .01
# anisotropy form cubic or uni
cubic
# choice of solver energymin, euler,heun or dvode or combined
combined
# dvode parameters MF,JACFLG,JPRE,MAXORD
21 0 1 5
# the initial magnetization direction x,y,z,flag. Not set if flag=0.0
0.26 -1.0 1.73  -99.0
# nextr line set =1 to start from file , =0  initial guess set using above
0
# next line gives rotation of cubic anisot axis a=35.25 rot about y, b=45, abo
ut z
0.0d0, 0.0d0
35.2643d0, 45.0d0


-246.d0 43.0d0 0.0d0


#1.d-1 0.0 2.0
#cgs
1.34d-6 4.8d2 1.24d5 8.d-3 1.d4 1.d0
#SI
1.34d-11 4.8d5 1.24d4 8.d-3 1.d6 1.d-7

#cgs
1.3d-6 8.0d2 0.0d0 1.d-4 1.d4 1.d0
#SI
1.3d-11 8.0d5 0.0d0 1.d-4 1.d6 1.d-7


C DVODEPK NOTES
C MF     = The method flag.  Used only for input.  The legal values of
C          MF are 10, 11, 19, 20, 21, 29 .
C          MF is a two-digit integer, MF = 10*METH + MITER .
C          METH indicates the basic linear multistep method:
C            METH = 1 means the implicit Adams method.
C            METH = 2 means the method based on backward
C                     differentiation formulas (BDF-s).
C          MITER indicates the corrector iteration method.  Currently,
C            the values of MITER have the following meanings:
C
C          0 means functional iteration is used (no Jacobian matrix
C            is involved).
C
C          1 means SPIGMR, a scaled, preconditioned, incomplete version
C            of GMRES, a generalized minimum residual method, is used.
C            This is the best choice in general.
C
```

```
C          9 means that only a user-supplied matrix P (approximating A)
C            will be used, with no Krylov iteration done internally to
C            DVODPK.  This option allows the user to provide the
C            complete linear system solution algorithm, if desired.
C
C If the problem is nonstiff use method flag MF = 10.  If it is stiff, MF shou
ld be 21.
C
C The following four parameters must also be set.
C  DIWORK(1) = LWP  = length of real array WP for preconditioning.
C  DIWORK(2) = LIWP = length of integer array IWP for preconditioning.
C  DIWORK(3) = JPRE = preconditioner type flag:
C                   = 0 for no preconditioning (P1 = P2 = I)
C                   = 1 for left-only preconditioning (P2 = I)
C                   = 2 for right-only preconditioning (P1 = I)
C                   = 3 for two-sided preconditioning
C  DIWORK(4) = JACFLG = flag for whether JAC is called.
C                     = 0 if JAC is not to be called,
C                     = 1 if JAC is to be called.
C  Use JACFLG = 1 if JAC computes any nonconstant data for use in
C  preconditioning, such as Jacobian elements.  See next paragraph.
C  The arrays WP and IWP are work arrays under the user's control,
C  for use in the routines that perform preconditioning operations.
C
C NAME    LOCATION      MEANING AND DEFAULT VALUE
C
C H0      RWORK(5)  The step size to be attempted on the first step.
C                   The default value is determined by the solver.
C
C HMAX    RWORK(6)  The maximum absolute step size allowed.
C                   The default value is infinite.
C
C HMIN    RWORK(7)  The minimum absolute step size allowed.
C                   The default value is 0.  (This lower bound is not
C                   enforced on the final step before reaching TCRIT
C                   when ITASK = 4 or 5.)
C
C DELT    RWORK(8)  Convergence test constant used in Krylov iteration
C                   algorithm.  The default value is 0.05.
C
C MAXORD  IWORK(5)  The maximum order to be allowed.  The default
C                   value is 12 if METH = 1, and 5 if METH = 2.
C                   If MAXORD exceeds the default value, it will
C                   be reduced to the default value.
C                   If MAXORD is changed during the problem, it may
C                   cause the current order to be reduced.
C
C MXSTEP  IWORK(6)  Maximum number of (internally defined) steps
C                   allowed during one call to the solver.
C                   The default value is 500.
C
C MXHNIL  IWORK(7)  Maximum number of messages printed (per problem)
C                   warning that T + H = T on a step (H = step size).
C                   This must be positive to result in a non-default
C                   value.  The default value is 10.
C
C MAXL    IWORK(8)  maximum number of iterations in the SPIGMR
C                   algorithm (.le. NEQ).  The default is
C                   MAXL = min(5, NEQ).
C
C KMP     IWORK(9)  number of vectors on which orthogonalization
C                   is done in the SPIGMR algorithm (.le. MAXL).
C                   The default is KMP = MAXL (complete GMRES method).
```

```
C                  See Ref. 2 for details on incomplete GMRES.
C                  Note:  When KMP .lt. MAXL and MITER = 1, the length
C                  of RWORK must be set accordingly.  See RWORK above.
C-----------------------------------------------------------------------
C Optional Outputs.
C
C As optional additional output from DVODPK, the variables listed
C below are quantities related to the performance of DVODPK
C which are available to the user.  These are communicated by way of
C the work arrays, but also have internal mnemonic names as shown.
C Except where stated otherwise, all of this output is defined
C on any successful return from DVODPK, and on any return with
C ISTATE = -1, -2, -4, -5, -6, or -7.  On an illegal input return
C (ISTATE = -3), they will be unchanged from their existing values
C (if any), except possibly for TOLSF, LENRW, and LENIW.
C On any error return, output relevant to the error will be defined,
C as noted below.
C
C NAME    LOCATION      MEANING
C
C HU      RWORK(11) The step size in t last used (successfully).
C
C HCUR    RWORK(12) The step size to be attempted on the next step.
C
C TCUR    RWORK(13) The current value of the independent variable
C                   which the solver has actually reached, i.e. the
C                   current internal mesh point in t.  In the output,
C                   TCUR will always be at least as far from the
C                   initial value of t as the current argument T,
C                   but may be farther (if interpolation was done).
C
C TOLSF   RWORK(14) A tolerance scale factor, greater than 1.0,
C                   computed when a request for too much accuracy was
C                   detected (ISTATE = -3 if detected at the start of
C                   the problem, ISTATE = -2 otherwise).  If ITOL is
C                   left unaltered but RTOL and ATOL are uniformly
C                   scaled up by a factor of TOLSF for the next call,
C                   then the solver is deemed likely to succeed.
C                   (The user may also ignore TOLSF and alter the
C                   tolerance parameters in any other way appropriate.)
C
C NST     IWORK(11) The number of steps taken for the problem so far.
C
C NFE     IWORK(12) The number of f evaluations for the problem so far.
C
C NPE     IWORK(13) The number of preconditioner evaluations (JAC calls)
C                   so far.
C
C NQU     IWORK(14) The method order last used (successfully).
C
C NQCUR   IWORK(15) The order to be attempted on the next step.
C
C IMXER   IWORK(16) The index of the component of largest magnitude in
C                   the weighted local error vector ( e(i)/EWT(i) ),
C                   on an error return with ISTATE = -4 or -5.
C
C LENRW   IWORK(17) The length of RWORK actually required.
C                   This is defined on normal returns and on an illegal
C                   input return for insufficient storage.
C
C LENIW   IWORK(18) The length of IWORK actually required.
C                   This is defined on normal returns and on an illegal
C                   input return for insufficient storage.
```

```
C
C NNI     IWORK(20) The number of nonlinear iterations so far (each of
C                   which calls the Krylov iterative linear solver).
C
C NCFN    IWORK(21) The number of convergence failures of the nonlinear
C                   (Newton) iteration so far.
C                   Note: A measure of success is the overall rate of
C                   nonlinear convergence failures, NCFN/NST.
C
C NETF    IWORK(22) The number of error test failures of the integrator
C                   so far.
C
C NLI     IWORK(23) The number of linear iterations so far.
C                   Note: a measure of the success of SPIGMR algorithm
C                   is the average number of linear iterations per
C                   nonlinear iteration, given by NLI/NNI.
C                   If this is close to MAXL, MAXL may be too small.
C
C NPS     IWORK(24) The number of preconditioning solve operations
C                   (PSOL calls) so far.
C
C NCFL    IWORK(25) The number of convergence failures of the linear
C                   iteration so far.
C                   Note: A measure of success is the overall rate of
C                   linear convergence failures, NCFL/NNI.
```

Figure B.1: This is an example of a single phase constants file. The information in the red box is the information directly relating to the material properties of the system. The line starting with describes the properties being input on the proceeding line.

B.3 Multiphase constants file

This section gives an example of an input file used for the multiphase version of the micromagnetic model. In this example only the information corresponding to that observed in the red box in Figure B.1 is shown as this is the only part of the file unique to the multiphase constant file.

As can be observed in Figure B.2, there is a second input line for all the material constants, the uniaxial easy axis, anisotropy form and the rotation of the anisotropy axis. The first line in those double line inputs is always attributed to material 1 and the second line to material 2.

In addition to the double inputs are two further inputs. The first of these new inputs is the file format flag where the flag indicates the method by which the geometry file will be read into the model. Both patran and genesis file formats are supported. However, the genesis files must be unwrapped using netcdf libraries so that the data is in an ASCII format. The second additional input line is that of the hard axis. this is not an input that was used and was added for the purpose of haematite.

```
#Mesh file format flag 0  for .mesh 1 for.pat
1
# A      Ms    K1    DeltaT  ls   mu
1.34d-11 4.8d5 1.24d4 8.d-3 1.d6 1.d-7
5.36d-12 3.8d5 -4.65d3 8.d-4 1.0d6 1.d-7
# initial time
0.0d0
# gilbert damping constant
1.0d0
# uniaxial easy axis
1.d0 1.0 1.0
1.d0 1.0 1.0
#hard axis
0.0d0 0.0d0 1.0d0
0.0d0 0.0d0 1.0d0
# externally applied field start finish reduction step (T or Oe)
0.0d0 -0.0d0 0.5d0
# externally applied field direction
1d0 1 1
# anisotropy form cubic or uni
cub
cub
# choice of solver energymin, euler,heun or dvode or combined
combined
# dvode parameters MF,JACFLG,JPRE,MAXORD
21 0 1 5
# the initial magnetization direction x,y,z,flag. Not set if flag=0.0
1.0 0.0 0.0  -99.0
# nextr line set =1 to start from file , =0  initial guess set using above
0
# next line gives rotation of cubic anisot axis a=35.26 rot about y, b=0, abou
t z, c=-45, about x
0.0d0, 0.0d0, 0.0d0
0.0d0, 0.0d0, 0.0d0
```

Figure B.2: This is an example of a multiphase constants file. The information included is proportional to the information in the red box in Figure B.1B.1.

Appendix C

Additional Results

C.1 Magnetite - Haematite system

C.1.1 Introduction

This appendix contains some results of an additional sample seen in Figure C.1. This sample contains magnetite and haematite intergrowths and was constructed and imaged by Nathan Church of the University of Cambridge. The compositions of the intergrowths are not the end members but instead some similar intermediate compositions of the system, the actual compositions being titanomagnetite regions TM09 ($Fe_{2.91}Ti_{0.09}O_4$) and haematite regions hem50 ($Fe_{1.5}Ti_{0.5}O_3$). The exchange and anisotropy therefore differ from those of pure haematite and magnetite. In relation to anisotropy the [001] of the haematite phase and the [111] of the magnetite phase are coexistent due to the exsolution process which produced them. The sample has an approximate thickness of 100-120 nm.

Unfortunately for several reasons this work could not be expanded further. Firstly, as the compositions are not those of the end members, approximations had to be made and as such the TM09 phase was assumed to be magnetite. The main difficulty within the models was the haematite phase, as due to the nature of the anisotropy system the cubic structure already used within the model was not able to be used. Although attempts were made to model haematite this coding

was unsuccessful. A further complication was that the individual structures in this sample were poorly defined and were on the cusp of what could be realistically modelled using a micromagnetic code. Due to this all the models use only those lamellae marked 1, 3 and 5 in Figure C.1.

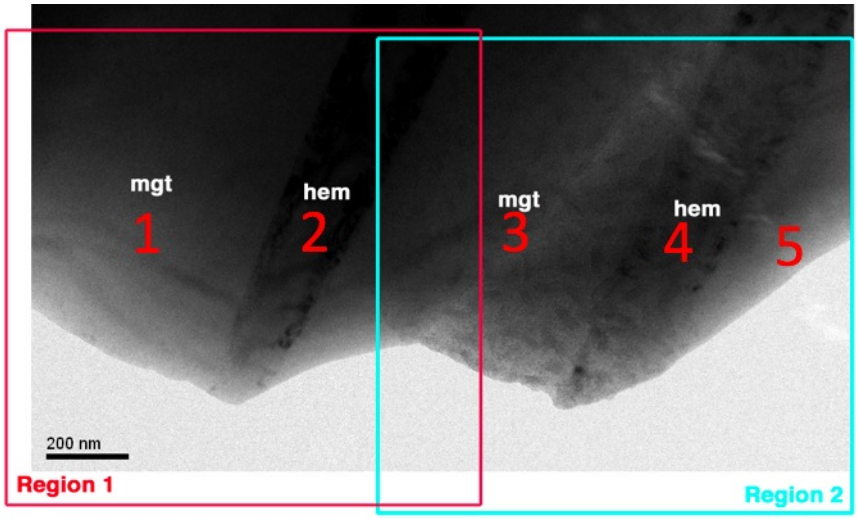

Figure C.1: Image showing the TM09 hem50 sample. The areas of haematite and magnetite have been marked on the image. The individual lamellae have also been labelled and this numbering scheme will be used for all the subsequent models.

Figure C.2 shows the direct observations of applying an external field of $\pm 2.2T$. In the case of applying the positive field we see one vortex structure in lamella 1 and one in lamella 2. In the application of the negative field a vortex is again seen in lamella 1, however it is in the opposite direction to that seen when a positive field is applied. Lamella 5 is strongly homogenous in the presence of the positive field, but in the presence of the negative field has a vortex structure. The field intensity in lamellae 2 and 3 is lower than in the surrounding areas. Overall, in response to the positive field, more of the sample aligns in the applied field direction. This is not the case for the negatively applied field.

The results in Figures C.3 and C.4 show the results of applying a positive and a negative field of 1T. Although a 1T field is far lower than the 2.2T field used in the direct observations the results in Figures C.3 and C.4 are fully saturated in the direction of the applied field in each case. It can be assumed from this that the hem50 phase plays an important role in fixing the magnetisation in the individual lamellae of this sample. Figure C.5 shows the same geometry as used in Figures C.3 and C.4 in the absence of an applied field. The structure seen in Figure C.5 is extremely complex with three vortex states in lamella 1 and a further two in lamella 3. Lamella 5 has a singe domain (SD) structure.

Due to the number of assumptions that had to be made, such as thickness and composition, and also that it was not possible to model haematite, these results would not be expected to be in good agreement to the direct observations. These models do, however, indicate that the coupling between the different magnetic phases has a considerable effect on the overall magnetic structure.

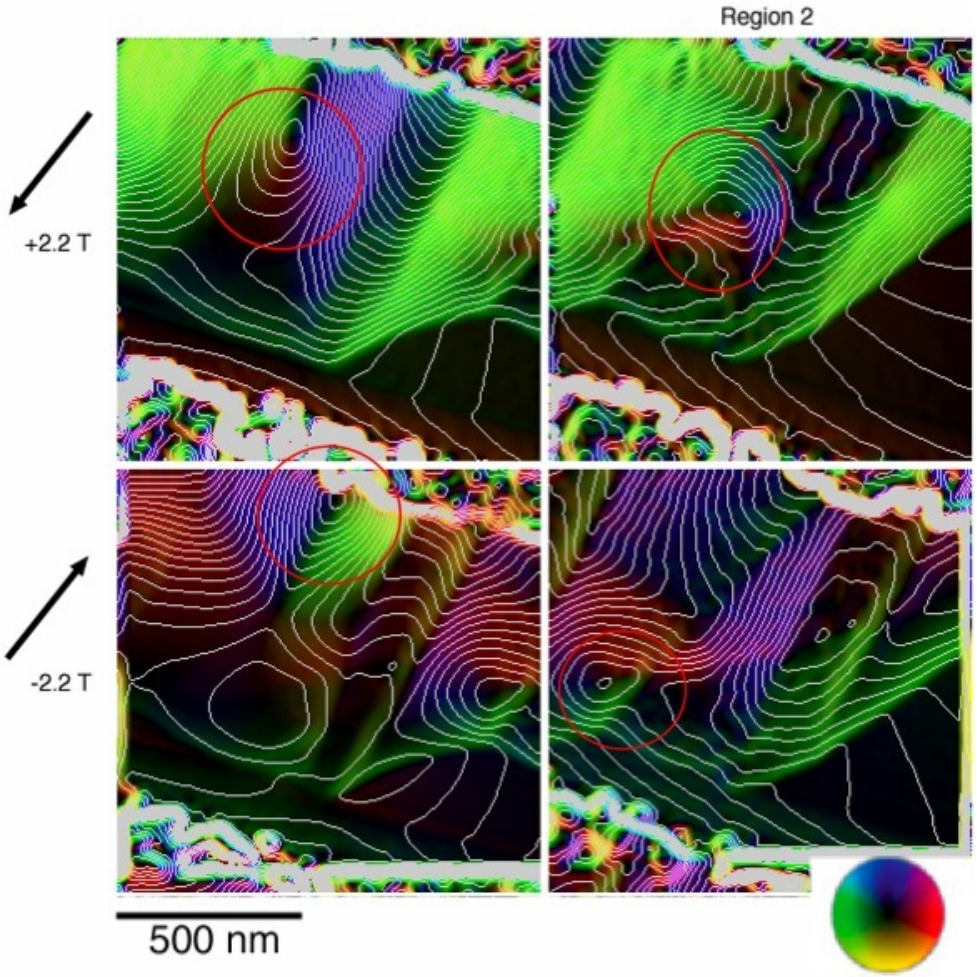

Figure C.2: Image showing the direct observations of the TM09 hem50 sample, the colour wheel indicates the field direction. The results are with the sample in the presence of an applied field of 2.2T and -2.2T in the opposing direction. Vortex structures can be seen in both lamellae 1 and 3 in both case the positioning and vortex direction differs. All the vortices have been circled. Lamella 5 remains mostly homogenous. The fuzzy areas are artifacts from the imaging process.

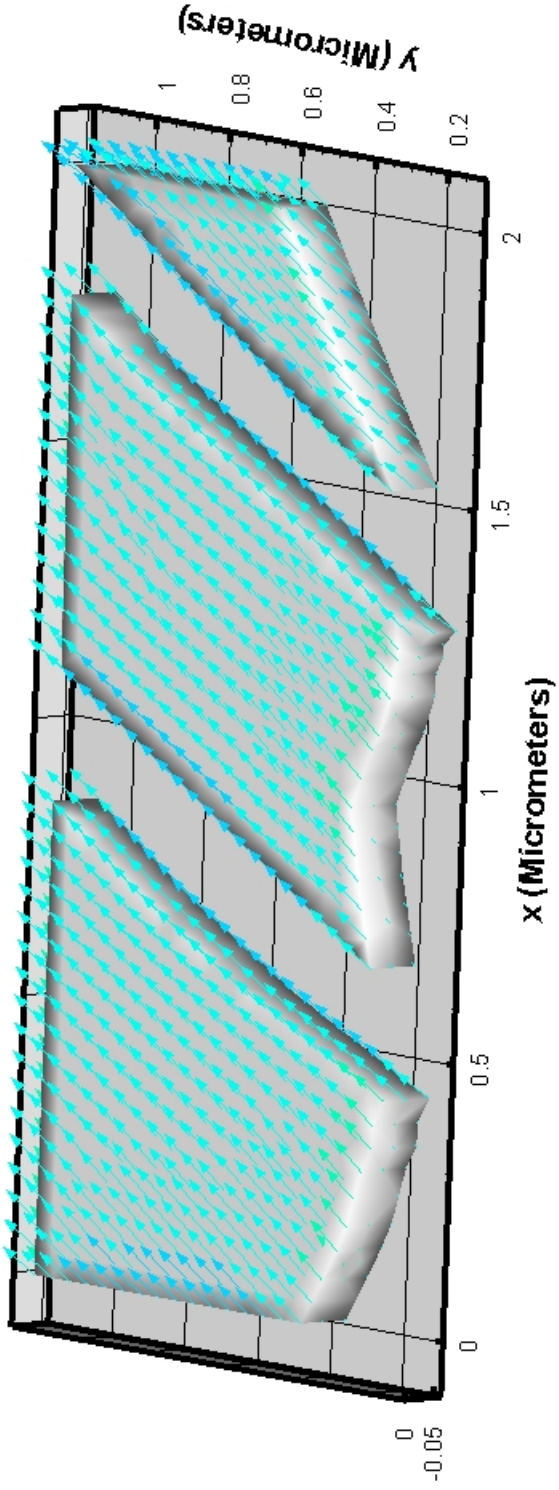

Figure C.3: This example shows the result where 1T was applied in the same direction as seen in Figure dobs. In this case we see that the entire structure is homogeneous and in the applied field direction.

Figure C.4: This example shows the result where -1T was applied in the same direction as seen in Figure dobs. In this case we see that the entire structure is homogeneous and in the applied field direction. This result is the inverse of the result seen in Figure100p

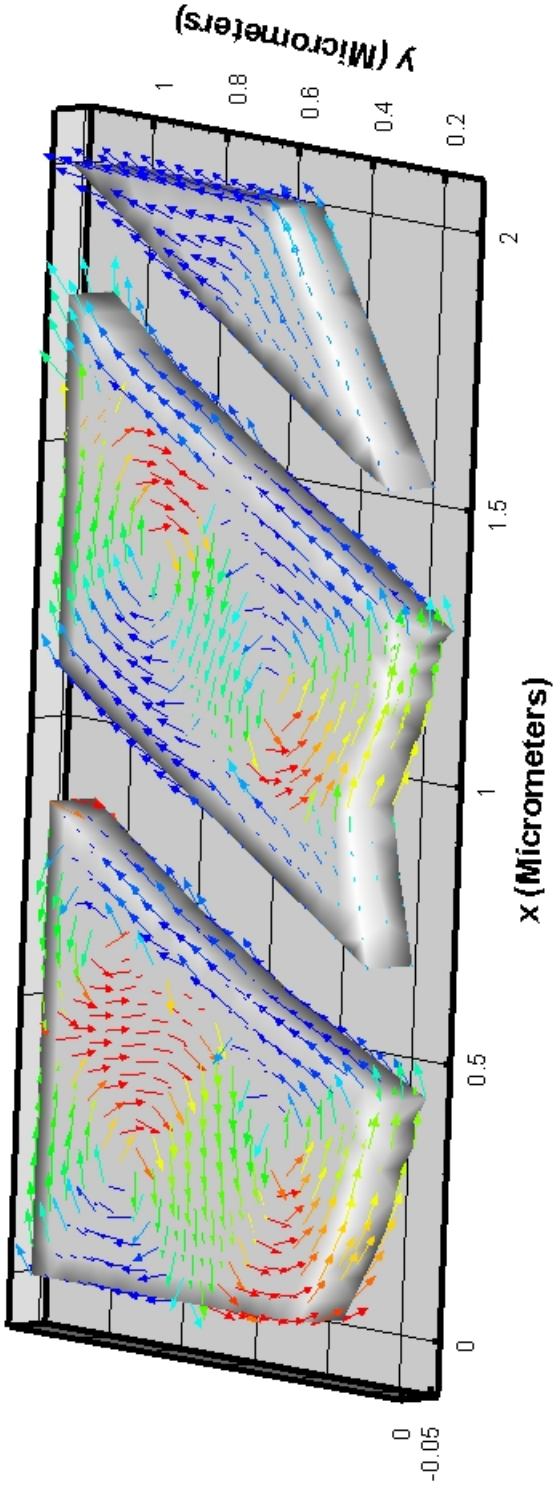

Figure C.5: Model of the magnetite haematite system with overall thickness of 100nm in the absence of an applied field. in this example three individual vortex states are seen in lamella 1 alone. A further 2 vortex states are seen in lamella 3 and lamella 5 has a SD structure.